

FRACTURE BEHAVIOR OF CONCRETE MATERIALS FOR RIGID PAVEMENT  
SYSTEMS

BY

AMANDA CHRISTINE BORDELON

B.S., University of Illinois at Urbana-Champaign, 2005

THESIS

Submitted in partial fulfillment of the requirements  
for the degree of Master of Science in Civil Engineering  
in the Graduate College of the  
University of Illinois at Urbana-Champaign, 2007

Urbana, Illinois

Adviser:

Professor Jeffery R. Roesler

*To my mom and dad, for their constant support and encouragement*

## **ACKNOWLEDGEMENTS**

I would like to thank my adviser, Professor Jeffery Roesler for his guidance and aid throughout my graduate studies. Also I would like to thank the graduate students Cristian Gaedicke, Kyoungsoo Park, Victor Cervantes, and Matthew Beyer for their assistance in various projects for this report. Also I would like to thank the undergraduate student Amruta Mate testing some fiber-reinforced concrete specimens in the summer of 2007. I also thank Klaus-Alexander Rieder from W. R. Grace for providing data for different types of fiber-reinforced concrete from 2002. I would like to thank Gregory Banas for his aid and training on the various testing methods used in my graduate research.

I thank the National Highway Institute Universities and Grants Program and the Illinois Chapter of the American Concrete Pavement Association for the fellowships I have received during the course of my graduate studies. I also thank the Illinois Department of Transportation for funding the ultra-thin whitetopping research project.

# TABLE OF CONTENTS

|   |      |
|---|------|
| LIST OF FIGURES .....                                   | vi   |
| LIST OF TABLES .....                                    | x    |
| LIST OF SYMBOLS .....                                   | xi   |
| LIST OF ABBREVIATIONS.....                              | xiii |
| CHAPTER 1: INTRODUCTION.....                            | 1    |
| Current Design Methods.....                             | 2    |
| Specific Pavement Research Projects .....               | 4    |
| CHAPTER 2: CONCRETE FRACTURE TESTING.....               | 8    |
| Background.....   | 8    |
| Fracture Testing Procedure.....                         | 11   |
| Data Calculation Analysis.....                          | 14   |
| CHAPTER 3: FRACTURE PROPERTIES OF PAVING MIXTURES ..... | 24   |
| Age Effect Studies .....                                | 26   |
| Age Effect Results .....                                | 29   |
| Mixture Proportioning Effects .....                     | 37   |
| Aggregate Type.....                                     | 40   |
| Prediction of Fracture Energy.....                      | 46   |
| CHAPTER 4: FUNCTIONALLY GRADED CONCRETE MATERIALS       |      |
| (FGCM).....   | 49   |
| Background.....   | 49   |
| FGCM Project Motivation .....                           | 51   |
| Functionally Graded Materials .....                     | 52   |
| Functionally Graded Material Results .....              | 55   |
| Finite Element Analysis.....                            | 63   |

|  |         |
|--|---------|
| CHAPTER 5: COMPOSITE BEAM TESTING .....  | 68      |
| Background .....   | 68      |
| Composite Beam Test .....  | 71      |
| Composite Beam Results .....   | 81      |
| Composite Beam Testing Issues .....  | 89      |
| Material Properties of Composite Beam Mixtures .....                                   | 93      |
| Concrete Free Shrinkage .....  | 96      |
| Summary .....  | 99      |
| <br>CHAPTER 6: FIBER-REINFORCED CONCRETE (FRC) MATERIALS FOR<br>RIGID PAVEMENTS .....  | <br>100 |
| FRC Beam Flexural Strength Results .....   | 104     |
| Residual Strength Analyses .....   | 111     |
| Beam Flexural Toughness Testing Standards Comparison .....                             | 116     |
| Summary .....  | 120     |
| <br>CHAPTER 7: CONCLUSION .....  | <br>121 |
| <br>REFERENCES .....   | <br>124 |
| <br>APPENDIX A: MICROMECHANICAL VIEW OF FIBER-REINFORCED<br>CONCRETE BEHAVIOR .....    | <br>128 |
| FRC Design and Construction .....  | 129     |
| Stress Distribution Theory in FRC Composites .....                                     | 135     |
| FRC models .....   | 138     |
| <br>APPENDIX B: CONCRETE LABORATORY PROCEDURES FOR CASTING<br>FRACTURE SPECIMENS ..... | <br>149 |

## LIST OF FIGURES

|  |    |
|--|----|
| Figure 1 - Single-edge notched beam configuration.....   | 10 |
| Figure 2 – Loading and Unloading Cycles for SEN(B) concrete specimen.....  | 12 |
| Figure 3 - Photograph of the single-edge notched beam during testing. ....   | 13 |
| Figure 4 - Testing equipment for fracture testing: (a) Instron control tower, (b)<br>Instron panels, and (c) data acquisition computers.....             | 13 |
| Figure 5 – Schematic of loading and unloading cycles of a TPB specimen used to<br>compute initial compliance $C_i$ and unloading compliance $C_u$ . .... | 14 |
| Figure 6 - Focal point method for compliance determination [from 21].....  | 16 |
| Figure 7 - $G_F$ calculation for a straight synthetic FRC specimen. ....   | 22 |
| Figure 8 - Stress intensity factor versus age both normalized at 28 days [from 49].....  | 26 |
| Figure 9 – Load versus CMOD curves for TPB specimen at 7 days.....   | 30 |
| Figure 10 - Load versus CMOD curves for the TPB specimen at 28 days.....   | 31 |
| Figure 11 - Load versus CMOD curves for the TPB specimen at 90 days.....   | 31 |
| Figure 12 – (a) Split-tensile strength and (b) TPB specimen peak loads and (c)<br>initial fracture energies compared to compressive strength.....        | 34 |
| Figure 13 - Stress intensity factor verses age for various mixtures.....   | 36 |
| Figure 14 - Compressive strength and initial fracture energy versus cement<br>content.....   | 39 |
| Figure 15 - Gradation curves for coarse aggregates and corresponding standard<br>limits. ....  | 42 |
| Figure 16 - Gradation curve for the natural sand and fine aggregate standard<br>limits. ....   | 42 |
| Figure 17 – TPB concrete specimen load versus CMOD curves for different<br>coarse aggregate types at various testing ages.....                           | 44 |

|   |    |
|---|----|
| Figure 18 - Predicted fracture properties versus measured properties for (a) initial fracture energy and (b) total fracture energy. ....            | 48 |
| Figure 19 - Three-point bending beam test setup for functionally layered concrete specimens.....  | 54 |
| Figure 20 - FGCM beam configurations: a) PCC/PCC, b) FRC/FRC, c) PCC/FRC, and d) FRC/PCC.....   | 55 |
| Figure 21 - Fracture load versus CMOD curves for plain concrete and straight synthetic FRC layer configurations. ....                               | 57 |
| Figure 22 – TPB specimen load versus CMOD curves for plain concrete and crimped steel FRC layer configurations. ....                                | 60 |
| Figure 23 - FRC TPB Specimen Load versus CMOD curve carried out to specimen fracture ( $P = 0.05$ kN).....  | 63 |
| Figure 24 - Simulations of the FRC results using various models (a) up to 4mm CMOD and (b) full range of CMOD [from 42].....                        | 66 |
| Figure 25 - Simulation using the trilinear softening ( $w_f = L_f/4$ ) model for FGCM combinations using FRCpp and plain concrete [from 42].....    | 67 |
| Figure 26 - Initial composite (concrete on asphalt) beam test setup [from 45].....  | 73 |
| Figure 27 - Initial composite (concrete on concrete) test setup [from 7].....   | 74 |
| Figure 28 - a) Schematic of the soil box components for composite testing, b) the top of the soil box and c) compaction of the soil in the box..... | 76 |
| Figure 29 - Composite beam test setup.....  | 80 |
| Figure 30 – Vertical deflections (stroke) for 1 <sup>st</sup> composite beam specimen.....  | 82 |
| Figure 31 - Vertical deflections (stroke) for 2 <sup>nd</sup> composite beam specimen. ....   | 82 |
| Figure 32 - Vertical position comparison between machine stroke and LVDT values. ....   | 83 |
| Figure 33 - Load versus crack opening displacement curves for Schanck Avenue composite beam specimens.....  | 84 |

|  |     |
|--|-----|
| Figure 34 - Load versus crack opening displacement curves for non-reinforced composite beam specimens.....   | 85  |
| Figure 35 - COD from clip gauge versus the neutral axis vertical deflection LVDT.....                        | 85  |
| Figure 36 - Example of composite beam specimen result.....   | 87  |
| Figure 37 - Picture of fractured composite beam.....   | 90  |
| Figure 38 – Failure pattern in the second Brazil 2 composite beam specimen.....                              | 91  |
| Figure 39 - Photo of an upside-down HMAC section prior to saw-cutting into beam sizes.....                   | 92  |
| Figure 40 - TPB Specimen load versus CMOD curves for Schanck concrete mixtures.....                          | 93  |
| Figure 41 - TPB Specimen load versus CMOD curves for non-reinforced concrete mixtures.....                   | 94  |
| Figure 42 – TPB Specimen load versus CMOD curves for run-out tests for Schanck mixtures.....                 | 96  |
| Figure 43 – Concrete free shrinkage results for the UTW mixtures.....  | 98  |
| Figure 44 - Mass loss results for the UTW mixtures.....  | 98  |
| Figure 45 - Photo of the equipment and set-up for the 4-point bending MOR test.....                          | 102 |
| Figure 46 – Straight synthetic FRC 4-point bending flexure curves.....                                       | 105 |
| Figure 47 – TPB specimen load versus CMOD curves for straight synthetic FRC mixtures.....                    | 106 |
| Figure 48 - Synthetic FRC 4-point bending flexure curves.....  | 107 |
| Figure 49 - Crimped steel FRC 4-point bending flexure curves.....  | 108 |
| Figure 50 – SEN(B) load versus CMOD curves for 0.5% volume fraction of crimped steel 2 fibers at 7-days..... | 109 |
| Figure 51 - Hooked end FRC 4-point bending flexure curves.....   | 110 |

|  |     |
|--|-----|
| Figure 52 - Schematic of a load versus midspan deflection for the ASTM C 1018 standard [from 2].....   | 112 |
| Figure 53 - Schematic of the load versus midspan deflection for ASTM C1609 and JCI-SF4 standards. ....   | 114 |
| Figure 54 - Comparison between the residual strength ratios of ASTM C 1609 and JCI-SF4 standards. ....   | 118 |
| Figure 55 – (a-d) SEM images of the fiber-cement interface [from 10] and (e-f) a microstructure schematic of FRC [from 9].....                         | 132 |
| Figure 56 - Secondary electron image of a straight synthetic fiber in concrete matrix. ....  | 133 |
| Figure 57 – A straight polypropylene/polyethylene fiber pulled out from the concrete matrix.....   | 134 |
| Figure 58 – a) Diagram of a fiber bridging a crack and b)the components of the force as the fiber pulls out of the matrix [from 26].....               | 137 |
| Figure 59 – Normalized stress versus displacement curve for Viscalvanich & Naaman model and corresponding experimental results [after 29]. ....        | 140 |
| Figure 60 – Schematic of Li’s micromechanical model for FRC.....   | 141 |
| Figure 61 - Aggregate interlock determination for high and normal strength plain concrete [from 31].....   | 142 |
| Figure 62 - Data and Li’s model stress versus crack opening curve for (a) steel FRC and (b) synthetic FRC [from 31]. ....                              | 145 |
| Figure 63 - Li's model applied to straight synthetic FRC at (a) $d_f = 0.44\text{mm}$ , $f = 0.05$ and (b) $d_f = 0.195\text{mm}$ , $f = 0.702$ . .... | 147 |

## LIST OF TABLES

|   |     |
|---|-----|
| Table 1 - Selected IDOT mixtures for UTW projects throughout Illinois.....                                | 6   |
| Table 2 - Concrete Mixture Designs of Field Projects .....  | 7   |
| Table 3 - Age Effect Concrete Mixture Designs .....   | 28  |
| Table 4 - Age Effect Batch Testing Plan and Fresh Properties .....  | 29  |
| Table 5 - Age Effect Strength and Fracture Properties.....  | 33  |
| Table 6 - Aggregate Properties .....  | 41  |
| Table 7 – Concrete Mixture Designs of Different Coarse Aggregates.....                                    | 43  |
| Table 8 - Average Concrete Strength and Fracture Properties for Different Coarse<br>Aggregate Types ..... | 45  |
| Table 9 - Mixture Designs for FGCM in lb/yd <sup>3</sup> .....  | 53  |
| Table 10 - Concrete Mixtures Average Fresh Properties and Strengths.....                                  | 56  |
| Table 11 - FGCM Average Fracture Properties.....  | 59  |
| Table 12 - UTW Mixture Designs for Composite Beam Testing.....  | 78  |
| Table 13 - UTW Fresh Properties and Strengths .....   | 79  |
| Table 14 – Average Composite Beam Specimen Results.....   | 87  |
| Table 15 - Fracture Results of UTW Mixtures .....   | 94  |
| Table 16 - Fiber Properties .....   | 103 |
| Table 17 - Concrete Proportions for FRC Study (in lb/yd <sup>3</sup> ).....                               | 104 |
| Table 18 – Average Flexural and Residual Properties of FRC.....   | 117 |
| Table 19 – Orientation and Length Efficiency Factors for FRC [after 11]. .....                            | 136 |

## LIST OF SYMBOLS

|               |   |
|---------------|---|
| $\alpha$      | Notch to depth ratio (subscript: $0$ = initial, $c$ = critical)   |
| $a$           | Notch depth (subscript: $0$ = initial, $c$ = critical)  |
| $A_f$         | Area of fiber   |
| $b$           | Beam width  |
| $BSG_{SSD}$   | Bulk specific gravity at saturated surface dry condition  |
| $C$           | Compliance (subscript: $i$ = initial loading, $u$ = unloading)  |
| $CMOD$        | Crack mouth opening displacement (subscript: $c$ = critical; superscript: $P$ = peak, $e$ = elastic)  |
| $CTOD_c$      | Critical crack tip opening displacement   |
| $\delta_0$    | Mid-span deflection at peak load  |
| $\delta_f$    | CMOD displacement corresponding to $P = 0.05$ kN at failure   |
| $d$           | Beam depth  |
| $d_a$         | Maximum coarse aggregate size   |
| $d_f$         | Fiber diameter  |
| $\varepsilon$ | Strain (subscript: $c$ = composite, $f$ = fiber, $m$ = matrix)  |
| $E$           | Modulus of elasticity (subscripts $i$ = initial, $f$ = fiber, $m$ = matrix, $u$ = unloading)  |
| $f$           | Residual strength (subscript: $150,3$ = at 3 mm midspan deflection, $e,3$ = up to 3mm deflection)   |
| $f'$          | Strength (subscript: $c$ = compressive, $t$ = split-tensile)  |
| $g_1(\alpha)$ | Geometric function for the TPB specimen   |
| $g_2(\alpha)$ | Opening displacement geometric function for the TPB specimen  |
| $G$           | Fracture energy (subscript: $2mm$ = Total up to 2 mm CMOD, $f$ = initial or critical, $F$ = total)  |
| $K_{IC}$      | Critical stress intensity factor (mode I) (superscript: 28 = tested at 28 day age)  |
| $I$           | Residual strength indices = area under the load versus mid-span deflection curve (subscript: 5 = up to $5\delta_0$ , 10 = up to $10\delta_0$ , 20 = up to $20\delta_0$ ) divided by area until $\delta_0$ |

|             |   |
|-------------|---|
| $l$         | Embedment length of a fiber   |
| $L$         | Beam length   |
| $L_c$       | Critical fiber length   |
| $L_f$       | Fiber length  |
| $\eta$      | Fiber efficiency factor (subscript: $l$ = length, $\theta$ = orientation, $VN$ = from Visalvanich and Naaman model)   |
| $P$         | Load (subscript: $c$ = peak, $w$ = equivalent self weight)  |
| $\rho$      | Density of fiber  |
| $R$         | Residual strength ratio (subscript: $150,3$ = at 3 mm midspan deflection, $e,3$ = up to 3mm deflection, $5,10 = 20*\{I_{10} - I_5\}$ , $10,20 = 10*\{I_{20} - I_{10}\}$ ) |
| $\sigma$    | Stress (subscript: $0$ = peak multiple fiber bridging, $a$ = aggregate interlocking, $c$ = composite, $f$ = fiber bridging, $m$ = matrix, $ps$ = pre-stress)              |
| $S$         | Beam span   |
| $t$         | Time (in days)  |
| $t_f$       | Fiber thickness   |
| $\tau$      | Shear stress or strength (subscript: $d$ = dynamic, $f$ = fiber, $s$ = static)  |
| $T_{150,3}$ | Toughness (area under load versus mid-span deflection) up to 3 mm deflection  |
| $V_f$       | Volume fraction of fiber reinforcement in the composite   |
| $w$         | Fiber width   |
| $W_0$       | Weight of a TPB specimen  |
| $w_f$       | Final crack opening width   |
| $W_r$       | Area under the load versus CMOD envelope curve  |
| $W_t$       | Total energy of a TPB specimen  |

## LIST OF ABBREVIATIONS

|        |   |
|--------|---|
| ACPA   | American Concrete Pavement Association  |
| ASTM   | American Standards for Testing and Materials  |
| CMOD   | Crack mouth opening displacement  |
| COD    | Crack opening displacement  |
| COV    | Coefficient of variability  |
| FEM    | Finite element method   |
| FGM    | Functionally graded materials   |
| FGCM   | Functionally graded concrete materials  |
| FRC    | Fiber-reinforced concrete (subscripts: PP – straight synthetic; CS – crimped steel 1) |
| GGBF   | Ground granulated blast furnace   |
| HMAC   | Hot-mixed asphalt concrete  |
| IDOT   | Illinois Department of Transportation   |
| JCI    | Japan Concrete Institute  |
| LEFM   | Linear elastic fracture model   |
| LVDT   | Linear variable differential transformer  |
| MOR    | Modulus of rupture  |
| PCC    | Portland cement concrete  |
| SEM    | Scanning electron microscope  |
| SEN(B) | Single-edge notched beam  |
| TPB    | Three-point bending   |
| TPFM   | Two-parameter fracture model  |
| UEL    | User-defined element  |
| UTW    | Ultra-thin whitetopping   |

## **CHAPTER 1: INTRODUCTION**

The design of rigid pavement today focuses on the stress analysis, climate, supporting layer and geometric effects. Consequently, less effort has been given to understanding the progressive failure of concrete pavements and specifically the crack propagation in the concrete materials. All concrete materials are assumed to be equivalent as long as they have the same strength; however this assumption is not always true. A new comparative measure for concrete materials is needed for understanding progressive failure of concrete slabs. More detailed information about concrete material, such as its fracture properties, is required along with the strength to better quantify crack propagation rates of varying concrete mixture proportions and constituents.

Several relatively new rigid pavement design concepts in the United States are two-layer paving and ultra-thin whitetopping (UTW). Field projects provide information on constructability and performance under environmental and traffic loading conditions. Laboratory research can assist to optimize the concrete material behavior to meet the overall pavement performance seen in the field projects. Characterizing the strength and fracture properties of concrete materials will give insight into the potential for early fatigue cracking, or in the case of UTW, susceptibility to reflective cracking. Furthermore, there is a huge gap in understanding the progressive cracking in concrete pavements and thus fracture properties are required if future 3-D modeling is going to be completed.

The main focus of this thesis is to determine fracture properties of concrete mixtures used in three projects – specifically functionally graded concrete materials (FGCM) for two-lift rigid pavement construction, UTW composite material behavior, and fiber-reinforced concrete (FRC) pavements – and the evaluation of mixture design selection to assist engineers in optimizing field performance. Concrete mixture designs from several rigid pavement projects were evaluated in the laboratory for their strength and fracture properties. The following sections review the current design philosophy of concrete pavements, present an argument for use of fracture testing of concrete materials, and finally review three relatively new rigid pavement systems.

### ***Current Design Methods***

Rigid pavement design guides have been developed over the years using nomographs, tables, and equations to predict the required slab thickness and service life. Concrete pavements must perform multiple functions such as handling the traffic loads, resisting thermal and moisture gradients, attenuate noise, and provide adequate skid/wear resistance and surface drainage. The input factors for mechanistic-empirical rigid pavement design guides include: slab geometry and support layers, material parameters, climatic information, and a variety of traffic characteristics. The final design is a single, monolithic concrete pavement layer that attempts to optimize the required functions for which the pavement must perform as far as fatigue, volume stability and functional service qualities. Most rigid pavements are over-designed with thicker slabs and many

times with higher concrete strengths than necessary. These conservative designs may not be the most economical either.

The main structural performance issue for rigid pavements is either early-age cracking or long-term fatigue cracking of the concrete slab. The initiation of cracking in concrete and the flexural load capacity of a concrete slab are related to its tensile strength and fracture properties. More recent design guides include the modulus of rupture (MOR) or flexural strength of the concrete to capture the material failure characteristics in bending. However, the behavior within the material during cracking is still not included in design guides. For concrete pavement systems associated with rehabilitation, it is important to understand the concrete behavior with respect to whether cracks are in the slab initially or in the supporting layers. Fracture mechanic tests can be used to measure the fracture properties of the material which can characterize the residual strength of a cracked concrete structure and can forecast the load carrying capacity of a slab for a given concrete material and geometry. The concrete material can be optimized for maximum pavement performance and economy with the knowledge of its fracture properties.

Specific projects were performed to determine the fracture and residual strength behavior of concrete mixtures commonly seen in pavement construction. The theory and testing procedure to determine the fracture properties of all the concrete mixtures in this thesis are presented in Chapter 2. The effects of concrete age, mixture proportions and constituents for concrete paving mixtures have been specifically investigated; these are presented in Chapter 3.

## ***Specific Pavement Research Projects***

### *Two-Layered Paving (or FGCM)*

Two-layered paving projects have been performed in the U.S. and Europe. They often are designed to incorporate the less-desired materials such as recycled concrete aggregate in the bottom concrete lift. The characteristics of these lesser quality materials are either poor for construction or unknown; thus analysis using these materials and their impact on the overall structural performance is important for the implementation in two-layered paving projects. Adding fiber-reinforcement can be used in concrete to increase the fracture properties (i.e. toughness) of the material. This report uses mixtures of plain and fiber-reinforced concrete to investigate the fracture performance of FGCM through two-layered single-edge notched beams [SEN(B)]. Background, experimental descriptions and results of the FGCM investigation for two-layered paving projects can be found in Chapter 4.

### *Ultra-Thin Whitetopping (UTW)*

UTW refers to a rehabilitation technique of placing a thin concrete overlay on a deteriorated hot-mixed asphalt pavement section. The fracture properties the concrete mixtures are important for understanding the mechanisms behind the UTW pavement performance, especially load carrying capacity, load transfer efficiency at joints, and debonding from the hot-mixed asphalt. An experimental program was designed to determine the fracture properties of UTW concrete mixtures used in the field. Table 1 shows field mixtures from IDOT UTW projects; Table 2 shows field mixtures for a continuously reinforced project on the Dan Ryan in Chicago, IL and UTW projects in

Sao Paulo, Brazil). A test method was also developed herein to represent the composite system (concrete, hot-mixed asphalt, and soil) behavior. Shrinkage specimens were sampled since this is the main contributor to de-bonding in field UTW projects. Chapter 5 provides the background, experimental set-up, and results of the composite beam testing and related material property findings using the UTW mixtures.

#### *Fiber-Reinforced Concrete (FRC)*

One main challenge for materials engineers is specifying fiber reinforcement type and amount for use in concrete pavements. A study was performed to understand the impacts of fiber type and volume fraction on the toughness properties and flexural strengths (modulus of rupture and residual flexural strength properties) of FRC. Other research project results were combined for a greater database of fiber types at different volume fractions and their respective properties. A comparison was also made between available testing procedures (American Standards for Testing and Materials and Japan Concrete Institute) for flexural strength of FRC mixtures. The results of these FRC tests can be seen in Chapter 6.

**Table 1 - Selected IDOT mixtures for UTW projects throughout Illinois**

| Location         | Schanck Avenue        | Int. of Vienna and Main Streets | Int. of US Hwy 45 and IL Rt. 13 | US Hwy 36           | Int. of US Hwy 36 with Oakland and Country Club Road | Int. of US Hwy 51 and Pleasant Hill Road | Cumberland County Highway 2 | Macon County Highway 27 | Piatt County Highway 4 | Clay County Highway 3  |
|------------------|-----------------------|---------------------------------|---------------------------------|---------------------|--|--|-----------------------------|-------------------------|------------------------|------------------------|
| District         | District 1, Mundelein | District 9, Anna                | District 9, Harrisburg          | District 5, Tuscola | District 5, Decatur                                  | District 9, Carbondale                   | District 5, Toledo          | District 5, Harristown  | District 5, Monticello | District 7, Louisville |
| Coarse Aggregate | 1972                  | 1805                            | 1847                            | 1704                | 1713   | 1805                                     | 1836                        | 1910                    | 1957                   | 1814                   |
| Fine Aggregate   | 022CAM11              | 022CAM11                        | 022CAM11                        | 022CAM11            | 022CAM16   | 022CAM11                                 | 022CMM11                    | 022CMM07                | 022CAM07               | 022CAM11               |
| Cement           | 1001                  | 1008                            | 959                             | 1035                | 1210   | 1008                                     | 1256                        | 1313                    | 1220                   | 1286                   |
| Water            | 027FAM02              | 027FAM01                        | 027FAM01                        | 027FAM01            | 027FAM01   | 027FAM01                                 | 027FAM01                    | 027FAM03                | 027FAM04               | 027FAM05               |
| Class C Fly Ash  | 515                   | 755                             | 755                             | 755                 | 705  | 755                                      | 575                         | 534                     | 534                    | 534                    |
| Synthetic Fibers | 267                   | 273                             | 292                             | 255                 | 239  | 273                                      | 197                         | 162                     | 179                    | 244                    |
| Air Entrainment  | 140                   | 0                               | 0                               | 0                   | 0  | 0  | 0                           | 0                       | 0                      | 0                      |
| Water Reducer    | 4                     | 0                               | 3                               | 0                   | 0  | 3  | 0                           | 0                       | 0                      | 0                      |
| Retarder         | Daravair 1400         | Daravair 1400                   | Daravair 1400                   | Daravair 1400       | Daravair 1400  | Daravair 1400                            | Daravair 1400               | Daravair 1400           | Daravair 1400          | Daravair 1400          |
| w/cm             | WRDA 82               | Daracem 65                      | Daracem 65                      | Daracem 65          | Daracem 65 / WRDA 19                                 | Daracem 65                               | -                           | Daracem 65              | Daracem 65             | WRDA 82                |
| coarse/fine      | -                     | -                               | -                               | -                   | -  | (Daratard 17, Hot Days)                  | Daratard 17                 | -                       | -                      | -                      |
| % agg            | -                     | -                               | -                               | -                   | -  | -  | -                           | -                       | -                      | -                      |
| wt ratio         | 0.41                  | 0.36                            | 0.39                            | 0.34                | 0.34   | 0.36                                     | 0.34                        | 0.30                    | 0.34                   | 0.46                   |
| wt ratio         | 1.97                  | 1.79                            | 1.93                            | 1.65                | 1.42   | 1.79                                     | 1.46                        | 1.45                    | 1.60                   | 1.41                   |
| wt ratio         | 76.3%                 | 73.2%                           | 72.8%                           | 73.1%               | 75.6%  | 73.2%                                    | 80.0%                       | 82.2%                   | 81.7%                  | 79.9%                  |

**Table 2 - Concrete Mixture Designs of Field Projects**

| Location         |                       | Dan Ryan            |               | Brazil          |                 |
|------------------|-----------------------|---------------------|---------------|-----------------|-----------------|
|                  |                       | Express Lanes       | Local Lanes   | SP-280          | USP campus      |
| Coarse Aggregate | lb/yd <sup>3</sup>    | 1894                | 1887          | 2013            | 1734            |
|                  | type                  | 022 CM 07           | 022 CM 11     | Crushed Granite | Crushed Granite |
| Fine Aggregate   | lb/yd <sup>3</sup>    | 1258                | 1230          | 831             | 1082            |
|                  | type                  | 029 FMM 20          | 027 FM 02     | Round Quartz    | Round Quartz    |
| Cement           | lb/yd <sup>3</sup>    | 435                 | 435           | 742             | 802             |
| Water            | lb/yd <sup>3</sup>    | 230                 | 230           | 298             | 340             |
| Silica Fume      | lb/yd <sup>3</sup>    | 0                   | 0             | 74              | 48              |
| GGBF Slag        | lb/yd <sup>3</sup>    | 110                 | 110           | 0               | 0               |
| Air Entrainment  | type                  | Excel AEA (3523-01) | Daravair 1400 | N/A             | none            |
|                  | fl.oz/yd <sup>3</sup> | N/A                 | N/A           | 3               | 0               |
| Water Reducer    | type                  | Redi-set (767-01)   | WRDA 82       | N/A             | N/A             |
|                  | fl.oz/yd <sup>3</sup> | N/A                 | N/A           | 43              | 37              |
| Superplasticizer | type                  | none                | none          | N/A             | N/A             |
|                  | fl.oz/yd <sup>3</sup> | 0                   | 0             | 140             | 62              |

|             |          |       |       |       |       |
|-------------|----------|-------|-------|-------|-------|
| w/cm        | wt ratio | 0.42  | 0.42  | 0.37  | 0.40  |
| coarse/fine | wt ratio | 1.51  | 1.53  | 2.42  | 1.60  |
| % agg       | wt ratio | 80.3% | 80.1% | 71.9% | 70.3% |

## **CHAPTER 2: CONCRETE FRACTURE TESTING**

Fracture mechanics is a growing field of interest within pavement engineering. All of the research initiatives presented in this thesis utilized fracture mechanics theory and testing methods. Other concrete material properties (such as strength) were also measured for further evaluation of the material behavior. This chapter summarizes the background behind using fracture mechanics in concrete pavement material characterization and explains the specific testing and analysis procedure used to determine fracture properties of the concrete mixtures.

### ***Background***

The current design of rigid pavements relies on hardened concrete properties such as compressive, tensile and flexural strengths. Although these properties have been used successfully for years, the existing design inputs do not capture the entire cracking behavior of the pavement structure. By quantifying failure properties of the concrete, a better grasp of how the concrete pavement performs throughout its life can be ascertained. Through fracture mechanics, material parameters indicating the initiation and growth of cracks and the nominal load capacity of initial cracked structures can be derived. The fracture toughness has been used to describe the rate of crack propagation through the concrete. The use of fracture energy with a cohesive zone model can quantify the load capacity of a beam or slab [38] or indicate the ability of a concrete material to transfer load across a crack or joint [14].

Concrete is often considered a brittle material, which alludes to the possibility of analyzing it with linear elastic fracture mechanics. In reality, concrete is a quasi-brittle material which exhibits a significant amount of nonlinear behavior especially after the peak strength is reached. Due to the nonlinear behavior, the recommended specimen size for testing to obtain size independent concrete material properties would be extremely large. Therefore, size effect considerations are an important issue that must be accounted for when testing concrete specimens. Typically, an equivalent elastic crack approach is used to account for the observed nonlinearity of the concrete fracture process. This testing and modeling approach allows for the calculation of “size independent parameters” using practically sized specimens.

Bazant [5] has performed several studies using concrete and determined that the nominal strength (e.g., flexural strength) of a material is dependent on the structural size and geometry. Several reasons for how the size impacts the properties of a material such as concrete have been described in his size effect model [5]. The size effects include: wall/boundary effect (aggregate size and surface paste), heat and water diffusion rates (related to the pore structure), heat generated from hydration, voids or defect probability, fracture or energy release rate. Each of these factors listed either increase or decrease strength and fracture properties depending on the size of the test specimen. Standardized fracture test methods using specific specimen geometries that are practical have been developed to characterize the fracture properties of concrete materials. These test methods specify the geometric constraints and boundary conditions needed in order to produce “size independent” fracture properties.

A RILEM procedure was developed by Jenq and Shah [23 and 43] using a single-edge notched beam (SEN(B)) to determine the fracture properties of the concrete. The single-edge notched beam specimen is configured for three-point bending with the load ( $P$ ) and crack mouth opening displacement ( $CMOD$ ) being measured. The specimen and load configuration for the SEN(B) test are shown in Figure 1. In order to characterize the fracture properties of various paving concretes the SEN(B) specimen configuration was utilized.

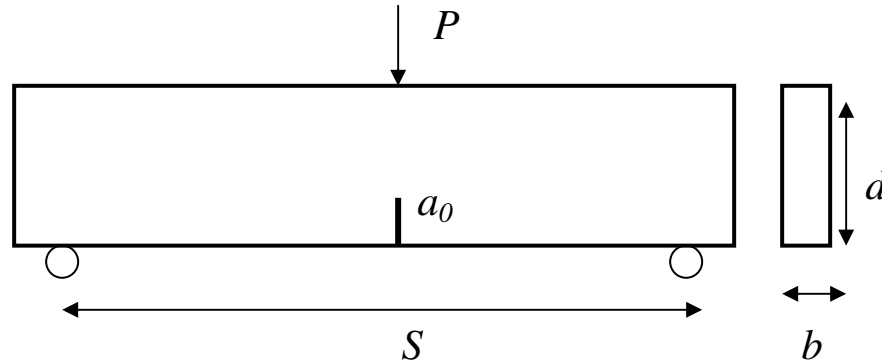


**Figure 1 - Single-edge notched beam configuration.**

Jenq and Shah developed the Two-Parameter Fracture Model (TPFM) to determine the critical stress intensity factor ( $K_{IC}$ ) and critical crack tip opening displacement ( $CTOD_C$ ) of a monolithic beam based on an effective elastic crack approach. The nonlinear fracture behavior was accounted for by using linear elastic fracture mechanics equations to calculate the effective elastic crack length based on the measured loading and unloading compliance of the beam. Geometric factors were included in the calculations to account for the geometry and size of the beams. A span-to-depth ratio ( $S/d$ ) was suggested in the TPFM to be 4; the initial notch depth  $a_0$  is 1/3 of the total depth  $d$ , and the notch width should be less than 5 mm [23]. The total beam dimensions (length x

depth x width) chosen were 700 x 150 x 80 mm with a span of 600 mm and an initial notch depth of 50 mm. It was recommended that four replicates of each beam be tested [24].

### ***Fracture Testing Procedure***

The Two-Parameter Fracture Model TPB beams were cast in steel molds and a notch was saw cut 24 hours before testing using a block saw with a diamond blade. Prior to testing two aluminum knife edges were placed 10 mm apart with a quick-set epoxy. An INSTRON clip gauge measuring opening displacement up to 4 mm range was clipped onto the knife edges to measure the crack mouth opening displacement (*CMOD*). An 11-kip MTS machine applied the monotonic load to the specimens. Cyclic compliance testing was useful for describing the deformation and crack propagation in a material. A LABVIEW program was developed to remotely control the testing of the concrete specimen through the clip gauge readings.

During testing a seating load of 0.05 kN was placed on each specimen followed by a constant opening displacement rate of 0.001 mm/sec. After the load decreased to 95 percent of the peak load, the data acquisition program automatically unloads the specimen over a 10 second period. The specimen was then again re-loaded and unloaded at 95 percent of the second peak load. The program was designed to continue this process for n-cycles. A plot of loading and unloading cycles is shown in Figure 2. For the majority of the experiments tested in this research, on the 3<sup>rd</sup> cycle, the opening

displacement rate was increased to 0.005 mm/sec and the program manually adjusted to not unload (i.e. continue constant displacement control) until the clip gauge went out of range or the load reached 0 kN, whichever was first.

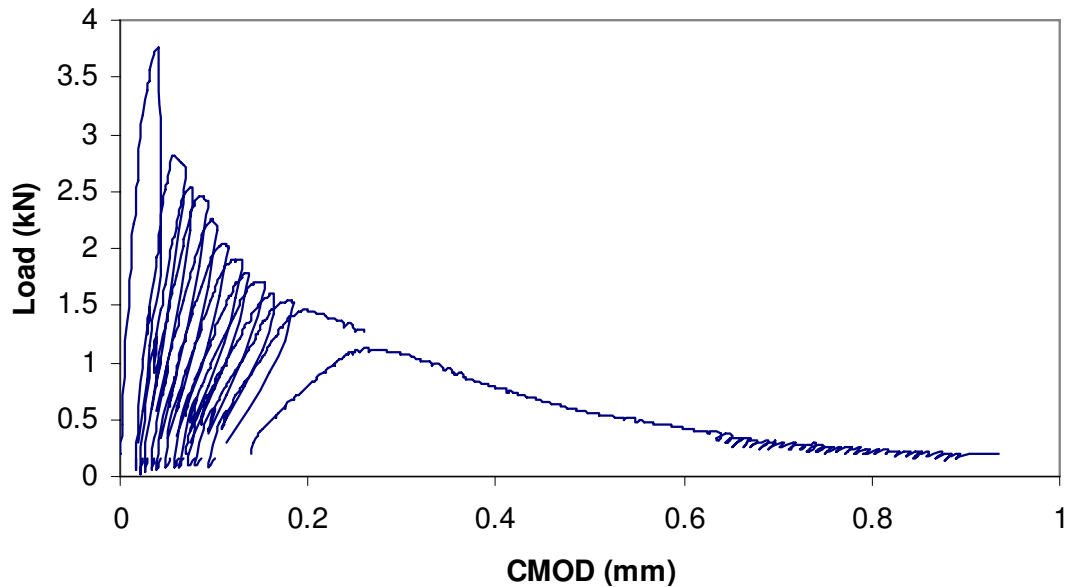


**Figure 2 – Loading and Unloading Cycles for SEN(B) concrete specimen.**

#### *Run-out test for FRC*

For some of the concrete materials, such as FRC, the clip gauge generally went out of range before the failure of the beam. Therefore a yo-yo gauge (a string extender linear transducer) with a 50 mm range was attached to one side of the beam with epoxy before the test (see Figure 3 for a photograph of the yo-yo gauge and clip gauge on the beam). The testing procedure for the FRC beams was still the same for the two initial cycles. A desktop computer controlled the test for the first two cycles. After the first two cycles were completed, the control of the test was switched over to a user-defined position ramping speed of 1 mm/min vertical machine position control using the 8800 Instron controls until failure was reached (determined manually when the load fell below 0.05

kN). An additional laptop computer was used for data recording of all cycles and the run-out beyond the range of the clip gauge. Figure 4 shows the 8800 Instron control machines and computers used.

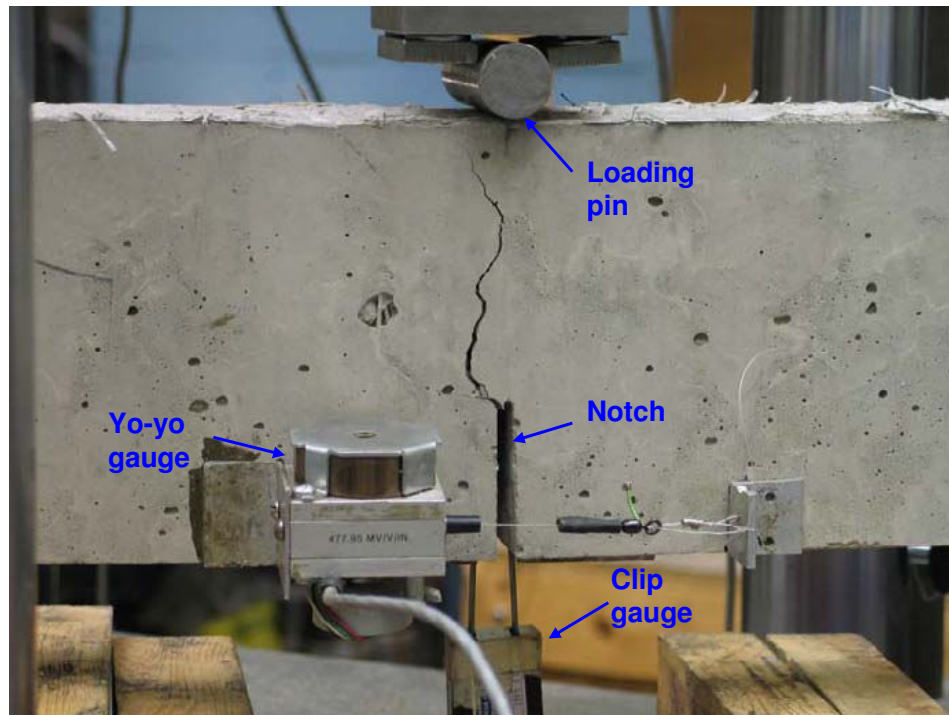


**Figure 3 - Photograph of the single-edge notched beam during testing.**

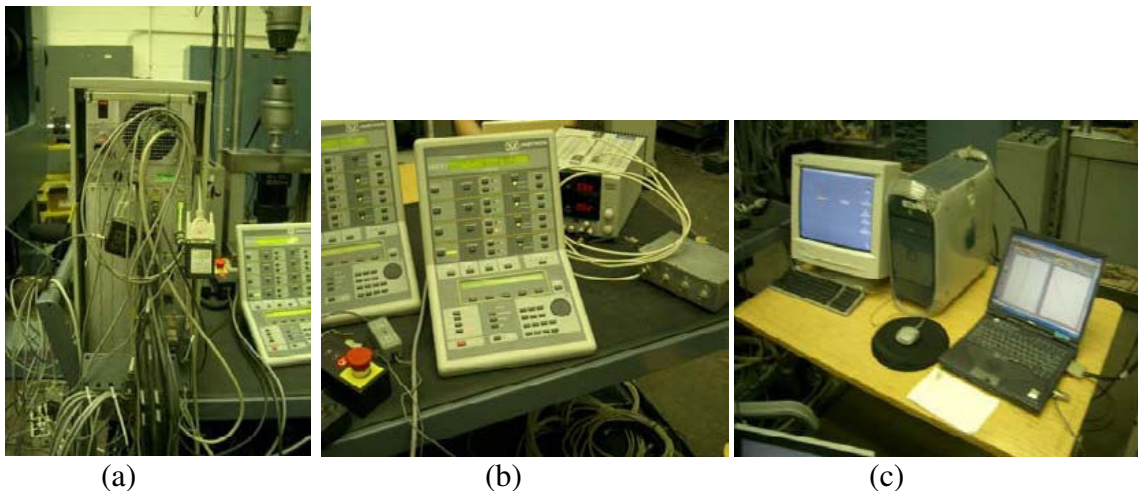


**Figure 4 - Testing equipment for fracture testing: (a) Instron control tower, (b) Instron panels, and (c) data acquisition computers.**

## Data Calculation Analysis

In order to plot the load-CMOD curve for each specimen, the clip gauge and yo-yo gauge data were correlated to each other and the change (based on the initial gauge reading) in corrected displacement is the CMOD. Figure 5 shows a schematic of the first and second loading cycles of the SEN(B).

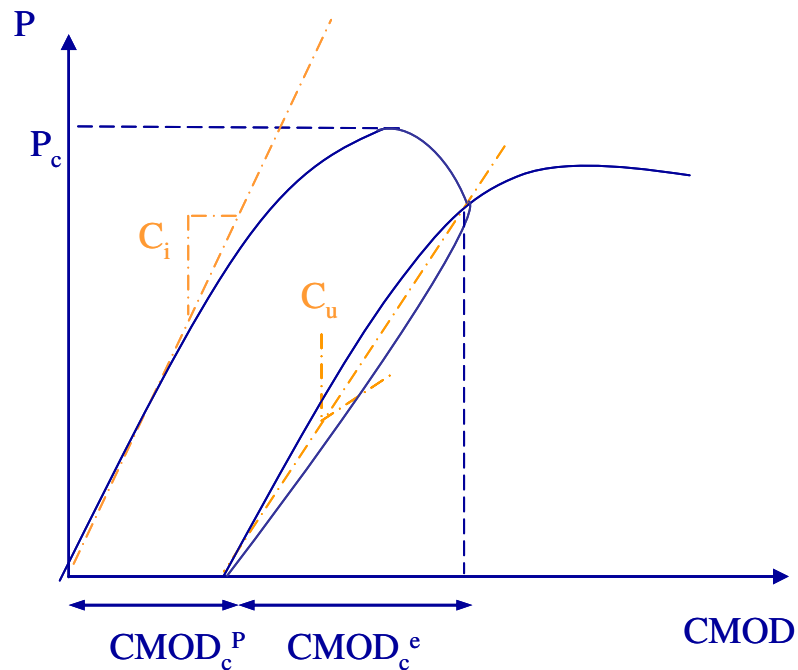


**Figure 5 – Schematic of loading and unloading cycles of a TPB specimen used to compute initial compliance  $C_i$  and unloading compliance  $C_u$ .**

### Analysis Inputs

The initial fracture properties were calculated from the loading and unloading compliance, the peak load ( $P_c$ ), the beam weight, and the initial notch depth. The beam weight was determined by multiplying the beam volume by the fresh concrete unit weight of the mixture measured during casting. The initial notch depth sometimes varied within

a specimen due to the rate at which the beams were cut under the saw;  $a_0$  was measured from the bottom surface of the beam to the top of the rounded notch tip.

The loading compliance ( $C_i$ ) was calculated as the inverse of the slope from 10% of the peak load until 50% of the peak load. This was estimated to be the linear elastic range and ignored any initial seating load discontinuities in the curve. The unloading compliance ( $C_u$ ) was the inverse of slope of the unloading curve. It was estimated that  $C_u$  should be calculated between 10% of the peak load and 80% of the peak load on the unloading curve. Since the calculation of  $C_u$  was dependent on the points chosen on the unloading curve other methods to determine of  $C_u$  were investigated and presented below.

#### *Compliance Determination*

The definition of loading and unloading compliance is shown in Figure 5. The compliances could be difficult to determine from the load versus CMOD curves since it involved some user subjectivity to determine the elastic part of the unloading compliance. The initial loading compliance for an elastic material was assumed to be roughly the inverse of the material loading stiffness. However, different methods exist for determining the initial slope such as tangent, secant, or chord stiffness. Computing the unloading compliance was even more difficult due to the inherent nonlinear elastic and inelastic response of the material during unloading. Ideally the test should be set up to unload immediately after the peak load was reached for the determination of the unloading compliance. Due to uncertainty in when the peak load level has been reached, the RILEM method proposed by Jenq and Shah [23] suggested unloading the specimen at

95% of the peak load with the assumption that the unloading slope at this load level was assumed to be similar to that from the actual peak load. This unloading technique also assumed there is no additional crack propagation from the peak load to the 95% peak value, which can lead to an error in the critical crack length calculation.

In order to eliminate operator controlled error, Jensen et al. [21] performed a study that implemented a focal point method for computing the unloading compliance. By extrapolating slopes (determined from the unloading curve) from several load/unload cycles back to a focal point; the need to unload a beam at 95% of the peak load was no longer required. A diagram of this process can be seen in Figure 6. In the paper by Jensen et al., little information was provided on how the actual compliance values for each unloading cycles were determined (tangent, chord, or secant compliance).

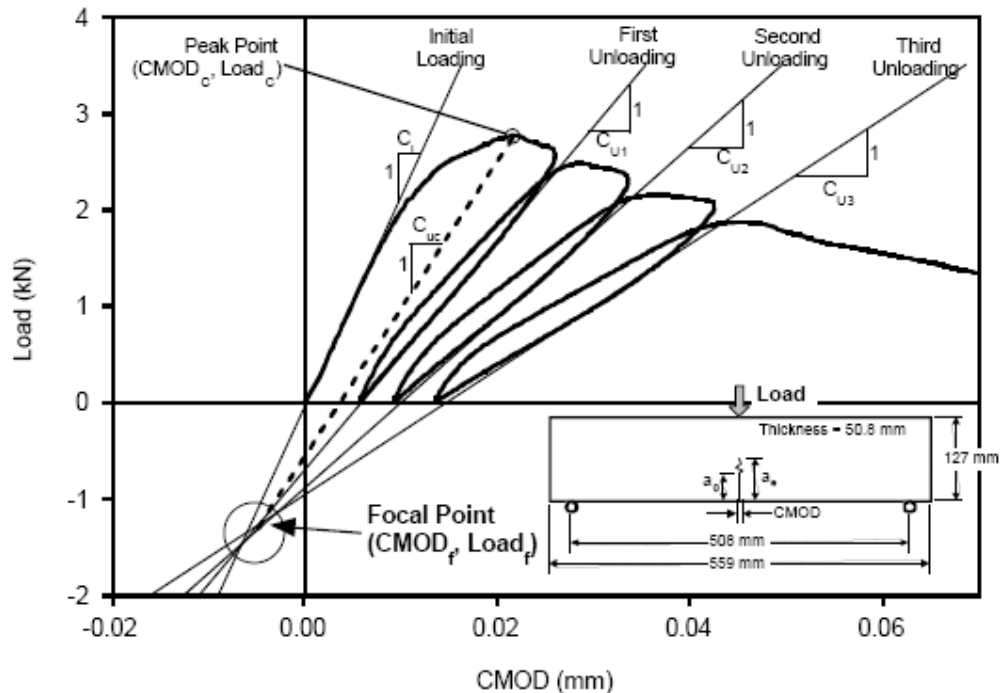


**Figure 6 - Focal point method for compliance determination [from 21].**

Computing the critical crack length could be determined by drawing a line between the focal point and the peak load and then calculating the unloading compliance. The critical crack length determined using the peak load compliance was always smaller than a compliance taken at any load after the peak load had been reached (when the crack has propagated beyond the critical length). Smaller critical crack lengths led to smaller critical stress intensity factor, critical crack tip opening displacement, and initial fracture energy values. In other words, Jensen et al. [21] found that the  $K_{IC}$  and  $CTOD_C$  values determined with the focal point method were consistently reduced by 12% and 38%, respectively, compared to just computing the unloading compliance from 10 and 80% of the peak load.

A specific feature that was noticed between specimens was that the duration or displacement at which the 95% post-peak unloading load was highly variable. Some specimens demonstrated a long gradual softening curve initially after the peak and the 95% load was not reached until a larger CMOD value; other specimens demonstrated almost instantaneous load reduction after the peak and thus the unloading began much sooner at smaller CMOD values. Either a manual unloading response or the focal point method may be desired in order to reduce the variability from those specimens which exhibit the more gradual post-peak curve.

The variability of the calculated  $K_{IC}$  and  $CTOD_C$  values using the focal point method was determined to be similar to the traditional TPFM, according to Jensen et al. [21]. For

example, the coefficient of variation on  $K_{IC}$  with the focal point method was 6.5% and was 5.1% for the TPFM; similarly, the coefficient of variation on  $CTOD_C$  was 37.0% using the focal point method and 21.0% using the TPFM. The focal point method was developed to supplement the TPFM to allow users to unload at any load level and still compute the relevant initial fracture properties. The focal point method may provide a more accurate result on fracture parameters however based on the larger variation reported in Jensen et al, it may not be as precise. For the studies performed in this thesis report, the TPFM with unloading from 95 percent of the peak load was used because the computer running the test was able to precisely detect the load level for automatic unloading at this level of loading. Due to the lack of improved accuracy for the focal point method, the loading and unloading compliances were respectively found by manually selecting specific data points along the loading (at 10% and 50% of the peak load) and unloading (at 80% and 10% of the peak load) curve as stated in the previous section.

#### *Calculation of Initial Fracture Properties*

The two fracture parameters determined through the TPFM were the critical stress intensity factor ( $K_{IC}$ ) and the critical crack tip opening displacement ( $CTOD_C$ ) [23 and 43]. These were computed by first obtaining the critical effective crack length ( $a_c$ ). By equating, the concrete's modulus of elasticity from the loading and unloading curves ( $E = E_i = E_u$ ) as shown in equations 1a and 1b, the critical effective crack length could be determine as follows:

$$E_i = \frac{6Sa_0g_2(\alpha_0)}{C_i d^2 b} \quad (1a)$$

$$E_u = \frac{6Sa_c g_2(\alpha_c)}{C_u d^2 b} \quad (1b)$$

where ( $S$ ) was the span, ( $d$ ) the depth, ( $b$ ) the width, ( $a_0$ ) the initial notch depth of the beam  $\alpha_0$  the initial notch/depth ratio,  $\alpha_c$  the critical notch/depth ratio and  $g_2(\alpha)$  the opening displacement geometric factor for the TPB specimen given by equation 2.

$$g_2(\alpha) = 0.76 - 2.28\alpha + 3.87\alpha^2 - 2.04\alpha^3 + \frac{0.66}{(1-\alpha)^2} \quad (2)$$

Once the  $a_c$  was computed, then the critical stress intensity factor ( $K_{IC}$ ) could be calculated from the following (equation 3),

$$K_{IC} = 3(P_c + 0.5W_0 S / L) \frac{S \sqrt{\pi a_c} g_1(a_c / d)}{2d^2 b} \quad (3)$$

where ( $P_c$ ) was the peak load,  $W_0$  was the weight of the specimen,  $L$  was the length of the specimen and ( $g_1$ ) was the stress intensity factor geometric function for the beam specimen defined as follows (equation 4).

$$g_1\left(\frac{a_c}{d}\right) = \frac{1.99 - (a_c / d)(1 - a_c / d)[2.15 - 3.93(a_c / d) + 2.70(a_c / d)^2]}{\sqrt{\pi}[1 + 2(a_c / d)][1 - (a_c / d)]^{3/2}} \quad (4)$$

Finally, the  $CTOD_C$  could be computed using equation 5.

$$CTOD_c = 6(P_c + 0.5W_0S/L) * \frac{Sa_c g_2(a_c/d)}{Ed^2b} * \left[ (1 - (a_c/a_0))^2 + [1.081 - 1.149(\frac{a_c}{d})] * [(a_c/a_0) - (a_c/a_0)^2] \right]^{1/2} \quad (5)$$

By using a thin TPB beam, plane stress was assumed and the critical energy release rate ( $G_f$ ), or also known as the initial fracture energy, was related to  $K_{IC}$  and the modulus of elasticity,  $E$ , by equation 6.

$$G_f = \frac{K_{IC}^2}{E} \quad (6)$$

#### *Total Fracture Energy*

The testing data from the TPB concrete specimen could also be used to calculate the area under the load-CMOD curve which can be related to the concrete total fracture energy ( $G_F$ ). Monotonic loading until specimen failure was usually employed instead of a cyclical load-unload testing process for determining the total fracture energy. Therefore the static cycles of the tested data were manually removed such that an envelope curve was drawn using the following: the initial loading data till the peak load, the data from the peak load to 95% of the peak load on each cycle, the remaining curve after cycles were complete until failure (at 0.05 kN).

According to Hillerborg [19], the total fracture energy ( $G_F$ ) or work of fracture was determined as the total energy ( $W_t$ ), normalized to the fracture area  $(d - a_0)b$ . The total energy ( $W_t$ ) was calculated using the sum of the area under the load ( $P$ ) vs.  $CMOD$

envelope curve ( $W_r$ ), and  $P_w\delta_f$ , where  $P_w$  was the equivalent self weight force, and  $\delta_f$  was the CMOD displacement corresponding to the applied load (zero) at failure. The equivalent self weight force and total fracture energy were calculated using equations 7 and 8, respectively.

$$P_w = \frac{W_0 S}{2L} \quad (7)$$

$$G_F = \frac{W_t}{(d - a_0)b} = \frac{W_r + 2P_w\delta_f}{(d - a_0)b} \quad (8)$$

The total fracture energy has more variability, especially compared to the initial fracture energy. Bazant et al. [6] described that much of the scatter in  $G_F$  calculation comes from: 1) inherent randomness in the tail end of the load-CMOD curve, 2) uncertainty in extrapolating the tail end of the curve to zero load, and 3) difficulty eliminating non-fracture sources of energy dissipation.

There is little information in the research literature as to the exact cut off criterion for the total fracture energy computation as it pertains to fiber-reinforced concrete (FRC) materials. The Hillerborg method was created for computing the fracture energy of plain concrete specimens that undergo complete specimen failure. With plain concrete, the area under the load-displacement curve from 0.05 kN to 0.0 kN load at failure is almost negligible. However, for such materials like FRC which have long post-peak curves and large displacements, the area under the load-displacement curve depended highly on the load to cut-off the area calculation. If the point of complete failure was determined to be

at the same load as the initial seating load, the fracture energy would be drastically lower for some FRC mixtures than if the point of failure were determined when the load reached a zero value with the testing apparatus. See Figure 7 for a schematic example of the area differences for FRC mixtures. For the FRC mixtures used in this report, the  $G_F$  was consistently computed as the area under the load-CMOD curve till 0.05 kN load (which was the applied load corresponding to the seating load). The Hillerborg method may still be a valid for determining the fracture energy. Clarification should be made for future testing to determine whether a load of zero or the initial seating load should be used as the cut-off criterion for the total fracture energy.

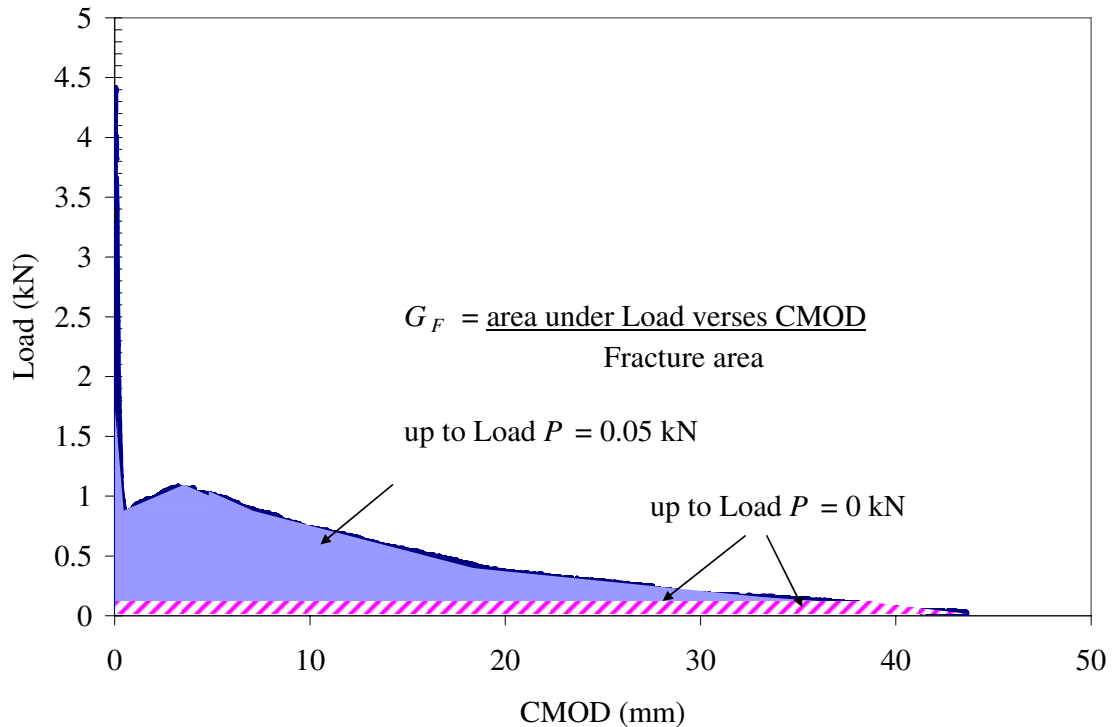


**Figure 7 -  $G_F$  calculation for a straight synthetic FRC specimen.**

All of the testing for projects presented in the remainder of this thesis utilized the TPB specimens for determining fracture properties. The fracture properties were all calculated using the same equations as described earlier, with the exception of a relative fracture energy  $G_{2mm}$  which is explained in Chapter 4. These fracture properties were used to evaluate the effectiveness of different concrete materials for their post-peak performance.

## CHAPTER 3: FRACTURE PROPERTIES OF PAVING MIXTURES

Laboratory research has been performed in this thesis to understand how age of testing, concrete material proportioning and constituent selection affect the concrete fracture properties. Concrete mixtures presented in this chapter were all used in the other chapters' pavement studies or from other researchers. The predictions of concrete fracture properties made by other researchers were also evaluated with the measured data presented herein.

### *Past Studies*

Several researchers have attempted to predict fracture properties with respect to age or material properties. Mindess et al. [35] have reported that the fracture energy did not vary with age, compressive strength, or w/cm ratio but instead depended on the strength of the coarse aggregate. Bazant and Becq-Giraudon [4] performed a statistical study of fracture properties in 2002. They used a database of fracture and strength properties for different specimen types and mixture designs reported in the literature. An equation was developed based on the compressive strength of the concrete  $f'_c$ , the maximum coarse aggregate size  $d_a$ , and the water-cement ratio, to compute the initial fracture energy  $G_f$  and total fracture energy  $G_F$ . Similar equations developed by other researchers were also reported in the Bazant and Becq-Giraudon paper but are not included here. Bazant and Becq-Giraudon described an equation to compute the fracture energy of concrete, shown here as equations 9a and 9b. They reported coefficients of variation of 18 and 30 percent for the initial fracture energy and total fracture energy, respectively.

$$G_f = 1.44 \left( \frac{f'_c}{0.051} \right)^{0.46} \left( 1 + \frac{d_a}{11.27} \right)^{0.22} (w/cm)^{-0.30} \quad (9a)$$

$$G_F = 2.5 G_f \quad (9b)$$

Zollinger et al. [49] conducted age effect testing (at 1, 7, and 28 days) with Texas concrete paving mixtures containing various coarse aggregate sources of crushed limestone or river gravel. The study concluded that the critical stress intensity factor  $K_{IC}$  and the fracture process zone size increased with the age for each concrete mixture. The brittleness of the concrete (computed as the specimen depth divided by the critical effective crack length) was also determined to be greatest at the early ages (before 28 days). For concrete specimens containing river gravel, the critical stress intensity factor was plotted against age, normalized to 28 days, and shown in Figure 8. An empirical formula shown in equation 10 was developed by Zollinger et al. to predict the critical stress intensity factor at different ages ( $t$  in days) based on a 28-day test ( $K_{IC}^{28}$ ).

$$\frac{K_{IC}}{K_{IC}^{28}} = \left( \frac{t}{28} \right)^{1/4} \quad (10)$$

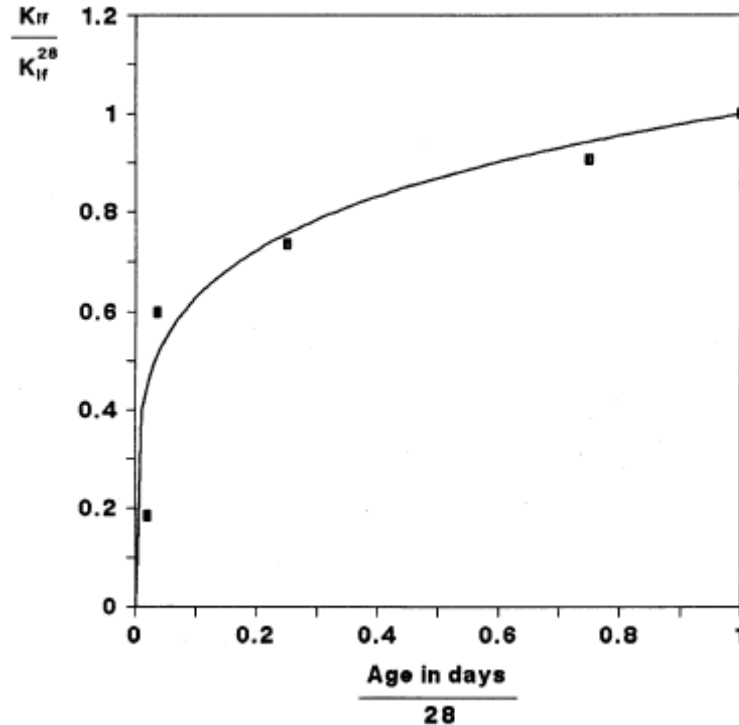


**Figure 8 - Stress intensity factor versus age both normalized at 28 days [from 49].**

### *Chapter Motivation*

The results in this chapter used the concrete mixture designs primarily from the UTW field mixtures (see Table 1) to evaluate the specific influences of age, aggregate type, and cement content on the measured fracture properties. In addition, the equations proposed by Bazant and Becq-Giraudon and by Zollinger et al. to determine fracture properties will also be evaluated. A standardized age for testing fracture properties was also determined in this chapter for paving mixtures used in Illinois.

### *Age Effect Studies*

It is well known that conventional concrete hardened properties such as strength and elastic modulus increase with age. The material properties of a pavement will vary with

time as the concrete continues to hydrate and as climate and traffic loading alters the stresses or strains within the concrete. The strength gain and hydration of concrete are greatly impacted by factors such as temperature, moisture or relative humidity, geometry of the specimen, and microstructure of the concrete. An age effect study was undertaken to verify the evolution of concrete paving mixtures fracture properties for a variety of material constituents and proportions. In addition, it was necessary to analyze concrete paving mixtures with age independent fracture properties. Therefore a standard age should be determined for further fracture testing of concrete mixtures.

The current study included a wide a variety of mixtures, shown in Table 3, using low and high cement contents, a fiber-reinforced concrete mixture, and mixtures containing slag, fly ash, or silica fume. The age effect fracture testing analyzed specimens cured from 7 to 90 days. The Anna and Low Cement mixtures were derived from IDOT ultra-thin whitetopping (UTW) field projects for the intersection project at Vienna and Main Streets in District 9 and the Piatt County Highway 4 project in District 5 (field mixtures shown in Table 1), respectively. The Parking Lot mixture was sampled directly from a field project on the University of Illinois at Urbana-Champaign parking lot E-15. No air entraining agent was added to the Parking Lot mixture in the field according to the ready-mix supplier. The Brazil 1 Mixture is based on SP-280 highway mixture proportions (shown in Table 2) with an adjustment in the coarse to fine aggregate blending and without any water-reducer. The mixture proportions shown in Table 3 have all been normalized to one cubic yard batches of concrete.

The same coarse aggregate type and maximum size (25mm) was used for all mixtures in this age effect study. Other researchers found the coarse aggregate type and maximum size to control the post-peak fracture behavior [4, 35, and 49]; a small research study is described later in this chapter to compare coarse aggregate effects.

**Table 3 - Age Effect Concrete Mixture Designs**

|                   |                    | Anna | Low Cement | Parking Lot | Dan Ryan | Brazil 1 |
|-------------------|--------------------|------|------------|-------------|----------|----------|
| Cement            | lb/yd <sup>3</sup> | 774  | 561        | 434         | 447      | 735      |
| Fly Ash           | lb/yd <sup>3</sup> | 0    | 0          | 135         | 0        | 0        |
| Slag              | lb/yd <sup>3</sup> | 0    | 0          | 0           | 113      | 0        |
| Silica Fume       | lb/yd <sup>3</sup> | 0    | 0          | 0           | 0        | 73       |
| Water             | lb/yd <sup>3</sup> | 280  | 246        | 222         | 236      | 295      |
| Coarse Aggregate  | lb/yd <sup>3</sup> | 1851 | 1924       | 1929        | 1939     | 1761     |
| Fine Aggregate    | lb/yd <sup>3</sup> | 1034 | 1282       | 1231        | 1264     | 1084     |
| Fibers            | lb/yd <sup>3</sup> | 0    | 0          | 3           | 0        | 0        |
| Air Entrainment   | ml/yd <sup>3</sup> | 114  | 83         | 0           | 66       | 271      |
| Water-Reducer     | ml/yd <sup>3</sup> | 172  | 498        | 770         | 397      | 0        |
| Super Plasticizer | ml/yd <sup>3</sup> | 0    | 0          | 0           | 0        | 2391     |
| w/cm ratio        |                    | 0.36 | 0.44       | 0.39        | 0.42     | 0.37     |

All mixtures for the age effect study were tested with the SEN(B), compressive strength, split-tensile strength, and elastic modulus at 7, 28 and 90 days with the exception of the Parking Lot mixture, which came directly from the field and properties were only measured at 7 and 28 days. All mixtures were tested in with the standard beam flexural specimen (ASTM C 78) at the following ages: Low Cement, Dan Ryan and Brazil 1 mixtures at 28 days; Anna mixture at 14 days; Parking Lot mixture at 7 days. The Anna mixture was tested as part of the composite beam studies (see Chapter 5) and therefore also was tested at 14 days for fracture properties. Two specimen replicates were tested

for each hardened property realizing that this would increase the variability in the results but it was important to cast all specimens for one age in one batch. Appendix B lists the equipment used, the number of beam molds available, and the capacity of the concrete mixer.

### ***Age Effect Results***

The hardened property testing plan of for each mixture and batch at the various ages (7, 28 or 90 days) is shown in Table 4. The fresh concrete properties for each concrete batch are presented in Table 4. Each batch of the same mixture proportions produced similar fresh concrete properties which meant that these batches should produce similar hardened properties.

**Table 4 - Age Effect Batch Testing Plan and Fresh Properties**

| Age tested (day)                  |      |        |            |      |             |          |      |          |      |
|-----------------------------------|------|--------|------------|------|-------------|----------|------|----------|------|
| test batch                        | Anna |        | Low Cement |      | Parking Lot | Dan Ryan |      | Brazil 1 |      |
|                                   | 1    | 2      | 1          | 2    | 1           | 1        | 2    | 1        | 2    |
| TPB                               | 7    | 28, 90 | 7, 90      | 28   | 7, 28       | 7, 90    | 28   | 7, 90    | 28   |
| Compression                       | 7    | 28, 90 | 7, 90      | 28   | 7, 28       | 7, 90    | 28   | 7, 90    | 28   |
| Split-Tension                     | 7    | 28, 90 | 7, 90      | 28   | 7, 28       | 7, 90    | 28   | 7, 90    | 28   |
| Elastic Modulus                   | -    | 28, 90 | 7, 90      | 28   | 7, 28       | 7, 90    | 28   | 7, 90    | 28   |
| MOR                               | 7    | 28     | -          | 28   | -           | -        | 28   | -        | 28   |
| Fresh Properties of Each Batch    |      |        |            |      |             |          |      |          |      |
| Slump (in)                        | 2.75 | 2.50   | 5.25       | 5.00 | -           | 1.00     | 1.50 | 9.50     | 9.75 |
| Unit Weight (lb/ft <sup>3</sup> ) | 148  | 147    | 144        | 144  | -           | 148      | 150  | 129      | 136  |
| Air Content (%)                   | 3.8  | 3.7    | 6.0        | 6.3  | -           | 3.7      | 2.8  | 13.3     | 10.3 |

### Load versus CMOD curves

The loads versus CMOD curves for the TPB specimens of each mixture in the age effect study are shown in Figures 9 through 11 at 7, 28 and 90 days, respectively. The Brazil 1 mixture contained a high amount of entrained air which caused the consistently low peak load compared to other mixtures. The post-peak behaviors of all curves, with the exception of the FRC (Parking Lot) mixture, were similar.

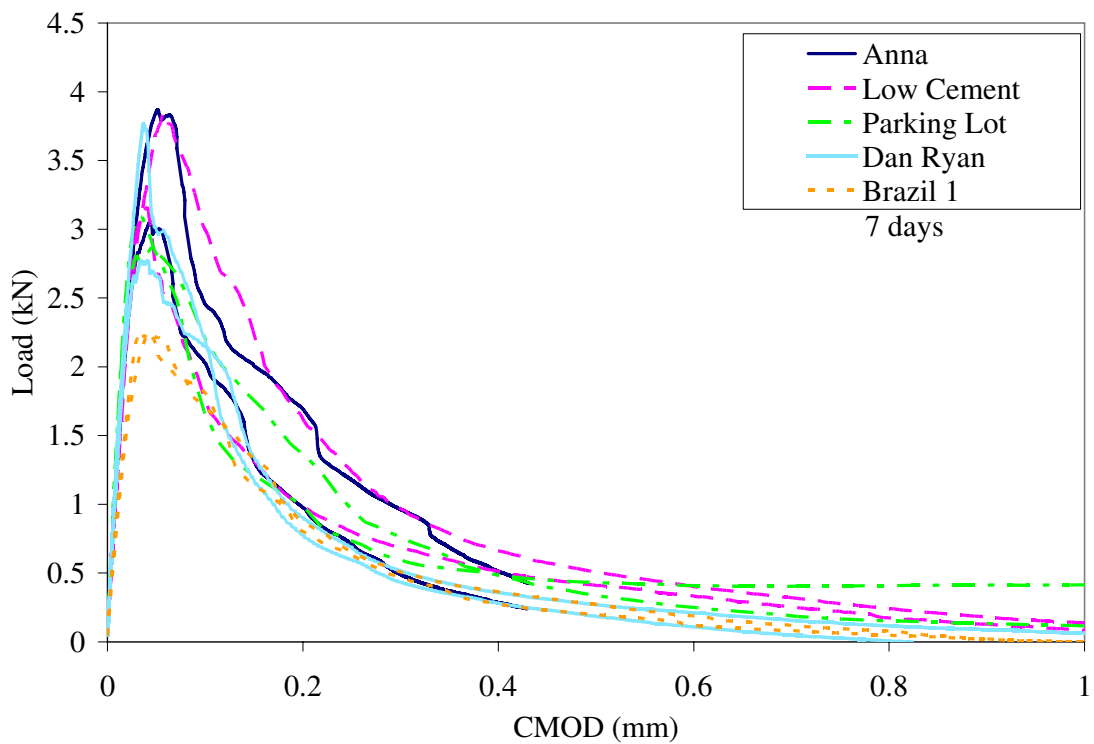


**Figure 9 – Load versus CMOD curves for TPB specimen at 7 days.**

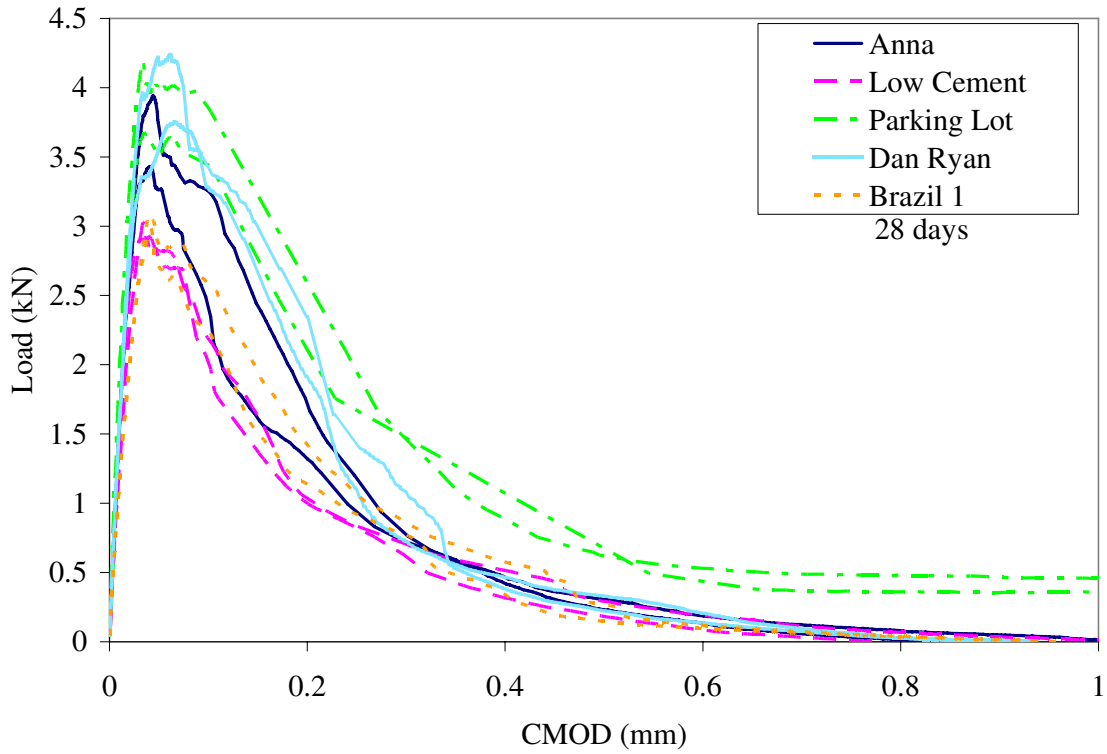


**Figure 10 - Load versus CMOD curves for the TPB specimen at 28 days.**

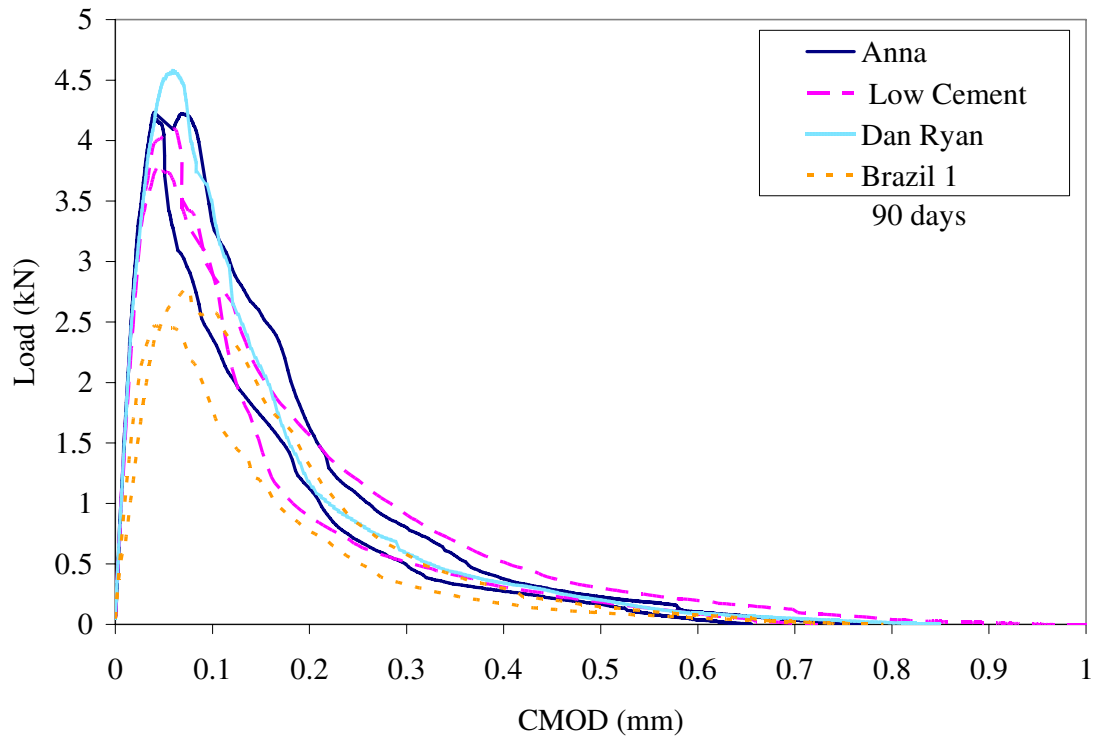


**Figure 11 - Load versus CMOD curves for the TPB specimen at 90 days.**

The CMOD value at specimen failure decreased with age from about 1 mm to 0.6 mm seen in Figures 9 and 11, respectively. This behavior corresponded to an increase in peak strength and toughness of the specimens and an opening width reduction with age. The reason the CMOD at failure decreased with age was the ITZ became stronger with time and therefore the concrete began fracturing through the bulk matrix and aggregates. Specimens at 90-days all showed a flat fracture plane through the aggregate and bulk matrix, while 7-day specimens showed a tortuous fracture path around the aggregates.

### *Measured Properties*

A summary of the strengths and fracture properties (averaged from two specimens) of the age effect study can be seen in Table 5. The coefficient of variation (COV) is also presented in Table 5 for each measured property. Overall the fracture and strength properties increased with specimen age as expected. A comparison between compressive strength to split-tensile strength, peak load and initial fracture energy is shown in Figure 12. There were a few discrepancies in strength gain such as Brazil 1 specimens had a higher average compressive strength at 28 days and the Low Cement specimens had a higher average split-tensile strength at 28 days. For both of these cases, the 28-day specimens were cast in a separate batch than the 7- or 90-day specimens which could be impacted by the altered air contents or consolidation differences used to cast the specimens from each batch. The Brazil 1 mixture had very high air contents and there was 3% less air in the 28-day specimens which likely led to the increased compressive strength.

**Table 5 - Age Effect Strength and Fracture Properties**

|                                  | Age (day) | Anna<br>COV |     | Low Cement<br>COV |     | Parking Lot<br>COV |     | Dan Ryan<br>COV |     | Brazil 1<br>COV |     |
|----------------------------------|-----------|-------------|-----|-------------------|-----|--------------------|-----|-----------------|-----|-----------------|-----|
| Compressive Strength (ksi)       | 7         | 5.60        | 0%  | 4.17              | 6%  | 3.65               | 12% | 4.41            | 6%  | 3.65            | 9%  |
|                                  | 28        | 6.46        | 10% | 4.90              | 5%  | 5.22               | 3%  | 6.17            | 4%  | 5.93            | 0%  |
|                                  | 90        | 7.28        | 5%  | 5.90              | 3%  | -                  | -   | 7.16            | 5%  | 5.26            | 1%  |
| Split-Tensile Strength (psi)     | 7         | 513         | 33% | 360               | 9%  | 436                | 17% | 520             | 0%  | 338             | 24% |
|                                  | 28        | 549         | 15% | 536               | 14% | 573                | 5%  | 524             | 3%  | 508             | 14% |
|                                  | 90        | 662         | 4%  | 512               | 10% | -                  | -   | 640             | 8%  | 541             | 11% |
| $P_c$ (kN)                       | 7         | 3.46        | 17% | 3.51              | 14% | 2.98               | 5%  | 3.27            | 22% | 2.26            | 0%  |
|                                  | 28        | 3.69        | 10% | 2.98              | 3%  | 3.94               | 10% | 4.00            | 9%  | 3.04            | 2%  |
|                                  | 90        | 4.20        | 1%  | 3.95              | 5%  | -                  | -   | 28.23           | *   | 2.63            | 8%  |
| $CTOD_C$ (mm)                    | 7         | 0.023       | 16% | 0.017             | 30% | 0.010              | 11% | 0.016           | 30% | 0.019           | 16% |
|                                  | 28        | 0.016       | 13% | 0.018             | 41% | 0.015              | 21% | 0.029           | 13% | 0.013           | 1%  |
|                                  | 90        | 0.024       | 40% | 0.022             | 7%  | -                  | -   | 0.025           | *   | 0.023           | 13% |
| $K_{IC}$ (MPa m <sup>1/2</sup> ) | 7         | 1.07        | 16% | 0.966             | 15% | 0.74               | 5%  | 0.93            | 7%  | 0.67            | 8%  |
|                                  | 28        | 1.05        | 1%  | 0.910             | 16% | 1.14               | 0%  | 1.37            | 1%  | 0.79            | 1%  |
|                                  | 90        | 1.32        | 14% | 1.21              | 2%  | -                  | -   | 1.42            | *   | 0.78            | 7%  |
| $G_f$ (N/m)                      | 7         | 50          | 32% | 43                | 40% | 22                 | 3%  | 35              | 10% | 28              | 8%  |
|                                  | 28        | 40          | 7%  | 34                | 22% | 47                 | 2%  | 68              | 2%  | 32              | 4%  |
|                                  | 90        | 60          | 32% | 54                | 14% | -                  | -   | 72              | *   | 40              | 11% |
| $G_F$ (N/m)                      | 7         | 83          | 22% | 127               | 23% | 164                | 19% | 99              | 14% | 83              | 6%  |
|                                  | 28        | 115         | 2%  | 89                | 13% | 1,140              | 20% | 135             | 5%  | 102             | 11% |
|                                  | 90        | 102         | 20% | 131               | 12% | -                  | -   | 141             | *   | 92              | 20% |

\* one beam was omitted due to testing errors.

*Initial Fracture Properties*

In general, the peak loads obtained in the fracture testing show a similar trend with age as the compressive strengths, see Figure 12b. Based on the data in Table 5, little difference could be seen in the magnitude of initial fracture property results ( $G_f$ ,  $K_{IC}$ ,  $CTOD_C$ ) between mixtures at any age. On average for all the mixtures, 75% of the fracture and strength properties were realized by 7 days and 85% by 28 days. The initial fracture energy of the Parking Lot mixture (containing fiber reinforcement) doubled between 7 and 28 days.

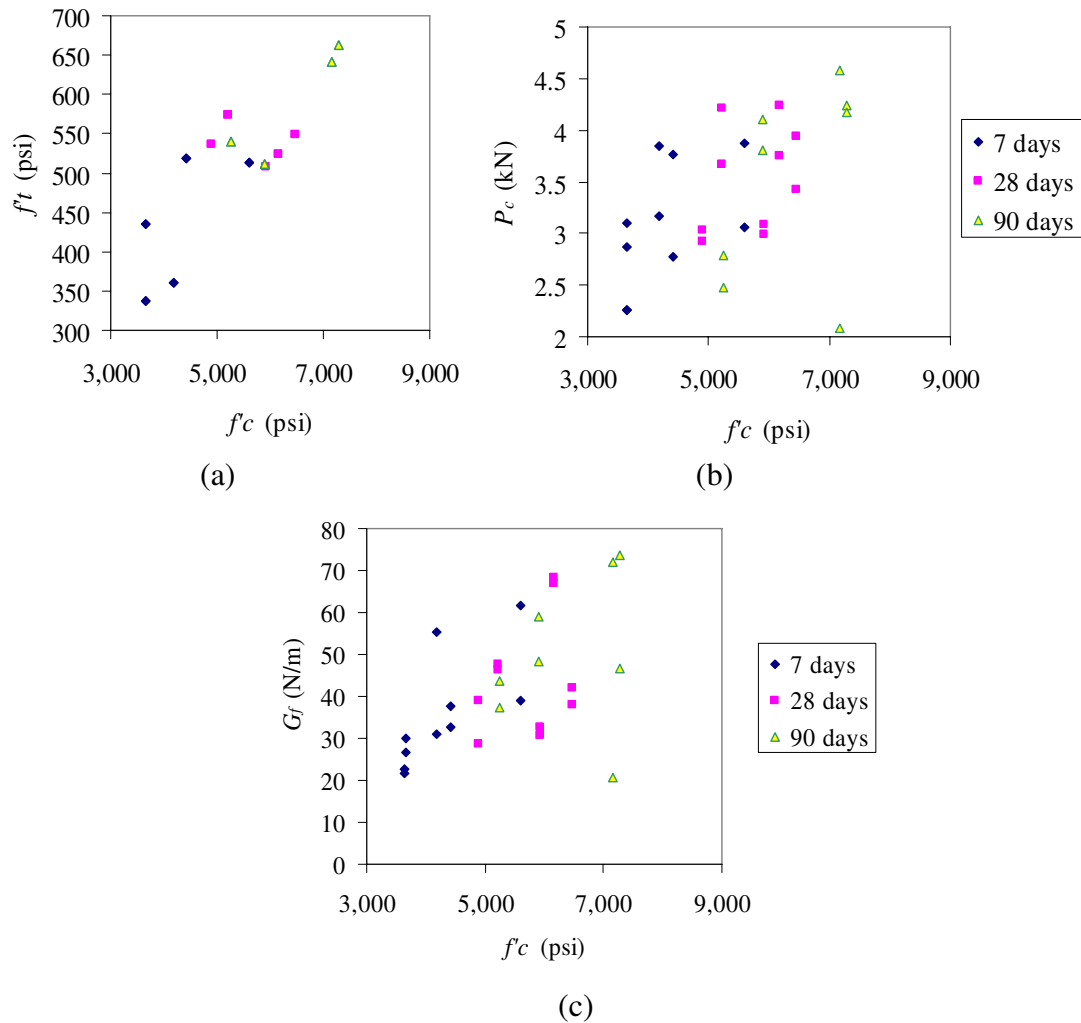


**Figure 12 – (a) Split-tensile strength and (b) TPB specimen peak loads and (c) initial fracture energies compared to compressive strength.**

### *Total Fracture Energy*

For the un-reinforced concrete mixtures, the total fracture energy did increase with age and ranged in values between 83 N/m to 141 N/m. The total fracture energy of the FRC mixture (Parking Lot) increased by almost seven times between 7 and 28 days. The FRC mixture used in the Parking Lot was significantly higher in total fracture energy than other un-reinforced concrete mixtures at 28 days. Slight variation in crack propagation seen in the load-CMOD curves may produce the variation in total fracture energy seen in

Table 5; again porosity caused from air voids or large aggregates found in the fracture plane may also contribute to variation in the total fracture energy.

### *Stress Intensity Factor*

For the mixtures studied in this report, a plot to compare stress intensity factor versus age is shown in Figure 13. The study previously mentioned by Zollinger et al. [49], proposed equation 10 be used to determine the critical stress intensity factor at different ages. This trend line (raised to the 0.25 power) fit the river gravel data from the Zollinger et al. study shown in Figure 8, but does not match all the mixtures tested in this age effect study for the age range of 7 to 90 days. The change in properties after 7 days is much less than Zollinger's model would predict. A shallow trend was plotted against the Zollinger et al. trend line in Figure 13 to more accurately match some of the data here; the shallow trend line proposed altered equation 10 such that the ratio of  $(t/28)$  was raised to a value between 0.05 rather than 0.25. It should be noted that Zollinger's equation was originally based on fracture toughness data at 1, 7, 14, 21, and 28 days, which was different than the time horizon used in this testing program.

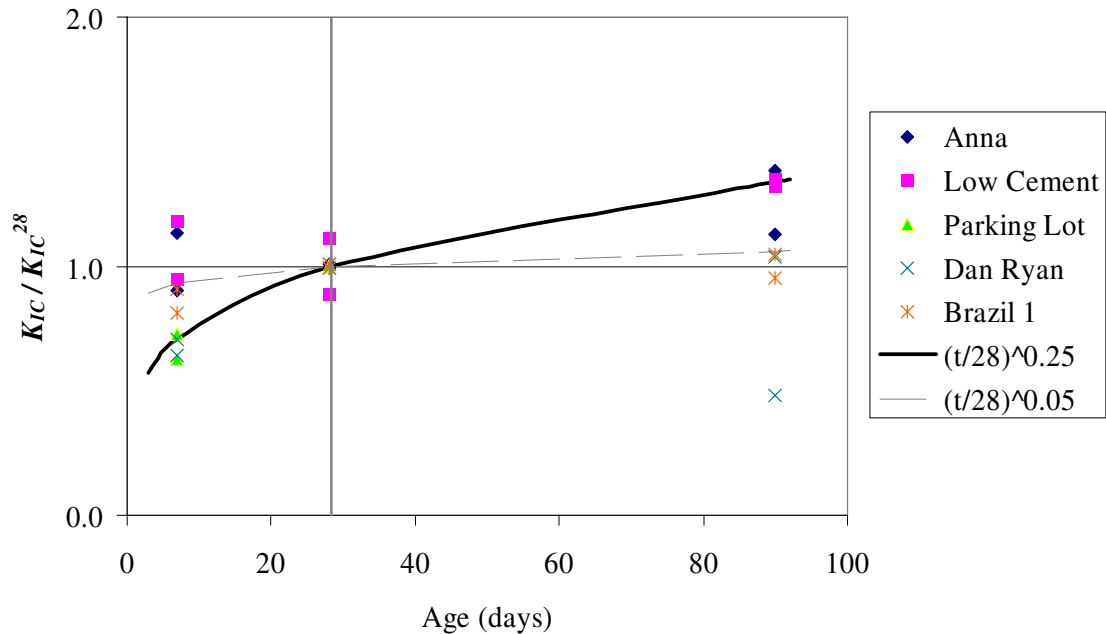


**Figure 13 - Stress intensity factor verses age for various mixtures.**

#### *Sample Preparation and Variability*

Specimens from different batches often demonstrated different fracture properties. For example, the 7-day Anna specimens showed higher initial fracture property results than the 28- or 90-day specimens. Opposite of the strength gain seen in the Low Cement specimens, the 28-day fracture properties such as  $G_f$ ,  $K_{IC}$ , and  $G_F$  decreased from the 7-day results (possibly driven by the increased air voids or some casting issue). The Brazil 1 mixture 28-day specimens also showed higher  $K_{IC}$ , and  $G_F$  values than at 90-days.

Bazant and Becq-Giraudon determined in a statistical study that the COV for initial and total fracture energy were on the order of 18 and 30 percent, respectively [4]. Table 5 supports previous researcher findings that fracture properties have large COV [4 and 6]. In fact, the  $CTOD_C$  values had the greatest average COV, followed by  $G_f$  and  $G_F$ . The 7-day fracture test results demonstrated high coefficients of variability (see Table 5) for the

material properties desired, compared to the 28- and 90-day testing. These results support other research literature findings that fracture properties can have larger coefficients of variability, especially at early ages.

### *Summary*

One of the main goals of the age testing with the TPB specimens was to determine the optimum age for fracture testing of concrete materials. Like strength testing, fracture properties increase with age, and therefore some change in properties with time was expected. It was determined that an age such as 28 days would be more appropriate to use as a reference time since the coefficient of variability after this point in time was relatively lower and little change occurred between 28 and 90 days.

### ***Mixture Proportioning Effects***

The choice in material proportioning can affect some of these properties; for example, higher cement contents tend to increase shrinkage within the concrete, although it may also aid in increasing the compressive and tensile strength and initial fracture energy of the concrete as well. Material type selection can also be important, for example, coarse aggregate type, proportion, and maximum size will have an effect on the hardened concrete properties and can even have a larger impact on the fracture behavior of the concrete pavement.

In this research, no specific mixture proportioning factorial was designed to examine the optimum mixture design proportions for maximum fracture properties for rigid paving mixtures. However, the various mixtures used in this research were chosen based on their diversity in mixture constituents and/or proportioning and the fact that they had been used for some type of rigid pavement project in the field. For example, the Anna mixture was selected to compare fracture properties with higher cement contents relative to lower cement contents (see Table 3 for Anna and Low Cement mixture proportions). The Brazil 1 mixture contained silica fume and it was derived from the SP-280 highway project (Sao Paulo, Brazil), which required high early strength concrete. The Dan Ryan mixture provided an alternative comparison with its use of slag to replace a percentage of cement with a similar total cementitious content as the Low Cement mixture. The Parking Lot mixture incorporated fly ash as a supplementary cementitious material and included fiber-reinforcement. The following sub-sections describe the mixture proportioning effects.

#### *Cement content*

There should be enough cement to cover all of the aggregates or fibers in the mixture and to meet the design and opening strength. However, the high cost of cement and the hydration products potential to shrink upon drying typically results in specifications to minimize the amount of cement in the mixture. Cementitious contents for these studies ranged from approximately 560 to 570 lb/yd<sup>3</sup> for the Dan Ryan, Low Cement and Parking Lot mixtures up to 774 lb/yd<sup>3</sup> and 808 lb/yd<sup>3</sup> for the Anna and Brazil 1 mixtures, respectively.



### *Coarse-Fine Aggregate Ratio*

The coarse and fine aggregates could be volumetrically optimized for maximum packing density. Ideally, the maximum packing density was the most economically viable to obtain the minimum volume of required cementitious material to fill voids (cement was the most expensive component). This optimized packing density was impacted by the gradation curves and aggregate surface texture [35]. For the mixtures examined here, the coarse-fine aggregate volume ratio ranged from 1.46 in the Low Cement mixture to 2.00 in the Brazil 1 mixture (as a note, the original Brazil SP-280 mixture suggested a high coarse-fine aggregate volume of roughly 2.37). A value around 1.50 of the coarse-fine volume ratio was determined to be a typical optimum value for crushed limestone and natural sand available in the laboratory. The coarse-fine aggregate ratio has been determined to affect the amount of interfacial transition zone (fines have more surface area and thus produce more ITZ in concrete) and porosity (higher for lower densely packed concrete), and as a result alter the strength of a concrete [35]. No specific study on the affect of coarse-fine aggregate ratio was performed here; therefore its effect on the fracture properties of concrete has not been determined at this time.

### *Aggregate Type*

The type of coarse aggregate used in concrete affects the workability, strength and crack tortuosity [35]. The influence of aggregate type on fracture properties was investigated by comparing the crushed limestone used for the majority of mixtures with other collected UIUC laboratory data that used recycled concrete aggregate and river gravel.

The bulk specific gravity and absorption capacity and gradation curves of these coarse aggregates are shown in Table 6 and Figure 15, respectively. For comparison, the gradation curve for the natural sand used as a fine aggregate is also provided in Figure 16. The physical properties of the fine aggregate sand are also listed in Table 6. River gravel was known to have a high stiffness; a Los Angeles abrasion test value for river gravel was 18 signifying its resistance to abrasion compared to 29 for crushed limestone [14]. Recycled concrete used as a coarse aggregate or fine aggregate replacement could produce concretes with strength and stiffness reductions by as much as 2/3 of a natural aggregate and typically have significantly higher absorption capacities [35].

**Table 6 - Aggregate Properties**

|                   | BSG <sub>SSD</sub> | Absorption Capacity |
|-------------------|--------------------|---------------------|
| Natural Sand      | 2.57               | 1.79%               |
| Crushed Limestone | 2.69               | 1.36%               |
| River Gravel      | 2.67               | 1.60%               |
| Recycled Concrete | 2.42               | 5.27%               |

The crushed limestone available was gap-graded and did not fall within the limits based on IDOT or ASTM standards for coarse aggregates. The river gravel did have a gradation that met IDOT CA11 standards for 3/4 inch maximum aggregate size. The recycled concrete gradation curve, physical properties, and fracture data were determined during a separate study by Cervantes et al. [13]. They were investigating the effects on concrete fracture properties when using of recycled coarse aggregate as a partial or full replacement of crushed limestone coarse aggregate.

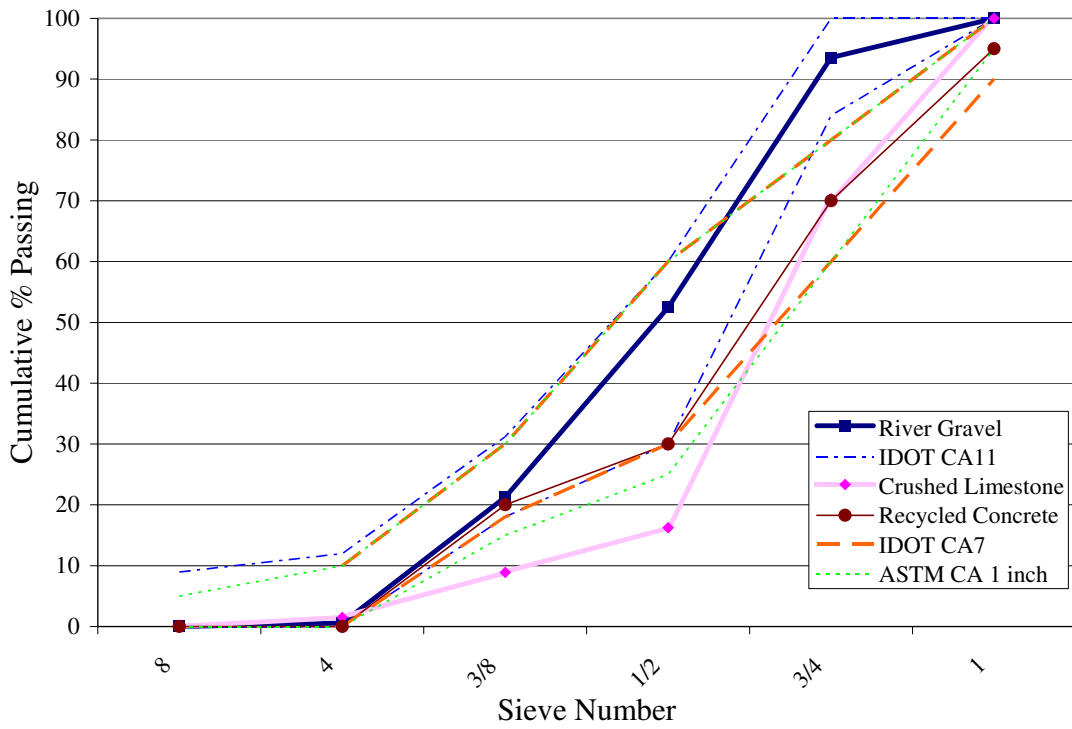


**Figure 15 - Gradation curves for coarse aggregates and corresponding standard limits.**

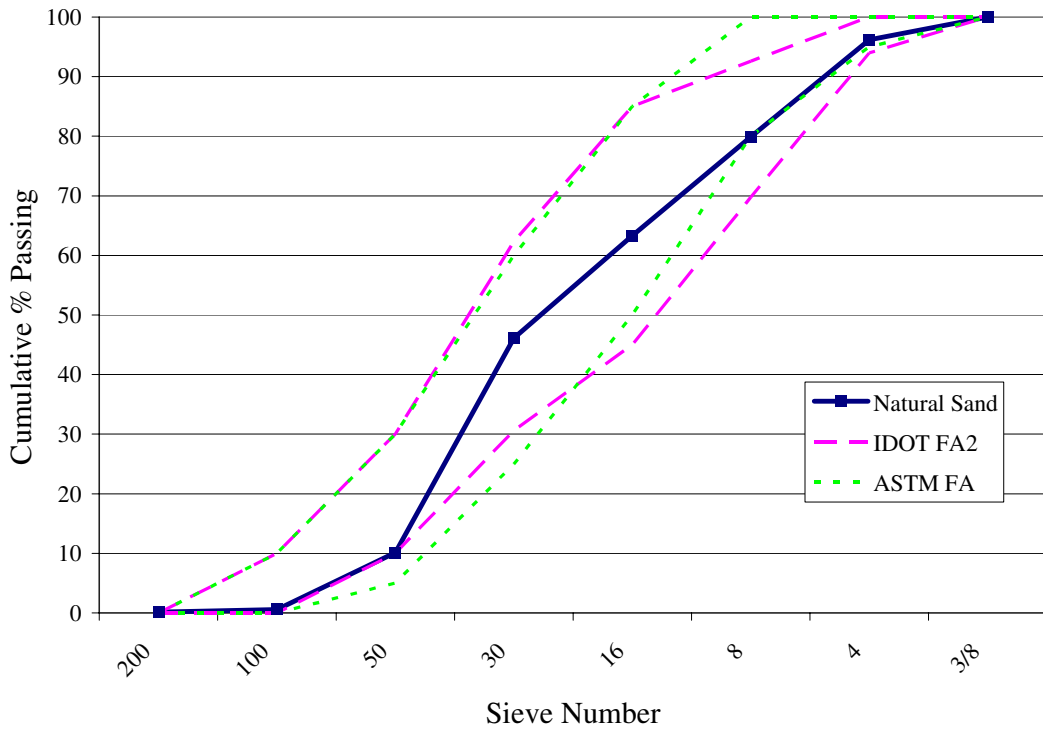


**Figure 16 - Gradation curve for the natural sand and fine aggregate standard limits.**

### *Mixture Designs*

The mixture designs are presented in Table 7 for the concrete mixtures containing different types of coarse aggregates. Using the fracture testing procedure described in Chapter 2, the fracture properties of each mixture containing different coarse aggregates was studied. The Limestone-Recycled Blend contained 50% by volume of crushed limestone and 50% by volume of recycled concrete as coarse aggregate.

### *Load versus CMOD curves*

The load versus CMOD curves for each of these mixtures is shown in Figure 17. The Crushed Limestone 1 mixture was tested at 14 days, the River Gravel mixture was tested at 28 days, and the Crushed Limestone 2, Recycled Concrete and Blend mixtures were all tested at 7 days.

**Table 7 – Concrete Mixture Designs of Different Coarse Aggregates**

| Material Proportions |                    | Crushed Limestone 1 | Crushed Limestone 2 | River Gravel | Recycled Concrete | Limestone-Recycled Blend |      |
|----------------------|--------------------|---------------------|---------------------|--------------|-------------------|--------------------------|------|
| Type I Cement        | lb/yd <sup>3</sup> | 517                 | 607                 | 493          | 607               | 607                      |      |
| Fly Ash              | lb/yd <sup>3</sup> | 140                 | 0                   | 134          | 0                 | 0                        |      |
| Water                | lb/yd <sup>3</sup> | 268                 | 308                 | 255          | 308               | 308                      |      |
| Coarse Aggregate     | Crushed Limestone  | lb/yd <sup>3</sup>  | 1978                | 1645         | 0                 | 0                        | 823  |
|                      | Recycled Concrete  | lb/yd <sup>3</sup>  | 0                   | 0            | 0                 | 1508                     | 754  |
|                      | River Gravel       | lb/yd <sup>3</sup>  | 0                   | 0            | 1886              | 0                        | 0    |
| Fine Aggregate       | Natural Sand       | lb/yd <sup>3</sup>  | 1004                | 1360         | 957               | 1360                     | 1360 |
| Air Entrainer        | ml/yd <sup>3</sup> | 306                 | 0                   | 2            | 0                 | 0                        |      |
| Water-Reducer        | ml/yd <sup>3</sup> | 687                 | 0                   | 0            | 0                 | 0                        |      |

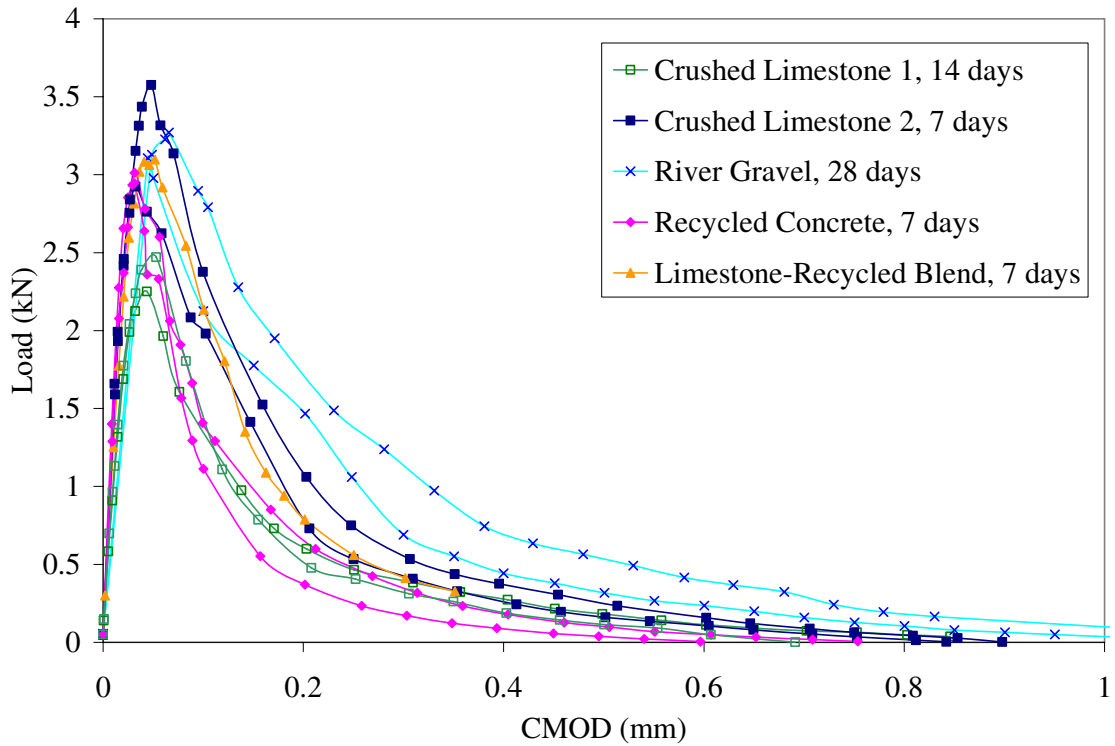


**Figure 17 – TPB concrete specimen load versus CMOD curves for different coarse aggregate types at various testing ages.**

### *Measured Properties*

The concrete fracture properties and strengths are shown in Table 8 for each coarse aggregate type. The River Gravel mixture had the highest strength due to the later testing age. Similarly, the total fracture energy was higher likely due to the later test age, and higher elastic modulus of the river gravel compared to other aggregates. The initial fracture energy and  $CTOD_C$  were not significantly higher for the River Gravel mixture compared to the other mixtures. The Crushed Limestone 1 mixture exhibited the greatest  $CTOD_C$  value and lowest  $K_{IC}$  value at 14 days, which was due to the addition of fly ash and high air entrainment content. By comparing the Recycled Concrete and Crushed Limestone 2 mixtures at 7 days, the values for strength and initial fracture properties are similar. The total fracture energy for the Recycled Concrete mixture was considerably

lower than the Crushed Limestone 2 and Limestone-Recycled Blend mixture due to its lower strength.

**Table 8 - Average Concrete Strength and Fracture Properties for Different Coarse Aggregate Types**

| Mixture                  | Age Tested (day) | Compressive Strength (psi) | Split-Tensile Strength (psi) | $K_{IC}$ (MPa m <sup>1/2</sup> ) | $CTOD_c$ (mm) | $G_f$ (N/m) | $G_F$ (N/m) |
|--------------------------|------------------|----------------------------|------------------------------|----------------------------------|---------------|-------------|-------------|
| Crushed Limestone 1      | 14               | 3,283                      | 332                          | 0.86                             | 0.031         | 43.7        | 60          |
| Crushed Limestone 2      | 7                | 4,528                      | 378                          | 1.12                             | 0.019         | 48.8        | 86          |
| River Gravel             | 28               | 5,232                      | 537                          | 1.10                             | 0.018         | 39.2        | 112         |
| Recycled Concrete        | 7                | 4,030                      | 356                          | 1.09                             | 0.019         | 43.0        | 56          |
| Limestone-Recycled Blend | 7                | 3,328                      | 412                          | 1.03                             | 0.019         | 43.9        | 85          |

*Comparison with Other Coarse Aggregate Studies*

In the previous mentioned study by Zollinger et al. [49], river gravel and crushed limestone mixtures were also investigated for early age fracture properties. The study concludes that the stress intensity factor of the limestone concrete increased more rapidly with age than the river gravel concrete. At 1-day age, the crushed limestone as a coarse aggregate in concrete was tougher (higher  $K_{IC}$ ) than the river gravel coarse aggregate concrete. The study mentioned by 28 days  $K_{IC}$  of crushed limestone and river gravel were roughly the same. Although the crushed limestone and river gravel mixtures tested for this thesis were at different ages, the 7-day Crushed Limestone 2 mixture did show the highest  $K_{IC}$  value which supports findings by Zollinger. Also Zollinger et al. stated the concrete containing limestone aggregate had a fractured surface which showed the

cracks proceeding through the aggregates while the gravel concrete mixture showed very few cracks through the gravel. This fractured surface observation also occurred in the testing performed in the research presented herein.

### *Summary*

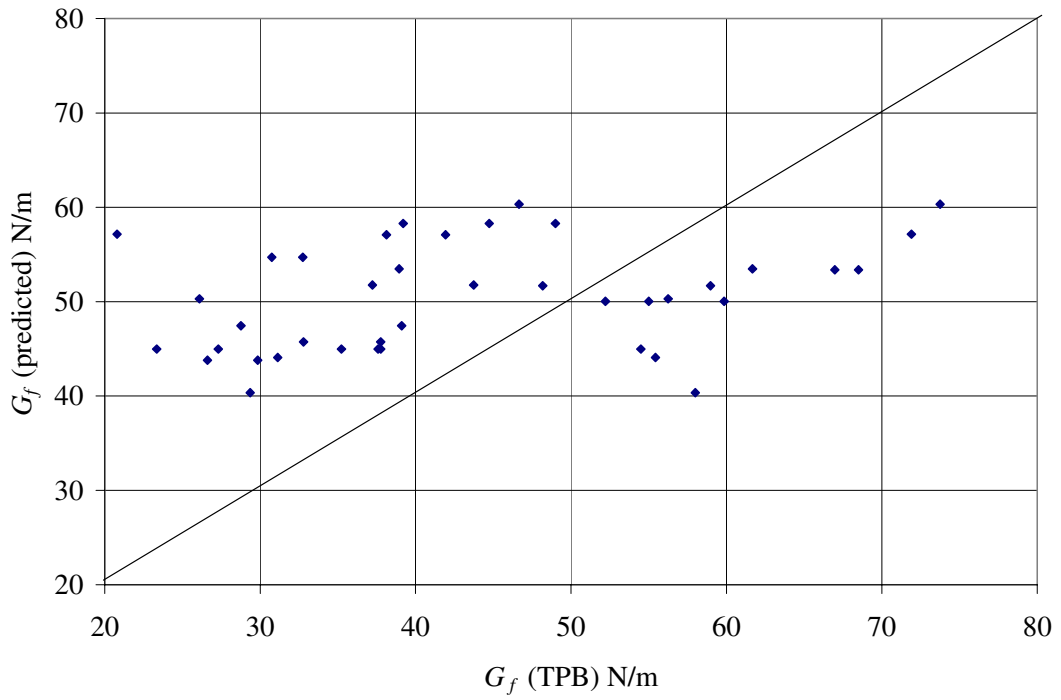
The coarse aggregate properties did have a significant factor on the overall fracture properties. Based on the results found here, the quality or strength of the coarse aggregate is linked with the strength and fracture properties of the concrete. With a river gravel coarse aggregate in concrete fracture was likely to proceed around the aggregate particles through the ITZ thus resulting in lower initial fracture properties compared to crushed limestone coarse aggregate in concrete. Still, the total fracture energy at 28 days was greater with the river gravel coarse aggregate mixture than the other coarse aggregate types tested at earlier ages. Recycled concrete as a coarse aggregate reduced the overall strength and fracture properties of the concrete. However, with at least 50% replacement with crushed limestone aggregate, the recycled concrete coarse aggregate specimens resulted in roughly the same fracture properties as the 100% crushed limestone aggregate mixture.

### ***Prediction of Fracture Energy***

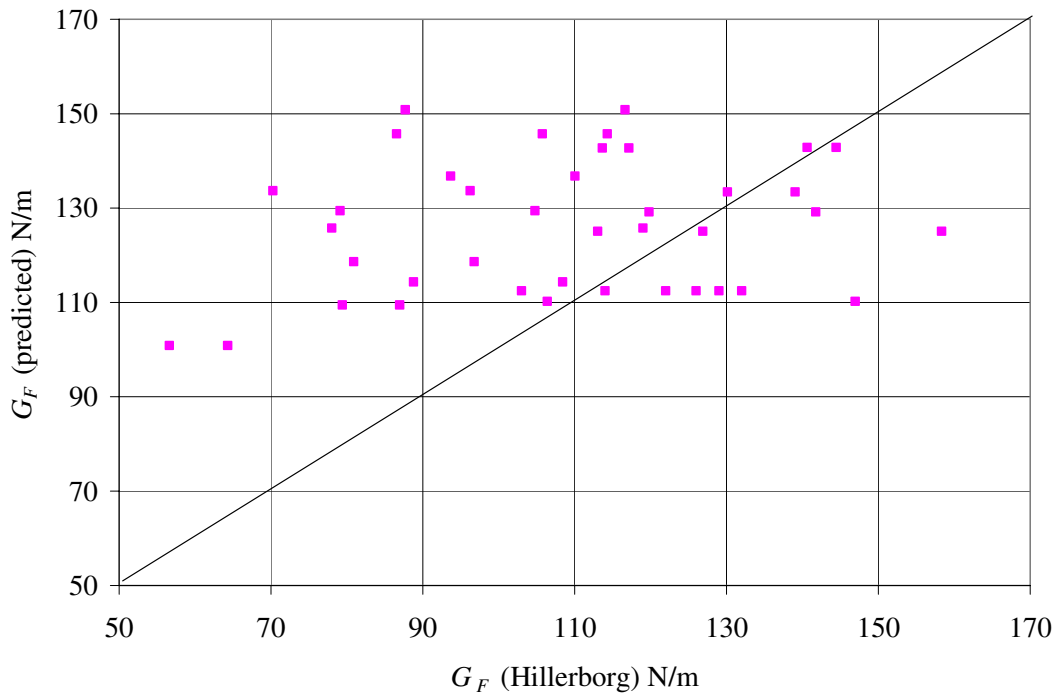
As mentioned in the background to this Chapter, Bazant and Becq-Giraudon performed a statistical study on fracture properties of un-reinforced concrete [4]. Equations 9a and 9b were developed to predict fracture properties from compressive strength, maximum

aggregate size, aggregate type, and water-cement ratio. These equations have been compared with the test results of all the un-reinforced concrete mixtures containing crushed limestone coarse aggregate studied in this thesis, and are shown in Figure 18.

As seen in Figure 18, no correlation was found between the Bazant and Becq-Giraudon equations for fracture energies and the actual measured fracture energies of the concrete mixtures in this thesis. One note here is the only inputs of the Bazant and Becq-Giraudon equation which varied were water-cement ratio and compressive strength. It is suggested that some of the other factors mentioned in this chapter, such as cement content, coarse-fine aggregate ratio, or age of testing could be used to supplement the existing input variables presented in the existing Bazant and Becq-Giraudon to predict the concrete fracture properties. Since the mixtures tested were not designed to derive a predictive equation, there is little confidence that a statistically relevant equation could be derived for all the variables used in the testing to predict the concrete fracture properties.



(a)



(b)

**Figure 18 - Predicted fracture properties versus measured properties for (a) initial fracture energy and (b) total fracture energy.**

## **CHAPTER 4: FUNCTIONALLY GRADED CONCRETE MATERIALS (FGCM)**

The investigation of fracture behavior of functionally graded concrete materials (FGCM) for use in rigid pavements is presented in this chapter. A layered combination of plain and fiber-reinforced concretes in different depth locations with respect to a pre-cut notch was studied. The mixtures, configurations, strength and fracture testing results using plain concrete and synthetic FRC were computed and presented. A summary of the work can be found in Roesler et al. [42]. Additional testing using plain concrete and crimped steel FRC configurations were run by Victor Cervantes in the summer of 2005. The findings from a finite element analysis of the system, developed by Dr. Glaucio Paulino and Kyoungsoo Park [37, 38, and 42], are presented in this chapter.

### ***Background***

A leading problem in the design and performance of concrete pavements today is the diminishing availability of high quality materials. Meanwhile, demands have increased on constructing, maintaining, or repairing pavements in order to improve performance and extend pavement life. As good quality materials are reduced, lower quality or even recycled materials are often used in replacement because of their availability and cheaper cost for initial construction. The lower quality materials could lead to more distresses in the pavement at a shorter pavement life if the properties of the lower quality constituents are not better characterized or possibly modified. This concept is clearly understood by

agencies and researchers who have been studying and developing specifications for the use of recycled asphalt pavement.

One solution for this problem is to implement a functionally graded or layered pavement system. Functionally graded materials (FGM) are most commonly used in metals and ceramics for high-tech applications. A FGM consists of steady transitions in material microstructure or composition to meet functional requirements and enhance the overall composite system performance [42]. This innovative approach can be applied to pavement design by using layers of different concrete mixtures at specified depths such that the overall structure is cost effective and still has an optimized performance and functionality.

A functionally graded concrete material (FGCM) system could be constructed to incorporate readily available cheaper and lower quality materials along with other better quality materials. The FGCM structure could be constructed as individual layers of concrete placed while the concrete is still plastic to eliminate creating discrete interfaces between layers similar to an extrusion method. Mixture designs for each layer could be specified in order to achieve maximize the local concrete layer and global rigid pavement system performance.

#### *Two-layered Paving Background*

The concept of paving FGCM in layers has been done in Europe, Michigan, Kansas, and other locations in the United States [12] and is typically termed two-layered paving. The

majority of these pavement structures focus on reducing noise and increasing friction by implementing a thin textured surface layer of concrete overlying a thicker standard concrete mixture. One of the challenges brought on with two-layered paving in the United States relate to construction. Some of the projects in the United States have seen non-uniform thicknesses in the top lift causing early-age distresses [12]. A research project by Ravindrarajah and Tam studied the flexural strength and casting delay times for 2-layered and 3-layered steel fiber-reinforced concrete (FRC) beams [40]. The flexural strength increased with increased FRC layer in the tension zone. A short delay of up to 3 hours between casting of layers did not produce a significant change in flexural strength. Overall, very few research studies have been done to date on testing and analyzing the mechanical properties of these layered concrete pavement systems.

### ***FGCM Project Motivation***

Research in this thesis includes a study of the fracture performance of FGCM two-layered composite beams. Fiber-reinforcement can be used in concrete to increase the fracture properties (i.e. toughness) of the material. In order to amplify the range of fracture behavior, steel and synthetic fiber-reinforced concrete mixtures have been investigated compared to plain concrete in various layered combinations. The beams were all tested for initial and total fracture properties. These properties were implemented in a finite element-based model to predict the performance of these FGCM by Park [37 and 38]. The results of the FGCM investigations can be found herein.

## ***Functionally Graded Materials***

### *Mixture Designs*

Concrete beams composed of two layers of concrete materials were tested to determine the viability of functionally graded concrete materials for rigid pavement systems. This research was initiated to look at the necessary fracture characteristics of two-layer paving systems. Several beams were created using a combination of three concrete mixtures: a plain concrete (PCC) and two fiber-reinforced concrete (FRC<sub>PP</sub> and FRC<sub>CS</sub>). The mixture design of the PCC and FRC mixtures used in the FGCM study are shown in Table 9. The fibers used for this project are “straight synthetic” fibers at a volume fraction of 0.78% or 12.1 lb/yd<sup>3</sup> and “crimped steel 1” fibers at 0.5% volume fraction or 65.5 lb/yd<sup>3</sup>. The straight synthetic fibers are 40 mm long rectangular cross-section polypropylene/polyethylene blended fibers with an aspect ratio of 90 and a tensile capacity of 620 MPa. The crimped steel 1 fibers are 50 mm long circular cross-section steel fibers, crimped along the length, with an aspect ratio of 50 and a tensile capacity of 900 MPa. Further fiber property details can be found in Chapter 6. A crushed limestone coarse aggregate was used with a maximum aggregate size of 19 mm along with natural sand and Type I Portland cement. The mixture proportions came from a previous study using 0.48% volume fraction of the same straight synthetic fibers [41].

**Table 9 - Mixture Designs for FGCM in lb/yd<sup>3</sup>**

| Material                  | Plain Concrete | Straight Synthetic FRC | Crimped Steel FRC |
|---------------------------|----------------|------------------------|-------------------|
|                           | PCC            | FRC <sub>PP</sub>      | FRC <sub>CS</sub> |
| Water                     | 308            | 308                    | 308               |
| Type I Cement             | 607            | 607                    | 607               |
| Coarse Aggregate          | 1645           | 1645                   | 1645              |
| Fine Aggregate            | 1360           | 1360                   | 1360              |
| Straight Synthetic Fibers | 0              | 12.1                   | 0                 |
| Crimped Steel 1 Fibers    | 0              | 0                      | 65.5              |

### *FGCM Beam Configurations*

In order to determine the initial fracture properties and total fracture for the concrete in the TPB configuration, the two-parameter fracture model (TPFM) and work-of-fracture method were used as described in Chapter 2. The beam configuration for the layered beams can be seen in Figure 19. To incorporate the layer design, the height of each layer was determined to be half of the effective cross-sectional area. The effective cross-sectional area was computed as  $d - a_0$ . Because the notch depth  $a_0$  was 50 mm of the total depth at 150 mm, the resulting effective cross-sectional area was 100 mm. The height of top layer ( $h_1$ ) was computed to be 50 mm and as a result the bottom layer height ( $h_2$ ) was 100 mm. See Figure 19 for a schematic of the layer heights.

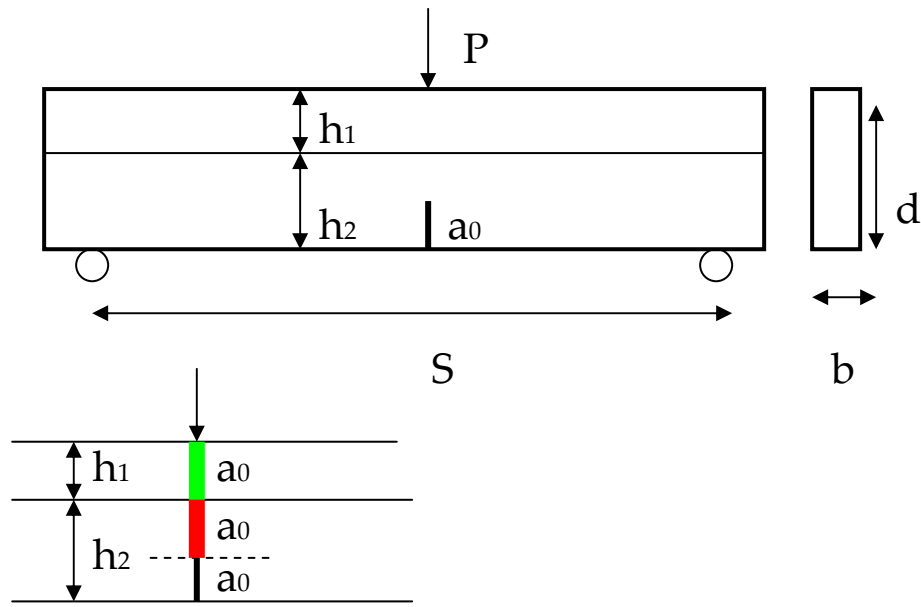


**Figure 19 - Three-point bending beam test setup for functionally layered concrete specimens.**

Four combinations of the PCC and FRC mixtures were used to fill the layers in the TPB beam as shown in Figure 20. As a result full-depth beams of PCC and FRC (Figures 20a and 20b, respectively) were considered as part of the testing plan and also aided as a control for comparison to the beams with the layered FRC and PCC mixtures (Figures 20c and 20d, respectively). Three replicates of each beam configuration were made. Two additional beams containing only FRC were cast to acquire the total fracture energy, which required a yo-yo gauge for the run-out testing.

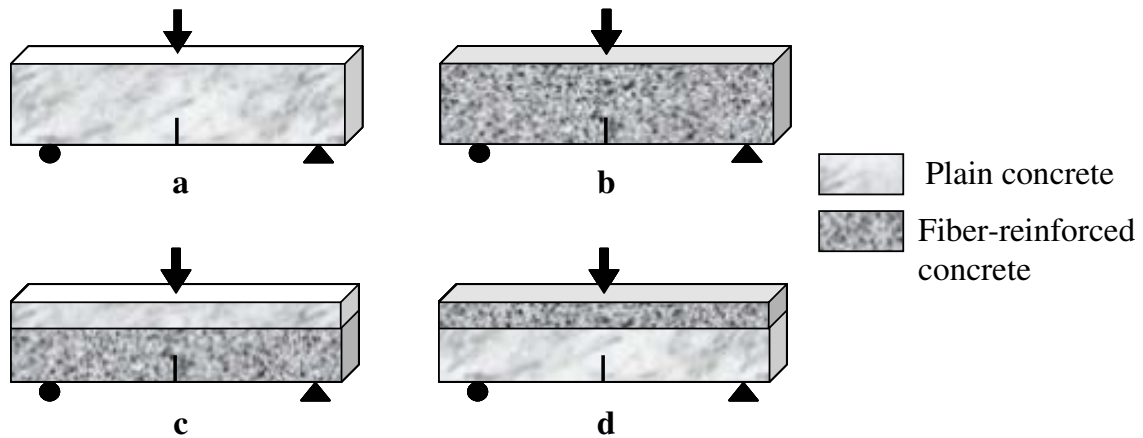


**Figure 20 - FGCM beam configurations: a) PCC/PCC, b) FRC/FRC, c) PCC/FRC, and d) FRC/PCC.**

Batches of each mixture were made on the same day within an hour. Steel molds were filled two-thirds of the depth ( $h_2$ ) with the first mixture and then filled the remaining depth ( $h_1$ ) with the second mixture. Each layer was consolidated into the molds using standard rodding techniques [2]. The second layer was consolidated 25 mm into the bottom layer allowing a graded zone between the two “homogeneous layers.” Specimens were demolded after 1 day then moist cured. The notch was saw-cut one day before testing. Further details of the mixing and testing procedures can be reviewed in Appendix B. For the FGCM study, all the specimens were tested at 7 day.

### ***Functionally Graded Material Results***

The average 7-day compressive and split-tensile strengths of the PCC, FRC<sub>PP</sub>, and FRC<sub>CS</sub> mixtures are shown in Table 10. The addition of fibers did not affect the compressive strength of the plain concrete, but the higher fiber content mixtures resulted in slightly increased split tensile strength over plain concrete which typically is seen when fiber

contents approach 1 percent [35]. In general the slump is reduced with the addition of fibers. However, with the crimped steel 1 FRC mixture the slump actually was significantly higher than expected possibly due to some higher amount of superplasticizer or water-reducer added to the mixture.

**Table 10 - Concrete Mixtures Average Fresh Properties and Strengths**

| Property                          | Plain Concrete | FRC <sub>PP</sub> | FRC <sub>CS</sub> |
|-----------------------------------|----------------|-------------------|-------------------|
| Slump (in)                        | 7.75           | 2.30              | 7.13              |
| Unit Weight (lb/ft <sup>3</sup> ) | 146            | 146               | 148               |
| Air Content (%)                   | 2.68           | 2.06              | 2.90              |
| Compressive Strength (psi)        | 4,799          | 4,551             | 3,458             |
| Split-Tensile Strength (psi)      | 499            | 612               | 619               |

*FRCpp Fracture Envelope Curves*

Figure 21 shows the load versus displacement envelope curves for each beam configuration containing the straight synthetic FRC and plain concrete. The full-depth FRCpp beam has the greatest post-peak load capacity as expected and the full-depth PCC beam is the lowest post-peak load capacity.

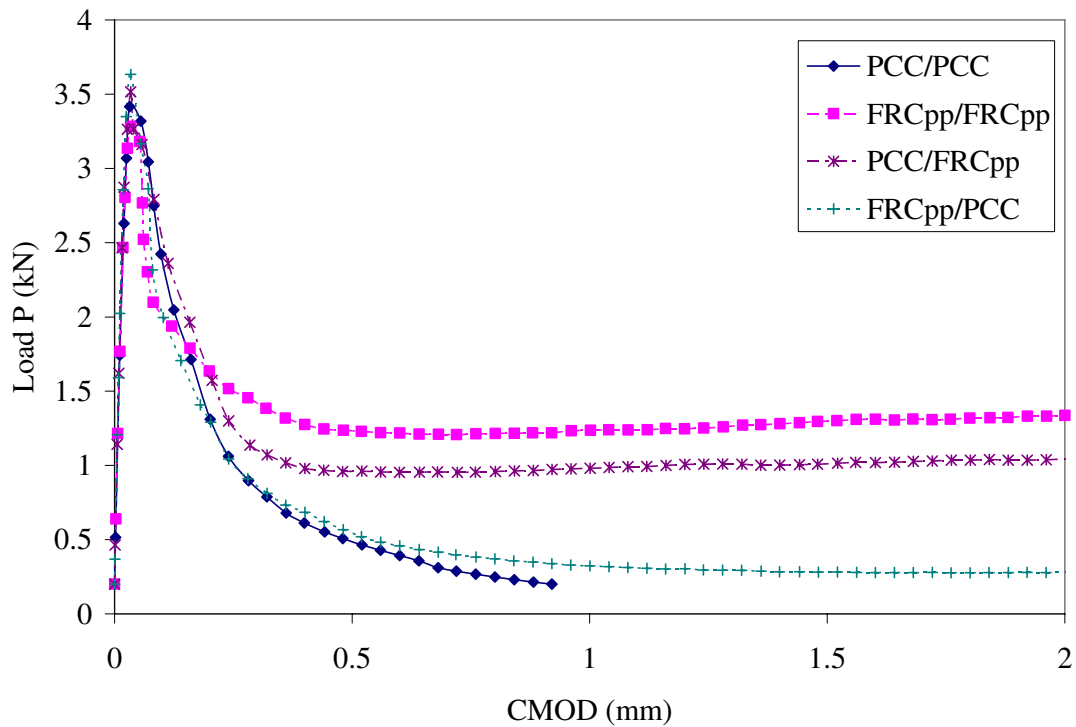


**Figure 21 - Fracture load versus CMOD curves for plain concrete and straight synthetic FRC layer configurations.**

A cut off criterion was used to compare various mixtures that have a large opening displacement capability, like FRC. For this study, a 2mm cut off CMOD was used in calculation of a relative fracture energy  $G_{2mm}$  (see Chapter 2 for computation of total fracture energy  $G_F$ ). The calculation of the fracture energy at 2mm was selected because the maximum desired crack widths for fractured concrete slabs were typically 1 to 2.5 mm. The computation for  $G_{2mm}$  used the same equation as the total fracture energy calculation (equation 8 in Chapter 2) except the area under the curve was only computed up to 2 mm crack mouth opening displacement ( $CMOD_{max} = \delta_f = 2$  mm).

It was estimated that for some FRC mixtures – generally those with higher volume fractions, larger aspect ratios, etc. – the 2mm CMOD cut off was too small to capture any

secondary peak in the load-CMOD curves (see Figure 9). Further discussion about this secondary peak behavior in FRC mixtures is explained in Chapter 6. The 2mm cut off fracture energy  $G_{2mm}$  was considerably less than the total fracture energy  $G_F$  obtained and there was no direct relation between these values because of the dependency on the fiber properties. However, the  $G_{2mm}$  values computed were significant enough based on the test results for the specific fiber used here that it was able to provide insight into the effectiveness of the fiber when dispersed in concrete. Even for the two layered beams the test results up to 2mm represented significant differences between the various configurations and the importance of the fiber-reinforcement location with respect to a crack or notch.

Table 11 presents the average  $P_c$ ,  $K_{IC}$ ,  $CTOD_C$ ,  $G_f$ , and  $G_{2mm}$  results obtained from SEN(B) layered specimens. The FRCpp/FRCpp and PCC/FRCpp specimens had significantly better fracture behavior ( $G_{2mm}$  increased by 2.9 times) especially after the post-peak load as compared to plain concrete (PCC/PCC) as seen in Table 11. Specimens with PCC on top and straight synthetic FRC on the bottom (PCC/FRCpp) had a higher  $G_{2mm}$  than samples with straight synthetic FRC on top and PCC on the bottom (FRCpp/PCC). The addition of straight synthetic fibers to the bottom or top layer improved  $G_{2mm}$  by 108 and 80 percent, respectively, in comparison to PCC/PCC.

**Table 11 - FGCM Average Fracture Properties**

| Top / bottom layer     | $P_c$ (kN) | $K_{IC}$ (MPa·m <sup>1/2</sup> ) | $CTOD_c$ (mm) | $G_f$ (N/m) | $G_{2mm}$ (N/m) |
|------------------------|------------|----------------------------------|---------------|-------------|-----------------|
| PCC / PCC <sup>1</sup> | 3.71       | 1.01                             | 0.016         | 38.3        | 120             |
| FRCpp / FRCpp          | 3.48       | 1.03                             | 0.016         | 37.1        | 381             |
| PCC / FRCpp            | 3.71       | 1.08                             | 0.017         | 40.5        | 249             |
| FRCpp / PCC            | 3.57       | 0.96                             | 0.016         | 35.4        | 216             |
| PCC / PCC <sup>2</sup> | 3.30       | 0.93                             | 0.016         | 33.4        | 116             |
| FRCcs / FRCcs          | 2.75       | 0.84                             | 0.018         | 29.1        | 318             |
| PCC / FRCcs            | 2.50       | 0.69                             | 0.019         | 29.3        | 153             |
| FRCcs / PCC            | 3.10       | 0.85                             | 0.014         | 30.0        | 389             |

<sup>1</sup> PCC tested with the other FRCpp configurations

<sup>2</sup> PCC tested with the other FRCcs configurations

#### *FRCcs Envelope Curves*

Figure 22 shows the load versus CMOD curves for the crimped steel 1 FRC and plain concrete configurations. The full-depth FRCcs beam still produced a large residual load capacity and fracture energy. As seen in Table 11, the  $G_{2mm}$  for the FRCcs full-depth beam increased by 2.7 times the plain concrete full-depth beam. However, the specimens with FRCcs in the compression zone of the fracture area (top third) and PCC on the bottom actually produced the greatest post-peak load performance. This is unexpected because the full-depth FRCcs specimens in theory should have produced the greatest fracture energy. It was noticed after the testing was complete, that very few steel fibers actually bridged the fracture plane with the TPB beam size chosen. At volume fractions less than 0.5%, the steel FRC beams have too much variation because of the low number of fibers bridging the plane. The load is significantly influenced at these low volume

fractions of steel fibers by each individual fiber pulling out of the matrix – hence the bumpy envelope curve of the crimped steel beams.

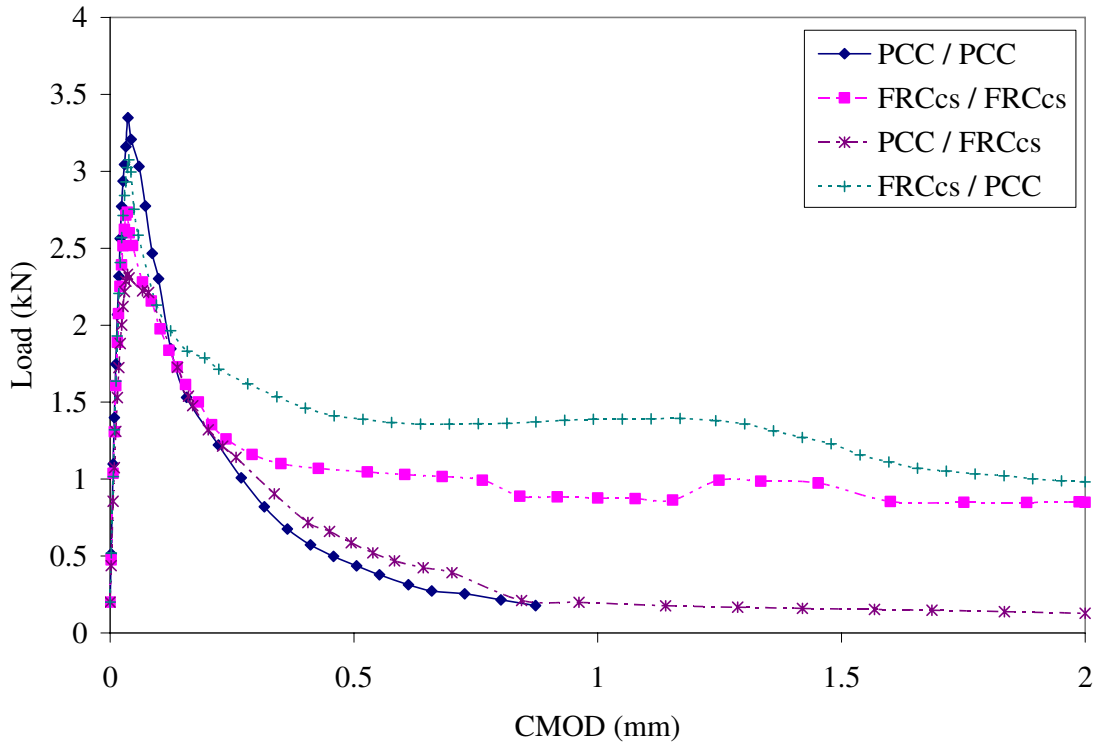


**Figure 22 – TPB specimen load versus CMOD curves for plain concrete and crimped steel FRC layer configurations.**

#### *FGCM Fracture Properties*

The use of fibers did not significantly affect the peak load of the specimens, and subsequently did not significantly change the calculated  $K_{IC}$ ,  $G_f$ , and  $CTOD_C$  as seen in Table 11. It is important to notice that  $K_{IC}$ ,  $CTOD_C$ , and  $G_f$  were related just to the stage of crack initiation instead of crack propagation, which is why the initial fracture properties did not differ much since the same concrete constituents and proportions were used for both the PCC and FRC specimens. The relative fracture energy at 2mm opening ( $G_{2mm}$ ) was used to describe the post-peak fracture behavior for smaller crack widths.

This relative total fracture energy is described later in this chapter. The full-depth FRC mixtures had greater  $G_{2mm}$  than the full-depth plain concrete mixtures as expected.

### *Synthetic versus Steel*

In general, the strength and fracture properties for the straight synthetic FRC combinations were higher than for the crimped steel 1 FRC combinations. The straight synthetic FRC beam (full-depth) had greater  $G_{2mm}$  than the crimped steel 1 FRC beam. For the straight synthetic fiber configurations, the magnitude of the relative fracture energy in increasing order was the following: PCC/PCC < FRCpp/PCC < PCC/FRCpp < FRCpp/FRCpp. The order of increasing relative fracture energy is different for the crimped steel 1 FRC beam configurations: PCC/PCC < PCC/FRCcs < FRCcs/FRCcs < FRCcs/PCC. Again note that the FRCcs full-depth beam should have produced the largest relative fracture energy. The straight synthetic fiber appears to have improved fracture properties when the fibers are located near the crack tip while the crimped steel fiber appears to improve fracture properties when located away from the crack tip. Also the straight synthetic FRC mixtures showed more repeatable results due to the higher concentration of fibers bridging the fracture plane compared to the crimped steel FRC mixtures. As shown in Chapter 6, the softening curve of concrete containing crimped steel fibers has a much larger variability than other fiber types.

The beams with crimped steel FRC on the top (FRCcs/PCC) had a higher  $G_{2mm}$  than samples with crimped steel FRC on the bottom (PCC/FRCcs). This behavior was different from the straight synthetic FRC configuration. One reason suggested for this

effect was the top FRCs layer created a plastic hinge when the crack intersects the layer, which maintains a constant residual load for large CMOD deformations. Again due to the low number of fibers bridging the fracture plane, with the FRCs as the bottom layer, very few steel fibers were able to pull out of the matrix and thus the beam behavior was quite similar to that of the un-reinforced PCC beams. Also with the synthetic fibers, there were significantly a greater number of fibers that actually bridged the fracture plane, which increases the frictional pullout load.

#### *Total Fracture Energy*

For modeling the fracture behavior of the FRC, the total fracture energy ( $G_F$ ) of the straight synthetic FRC full-depth beams (FRCpp/FRCpp) until complete failure (shown in Figure 23) was needed. No full-depth crimped steel 1 FRC beams were tested until complete failure. However, Chapter 6 investigates the TPB fracture behavior of the crimped steel 2 FRC, where crimped steel 2 fiber had a semi-circular cross-section and shorter length compared to the spherical cross-sectioned crimped steel 1 fiber. The total fracture energy of a full depth FRCpp beam was 3,531 N/m which was 29 times greater than the full-depth plain concrete beam. The FRC beams had not broken in half by the time the test was ended at a load of 0.05 kN at CMOD readings around 45 mm.

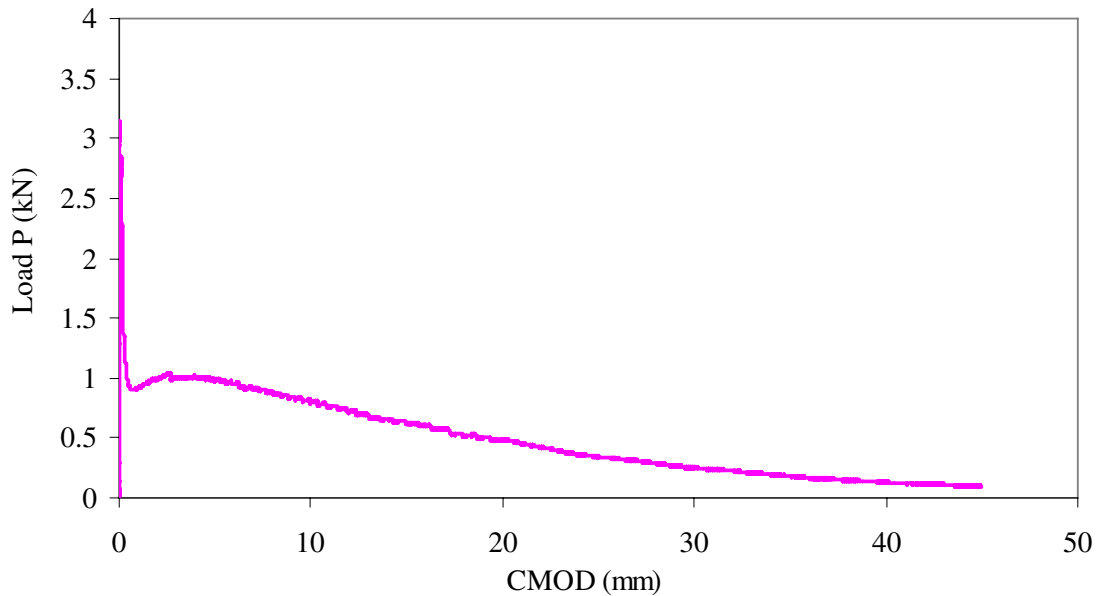


**Figure 23 - FRC TPB Specimen Load versus CMOD curve carried out to specimen fracture ( $P = 0.05$  kN).**

### *Finite Element Analysis*

As complementary part of this FGCM study, a numerical model of the fracture behavior of these functionally graded composites was conducted under the direction of Dr. Glaucio Paulino and completed by graduate student Kyoungsoo Park at the University of Illinois [37 and 38]. This modeling was not done as part of this thesis, but the primary purpose of this section was to summarize the numerical findings so that future researchers could readily implement the appropriate modeling techniques.

Models to describe the fracture process or tension softening curve of each material must be chosen and implemented. For plain concrete, a bilinear softening curve has been found to be sufficient for modeling plain concrete [37, 38, and 42] based on the initial

and total fracture energy ( $G_f$  and  $G_F$ ) and the tensile strength  $f'_t$  of the concrete mixture. Different models exist to describe the performance of FRC mixtures; a summary of several available FRC micromechanical models are provided in Appendix A. Recent work by Park et al. [38] has clearly demonstrated that a bilinear softening model was sufficient for plain concrete but this same model could not be used for fiber-reinforced concrete materials (see Figure 24). Park et al. [38] have proposed a trilinear softening model also in Figure 24, which has reasonably described the fracture behavior of straight synthetic FRC materials in the TPB configuration.

The trilinear model developed by Park et al. captures the post-peak fiber bridging behavior of the FRC mixture much better. This trilinear model requires an additional parameter to describe the curve which in this case was the final crack width  $w_f$ . The value for this final crack width is not agreed upon in the literature [42]. Various FRC models (see Appendix A) suggest that the final crack width be equal to half the embedment length or  $L_f/2$ . However, a value of  $L_f/4$  was suggested by Park et al. [38] to capture the entire envelope curve for low volume straight synthetic FRC. Two values of the final crack width,  $L_f/2$  and  $L_f/4$  were chosen for comparison with the results of the FRCpp data in the FGCM testing. As seen in Figure 24, the softening curve using this crack width matches the data closely for small crack width openings. However in order to capture the entire fracture curve of the FRC mixture, a maximum crack width of  $L_f/4$  shows a closer match up to 40mm CMOD for the global response.

The FEM cohesive zone model shown in Figure 25 closely matches the beam results of the FGCM seen in Figure 21. The trilinear softening the FRCpp mixture using a final crack width of  $L_f/4$  slightly overestimates the envelope curve at small crack opening displacements and therefore shows a slightly higher curve for all the layered beams and full-depth FRCpp beam. The global curve seen in Figure 25 for the FRCpp/FRCpp and PCC/FRCpp (“FRC on the bottom”) beam configurations shows the same kinking behavior at about half of the peak load indicating the onset of the fiber pull-out response occurring at the same point in the crack propagation process. Similarly the FRCpp/PCC (“FRC at the top”) and PCC/PCC beam configurations have a low kinking point load level, in the global load-CMOD curve, indicating that the fiber pull-out force does not impact the global response until larger crack opening widths. No finite element analysis was performed to date to confirm the results from the crimped steel 1 FRC and plain concrete configurations due to the high variability of the steel fracture properties for low volume fractions.

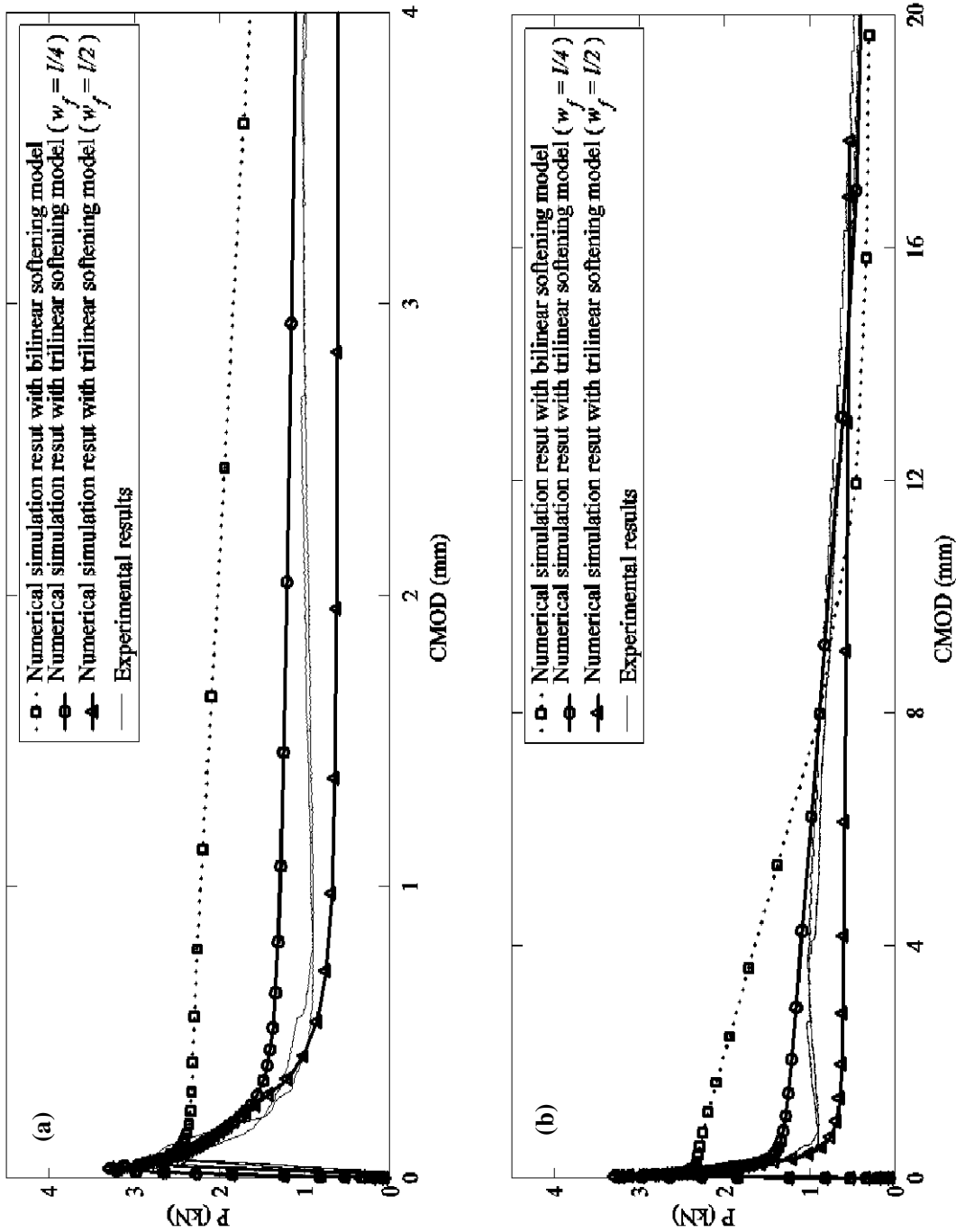


Figure 24 - Simulations of the FRC results using various models (a) up to 4mm CMOD and (b) full range of CMOD [from 42].

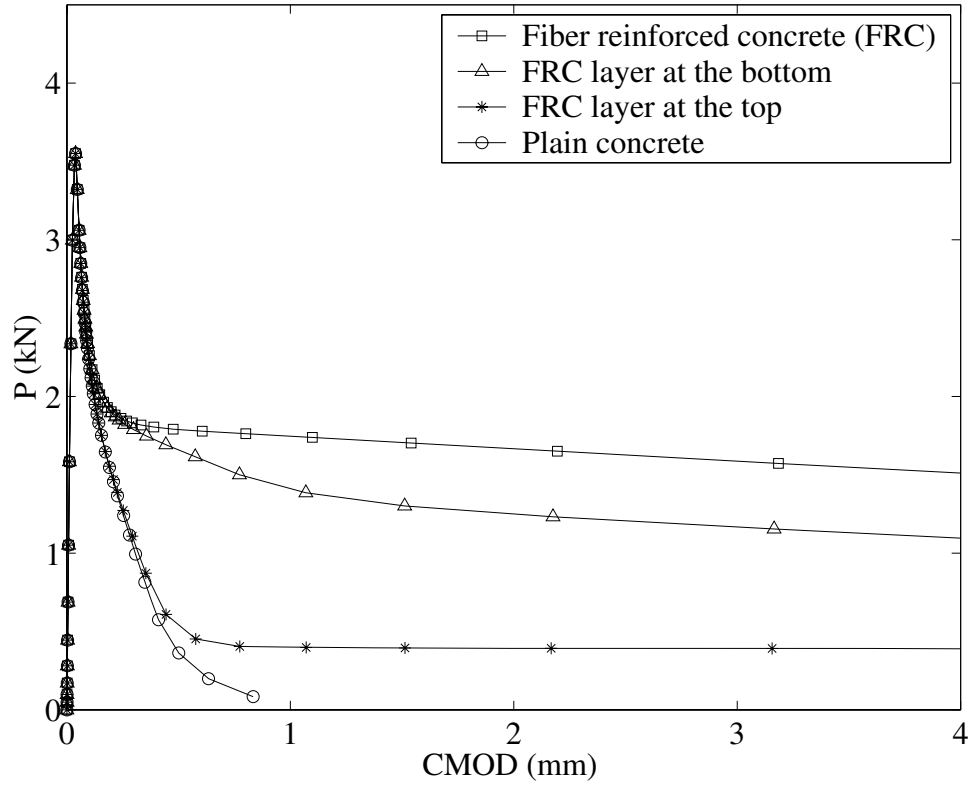


Figure 25 - Simulation using the trilinear softening ( $w_f = L_f/4$ ) model for FGCM combinations using FRCpp and plain concrete [from 42].

## **CHAPTER 5: COMPOSITE BEAM TESTING**

Ultra-thin whitetopping pavements are a rehabilitation technique requiring very thin concrete slabs to be cast on distressed hot-mixed asphalt pavement. An investigation of these pavement materials has been made in this chapter, specifically to gain insight into the composite section behavior. The fracture behavior and shrinkage properties of several of these mixtures have also been analyzed and presented herein.

### ***Background***

Whitetopping is a rigid pavement rehabilitation consisting of a new concrete pavement overlaid on an existing flexible pavement structure. Whitetopping is an alternative rehabilitation technique to hot-mix asphalt overlays given there is a minimum asphalt concrete thickness for support and sufficient vertical clearance for a concrete overlay. These concrete overlay designs are either bonded or unbonded concrete overlays depending on the thickness of the concrete slabs. In general, whitetopping may provide a greater cracking resistance, durability, and surface reflectivity relative to hot-mix asphalt concrete. Furthermore, in situations where the hot-mix asphalt pavement shows signs of surface distresses, especially rutting, whitetopping is an effective solution rather than a hot-mix overlay.

Whitetopping is classified based on the concrete thickness and concrete/hot-mixed asphalt bonding condition in the pavement structure. Conventional whitetopping is

designed and constructed as a normal new concrete pavement section except it is placed over existing flexible pavement and a negligible bond condition is assumed. Ultra-thin whitetopping (UTW) is designated for whitetopping pavements between thickness of 3 and 5 inches and a bonded interface between the concrete and asphalt concrete layer. Some researchers have refer to UTW projects as “bonded concrete resurfacing of asphalt pavements” to distinguish it from other concrete overlay types [36]. Due to high surface to volume ratios thin and ultra-thin whitetopping are made with smaller slab sizes. The smaller slab size reduces the moisture and temperature curling and load stresses on the concrete pavement. The slab size, saw-cut timing and bond issues are important design parameters that must be addressed during construction of ultra-thin whitetopping pavements. Currently no quantitative condition assessment of the existing hot-mix asphalt pavement exists and no universal concrete mixture designs required to assure adequate performance of these concrete rehabilitation strategies are accepted.

#### *IDOT UTW Projects*

Several concrete mixture designs, thicknesses, and construction techniques have been recommended or developed since the 1990s for UTW. The American Concrete Pavement Association (ACPA) has been collecting information about UTW projects in the United States since 1991 and has developed design guidelines based on field, laboratory and analytical studies [20]. Since 1998, Illinois Department of Transportation (IDOT) began paving several whitetopping projects in locations throughout the state at intersections and mainline roads. IDOT implemented the whitetopping projects on low and moderate traffic volume roads. A study to develop guidelines for future whitetopping designs was

initiated by IDOT. The study investigated 10 ultra-thin whitetopping projects throughout the state of Illinois [47]. The mixture designs of these UTW projects (as of 2005) are shown in Table 1. Several of the pavements have showed significant distresses as early as 3 years of service life, while other pavements are currently still in service with little to no distresses. The early and severe distresses may have been caused from several sources (mixture design selection, bonding conditions, underlying condition of the existing hot-mixed asphalt pavement, heavy vehicular traffic, etc).

### *Global UTW Projects*

UTW has been experimented with in pavement projects around the world. For example, a study in Brazil investigated two UTW projects using high strength concrete [39]. The University of São Paulo campus roadway has performed with little distresses, while a nearby UTW on SP-280 highway was severely distressed after a short service life. The mixture designs used for two UTW projects in Brazil can be seen in Table 2. In Taiwan, high early strength concrete was used which resulted in alligator type fatigue cracking occurring in the UTW section after 2 months of service [33].

Part of the research objectives was to evaluate more ideal concrete mixtures for UTW pavements. Although the Dan Ryan mixture (shown in Table 2) was designed for a highly trafficked highway (with express and local lanes for traffic control) near Chicago, IL, it was recreated in the laboratory to evaluate the fracture properties. The Dan Ryan mixture also contains low cement content and ground granulated blast furnace slag as a supplementary admixture.

### *Motivation*

To understand what mixture design parameters resulted in undesirable performance issues seen in certain field projects, a study of the strength and fracture properties of various mixture proportions and constituents was undertaken. The field mixture designs listed in Tables 1 and 2 have been repeated or adjusted in order to be reproduced in the laboratory at the University of Illinois at Urbana-Champaign. The primary study investigated a selective set of mixtures in a composite beam on an elastic foundation system. The composite beam consisted of concrete cast directly on a notched asphalt beam and recorded vertical deflections of the entire section (concrete, asphalt and the soil) along with estimated crack opening displacements in the concrete. In addition, various material properties including shrinkage, fracture toughness, and fracture energy were measured to characterize the behavior of each mixture.

### ***Composite Beam Test***

A comparison some of the IDOT mixture designs used in whitetopping project around the state of Illinois [47] were replicated in the laboratory in order to measure both the fracture behavior and shrinkage characteristics of the materials. Strength, fracture, and shrinkage properties were used to understand what mixture design parameters may cause the undesirable performance issues of the field UTW pavements. From all of the mixture designs of whitetopping projects IDOT has already paved (see Table 1), two of these (Schanck Avenue project in Mundelein and the intersection project in Anna) were selected for composite beam testing (concrete over cracked hot-mixed asphalt concrete).

Schanck Avenue was a fiber-reinforced concrete pavement cast in 2005 with no visible distresses to date. The Anna mixture used higher cement content and was placed in an intersection. The Anna test section showed a high frequency of cracking after 3 years of service.

### *Initial Concept*

The concept of testing of a composite beam concept began in spring 2006 as a class project at the University of Illinois. Two students in the course, Tursun [45] and Braham [7], worked on the effects of mixture designs changes on composite pavement fracture response.

The project by Tursun looked at concrete overlays of hot-mixed asphalt concrete (HMAC). A HMAC beam was mixed and compacted, then cut to the dimensions of 3x3x15 inches. In addition, half of the HMAC compacted beams had aluminum foil placed vertically in the center of the beam. This foil was removed later to simulate a crack in the asphalt pavement. Concrete beams were also cast separately using 6x6x21 inch molds and later cut to the following beam dimensions: 3x3x15 inches. The composite beam was tested on a rubber pad of roughly 1 inch thickness. The test setup for this initial composite testing of a concrete overlay on asphalt can be seen in Figure 26. An 11-kip MTS machine applied the load while an LVDT measured the vertical deflection of the concrete beam at midspan. Plain and fiber-reinforced concrete mixtures were used for the original work.

This study by Tursun found that higher peak loads (by 1.5 to 1.65 times) resulted when the HMAC beams were un-notched compared to the notched beams. No significant change in peak load was seen between the plain and FRC samples. The plain concrete samples showed a significant drop in load by about 80%, while the FRC samples only dropped by 50 to 60% in load after the beams cracked.



**Figure 26 - Initial composite (concrete on asphalt) beam test setup [from 45].**

The preliminary research by Braham [7] conducted a similar test to the previous setup but consisted of two concrete beams separated by one inch of HMAC as shown in Figure 27. The concrete beams were cast using wooden molds and then cut to the dimensions of 2.5 inches x 4 inches x 15 inches. The lower concrete layer was saw-cut in half for all specimens to simulate a joint at midspan of the specimen. The HMAC was mixed and compacted directly onto the concrete beam. The top concrete beam was then placed unbonded on the asphalt/concrete composite beam. The whole composite section was again tested on a rubber pad with an 11-kip MTS machine. Steel knife-edges were epoxied to the concrete at the bottom crack location. A 4mm range clip gauge was placed across this location to measure the crack opening width of the bottom layer concrete (see

Figure 27). The vertical displacement of the whole composite section (concrete, asphalt, and rubber pad) was measured using a midspan LVDT as seen in Figure 27.



**Figure 27 - Initial composite (concrete on concrete) test setup [from 7].**

The study by Braham concluded that the peak loads remained roughly consistent between each specimen tested. Polymer-modified asphalt as an interlayer between the concrete beams did not show significant changes to the load, but did slightly increase the CMOD readings upon cracking. When FRC was used instead of plain concrete, the load reduction after cracking was significantly less and CMOD values upon cracking were also increased.

#### *Revised Concept*

Results from the initial concept showed the concrete and asphalt mixture both can impact the overall load versus vertical deflection curves. An initial finite element model of this test configuration by graduate research assistant Kyoungsoo Park proved to be difficult mostly because of the nonlinear response offered by the rubber pad. Another challenge that needed to be addressed was due to the bonding between the concrete and asphalt

layers. Because no mechanical or chemical means were used to bond the top concrete layer to the hot-mix asphalt interlayer, the concrete layer would immediately slip and lift off from the underlying hot-mix asphalt layer during testing. This behavior resulted in high contact stresses near the midspan of the beam.

A new test setup concept was developed which replaced the rubber pad with a clay soil box of known properties. To simplify the test, composite beams similar to Tursun's project were made, except the concrete would be cast directly onto the HMAC layer. The HMAC would all come from one source to avoid variability in materials. A 1-year old asphalt pavement slab that was compacted with regular construction equipment was used to cut-out the required beam sizes. The concrete was cast directly onto the HMAC layer to avoid any initial slippage and lift off issues caused from the bending of the beam. The concrete mixture designs used for the surface layer were replicates of UTW field projects funded by IDOT.

#### *Soil box*

A soil box was manufactured using 2x4 wood for support and lined with 3/4-inch plywood on the inside. The inner dimensions of the box were 12 inches high, 8 inches wide, and 20 inches long. A schematic and photo of the soil box along with a photo of soil compaction are shown in Figure 28.

The box was painted on the inside, and two layers of a black plastic sheeting of 3 mils were stapled to the frame; these were used to make the plywood more water-resistant in

case of leakage. Roughly an inch of the bottom was filled uniformly with  $\frac{3}{4}$ -inch size recycled concrete which would serve as a water-table basin. A double-layer of burlap was placed at the bottom to separate the water table from the soil. In addition to the water table, two small PVC pipes were added at opposite corners of the box to provide a location to add water directly to the water table basin. The 10-inch layer of clay was constructed using trowels, rods, and hand compaction. The Mexico clay (from Missouri) was made assuming an optimal compacted density of  $114 \text{ lb/ft}^3$  at optimum moisture of 15%. This clay was used in a previous project at the University of Illinois [41]. A thin layer of sand was added to the top to maintain a level surface and to hold in moisture.

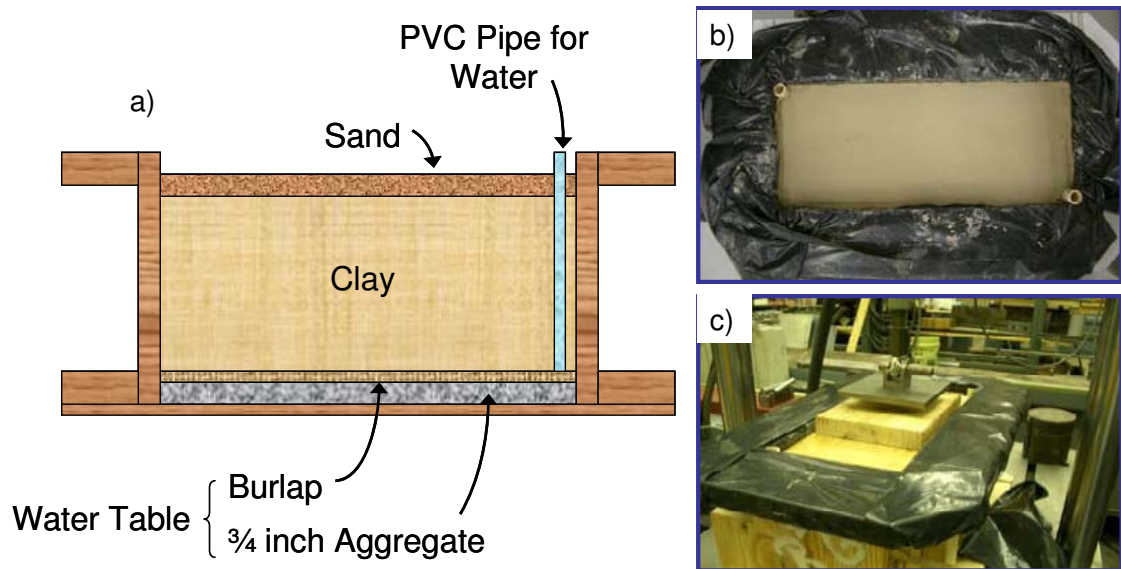


**Figure 28 - a) Schematic of the soil box components for composite testing, b) the top of the soil box and c) compaction of the soil in the box.**

Further compaction (seen in Figure 28c) was made using plywood across the top surface and a metal bar to distribute the load from an 11-kip MTS actuator in the Newmark Civil Engineering Laboratory. Repetitive loads were manually added to compact the clay, each time the soil condensed vertically and then rebound due to the clay's elastic response.

Note the peak loads reached during the composite beam testing was unknown at the time of the soil compaction; a maximum load of 8 lb was applied during the compaction efforts.

### *Ultra-thin Whitetopping Mixtures*

A total of seven composite beam mixtures were created in the lab, these are shown in Table 12. The Schanck Avenue mixture (4 lb/yd<sup>3</sup> of fibers) shown in Table 1, and three mixtures similar to Schanck Avenue – plain concrete without fibers, plain concrete with gravel instead of crushed limestone coarse aggregate, and a mixture with a higher volume fraction of fibers (6 lb/yd<sup>3</sup>) – were created. The Anna mixture was from Table 1 and the Dan Ryan and Brazil 2 mixtures were adjusted from Table 2. Note a different mixture design called Brazil 1 was used in Chapter 3. The final concrete mixture proportions are shown in Table 12 for the composite UTW testing and generally follow the concrete mixture used in the field [47]. All weights shown in Table 12 have been re-adjusted so the total batch volume is 1 yd<sup>3</sup>. It was expected that the Schanck Avenue mixture containing 6 lb/yd<sup>3</sup> would demonstrate the most favorable fracture behavior. In contrast, the fracture behavior of Anna mixture was hypothesized to not perform as well due to the early age distresses on the field sections.

The Schanck Plain, Schanck 4 lb, and Anna specimens were tested at 14 days (testing age chosen because fracture properties were predicted to be more stable after 7 days). The Schanck 6 lb, Schanck Gravel, Dan Ryan, and Brazil 2 specimens were tested at 28 days. In addition to the composite beam tests, the compressive strength, split-tensile strength,

elastic modulus, flexural strength, residual strength, free shrinkage, and fracture properties were also tested. The results of these tests are presented in the following sections.

**Table 12 - UTW Mixture Designs for Composite Beam Testing**

|                   |                    | Schanck Ave |      |      |        | Anna | Dan Ryan | Brazil 2 |
|-------------------|--------------------|-------------|------|------|--------|------|----------|----------|
|                   |                    | Plain       | 4 lb | 6 lb | Gravel |      |          |          |
| Cement            | lb/yd <sup>3</sup> | 517         | 518  | 522  | 493    | 774  | 447      | 748      |
| Fly Ash           | lb/yd <sup>3</sup> | 140         | 141  | 142  | 134    | 0    | 0        | 0        |
| Slag              | lb/yd <sup>3</sup> | 0           | 0    | 0    | 0      | 0    | 113      | 0        |
| Silica Fume       | lb/yd <sup>3</sup> | 0           | 0    | 0    | 0      | 0    | 0        | 75       |
| Water             | lb/yd <sup>3</sup> | 268         | 268  | 271  | 255    | 280  | 236      | 288      |
| Coarse Aggregate  | lb/yd <sup>3</sup> | 1978        | 1982 | 2000 | 1886   | 1851 | 1939     | 1926     |
| Fine Aggregate    | lb/yd <sup>3</sup> | 1004        | 1006 | 1015 | 957    | 1034 | 1264     | 940      |
| Fibers            | lb/yd <sup>3</sup> | 0           | 4    | 6    | 0      | 0    | 0        | 0        |
| Air Entrainer     | ml/yd <sup>3</sup> | 306         | 77   | 77   | 73     | 114  | 66       | 169      |
| Water-Reducer     | ml/yd <sup>3</sup> | 458         | 459  | 0    | 0      | 687  | 397      | 0        |
| Super Plasticizer | ml/yd <sup>3</sup> | 0           | 0    | 463  | 0      | 0    | 0        | 917      |
| w/cm ratio        |                    | 0.41        | 0.41 | 0.41 | 0.41   | 0.36 | 0.42     | 0.35     |

### *Fresh and Hardened Properties*

Table 13 shows the measured fresh and hardened concrete properties of the UTW mixtures. The Anna mixture was also used in the age effect study of Chapter 3, so the corresponding 28 day results are also shown here for comparison. The compressive strength of Schanck Plain mixture was lower than the others. This was the result of the higher air content in the mixture design. The large air entrainer dosage was cut back to reduce the air content for the remaining Schanck mixtures. The slumps of the Schanck 6 lb FRC and Brazil 2 mixtures were extremely low even with the addition of superplasticizer. Due to the rounded, smooth gravel in the Schanck Gravel mixture, no water reducer or superplasticizer was used, which still resulted in a 9-inch slump. The

Anna and Brazil 2 mixtures showed similar 28-day compressive strengths due to their similar cement contents and w/cm ratios. The Schanck 6 lb FRC mixture had a relatively high compressive strength. The Schanck Gravel mixture had a very high elastic modulus of 7,023 ksi after 28 days, which could be attributed to the higher elastic modulus of the gravel coarse aggregates.

**Table 13 - UTW Fresh Properties and Strengths**

|                                   | Schanck |       |       |        | Anna  | Dan Ryan | Brazil 2 |
|-----------------------------------|---------|-------|-------|--------|-------|----------|----------|
|                                   | Plain   | 4 lb  | 6 lb  | Gravel |       |          |          |
| <b>Fresh Properties</b>           |         |       |       |        |       |          |          |
| Slump (in)                        | 5.00    | 4.75  | 1.00  | 9.00   | 3.25  | 4.00     | 1.00     |
| Unit Weight (lb/ft <sup>3</sup> ) | 134     | 143   | 144   | 148    | 146   | 143      | 146      |
| Air Content (%)                   | 10.3    | 5.3   | 4.4   | 2.6    | 4.6   | 6.7      | 2.6      |
| <b>Hardened Properties</b>        |         |       |       |        |       |          |          |
| Age (days)                        | 14      | 14    | 28    | 28     | 14    | 28       | 28       |
| Compressive Strength (psi)        | 3,283   | 5,054 | 5,752 | 5,232  | 4,905 | 6,461    | 6,618    |
| Split-Tensile Strength (psi)      | 332     | 553   | 590   | 537    | 579   | 549      | 533      |
| Elastic Modulus (ksi)             | 3,276   | 4,565 | 4,832 | 7,023  | 4,451 | 4,608    | 4,331    |

### *Composite Beam Testing*

The composite beams were centered on the top of the soil in the box and several gauges were attached as shown in Figure 29. An angle bracket located at the top center of the concrete beam and knife edges spaced 10 mm apart located at the bottom of the concrete layer were mounted with epoxy prior to testing. For space consideration, the angle bracket and knife edges were affixed on opposite sides of the composite beam.

The first LVDT (1-inch range) was rigidly attached to the frame of the machine and measured the total vertical deflection of the composite beam (concrete, asphalt, and soil). A second LVDT (0.1 inch range) was attached to an aluminum frame and measured

vertical deflection between the frame and the angle bracket. This vertical midspan deformation measured only the concrete beam deflection relative to the ends of the concrete layer. The aluminum frame was pinned 1-inch from the ends of the beam and 2.5 inches from the top of the beam as seen in Figure 29. An INSTRON clip gauge (4 mm range) was placed between the knife edges to give an estimate of the crack tip opening displacement for any cracks that would initiate at the bottom of the concrete layer. The composite beam was center-loaded using an 11-kip MTS servo-hydraulic actuator with the stroke position gauge being set at 0.5 mm per minute. An 8800 INSTRON digital controller was used to program the loading commands and LABVIEW was employed to record the vertical load, two LVDT measurements, a clip gauge, and the stroke position.

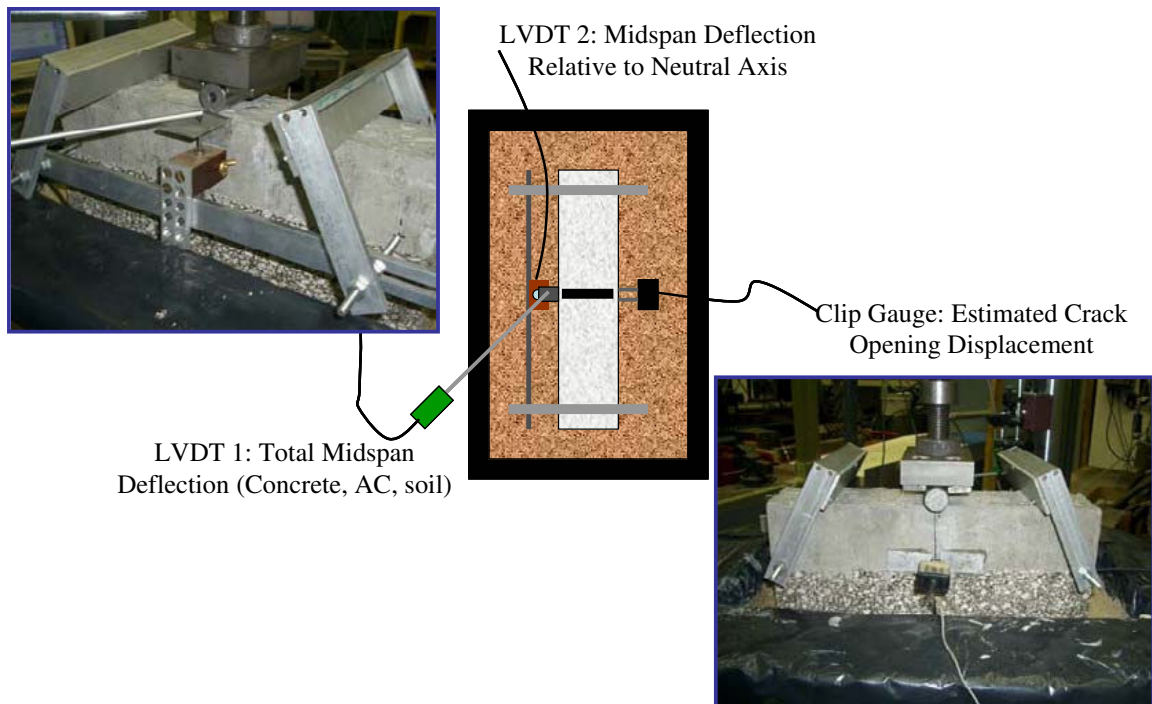


**Figure 29 - Composite beam test setup.**

## ***Composite Beam Results***

### *Load versus Vertical Stroke Curves*

The vertical deflection (stroke) and the crack opening displacements measured for each beam are presented here, shown in Figures 30 and 31. The results from the LVDT measuring the total vertical deflection did not always work properly (particularly with the 4 lb Schanck beams) due to problems with the rigid connection; a comparison between the stroke and LVDT to measure vertical deflection is shown in Figure 32. In general, the vertical deflection from the actuator stroke was expected to have some extraneous deformations and should not be considered the true total deflection.

The composite beams made from the same concrete mixture were tested on separate days and therefore the change in soil characteristics from compaction fluctuated between the two specimens. As seen in Figure 30, the 1<sup>st</sup> beam generated larger vertical deflections as the soil compacted compared to the 2<sup>nd</sup> beam (Figure 31). It appeared that when the soil moisture was lower (cracks occurred in the clay), the difference between the 1<sup>st</sup> and 2<sup>nd</sup> beam tested was lower and the magnitude of the vertical deflection was lower; the Anna, Dan Ryan and Brazil 2 mixtures were tested with the soil in a drier condition.

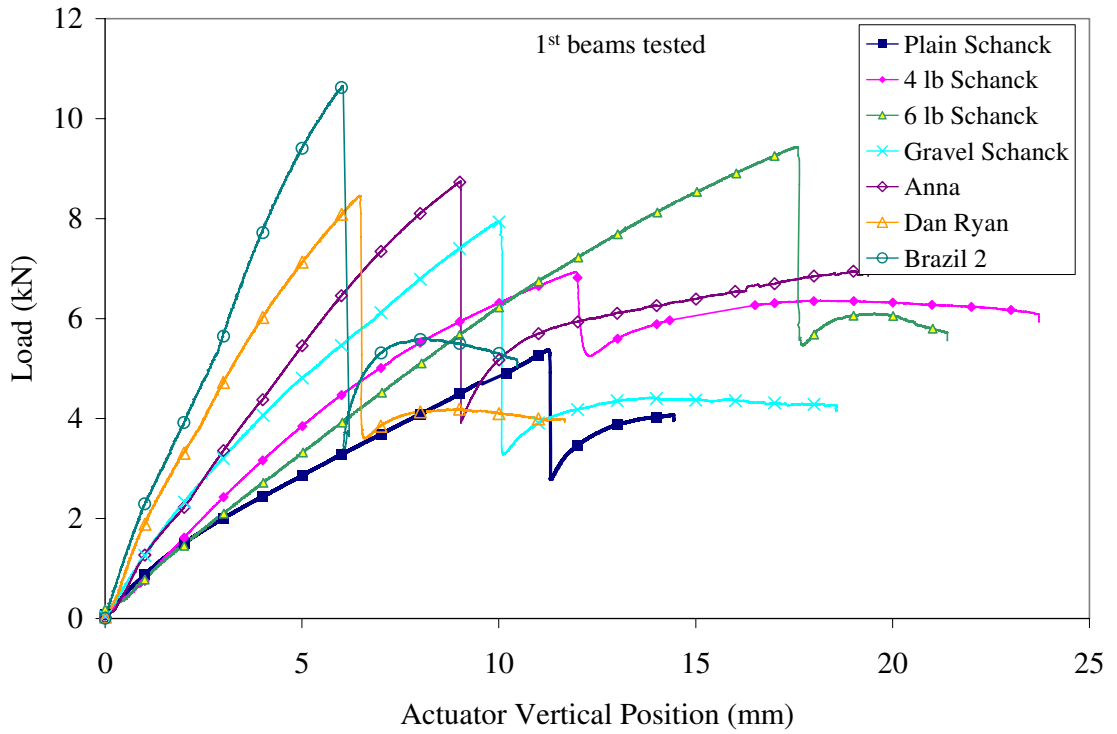


Figure 30 – Vertical deflections (stroke) for 1<sup>st</sup> composite beam specimen.

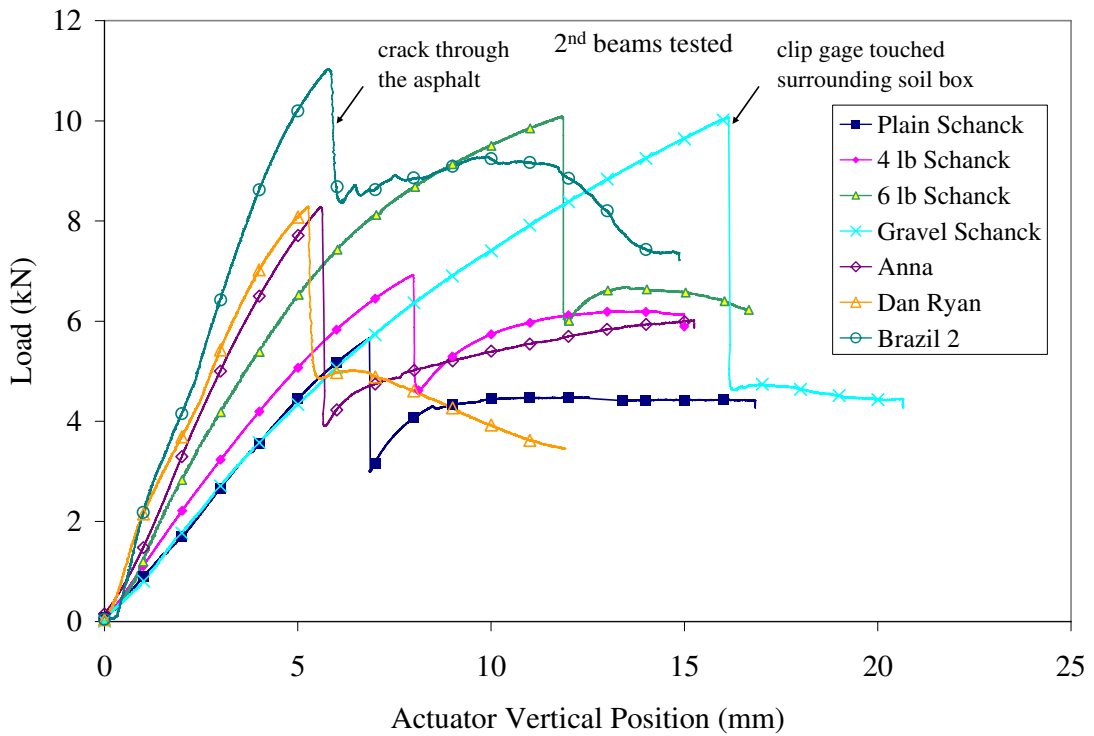
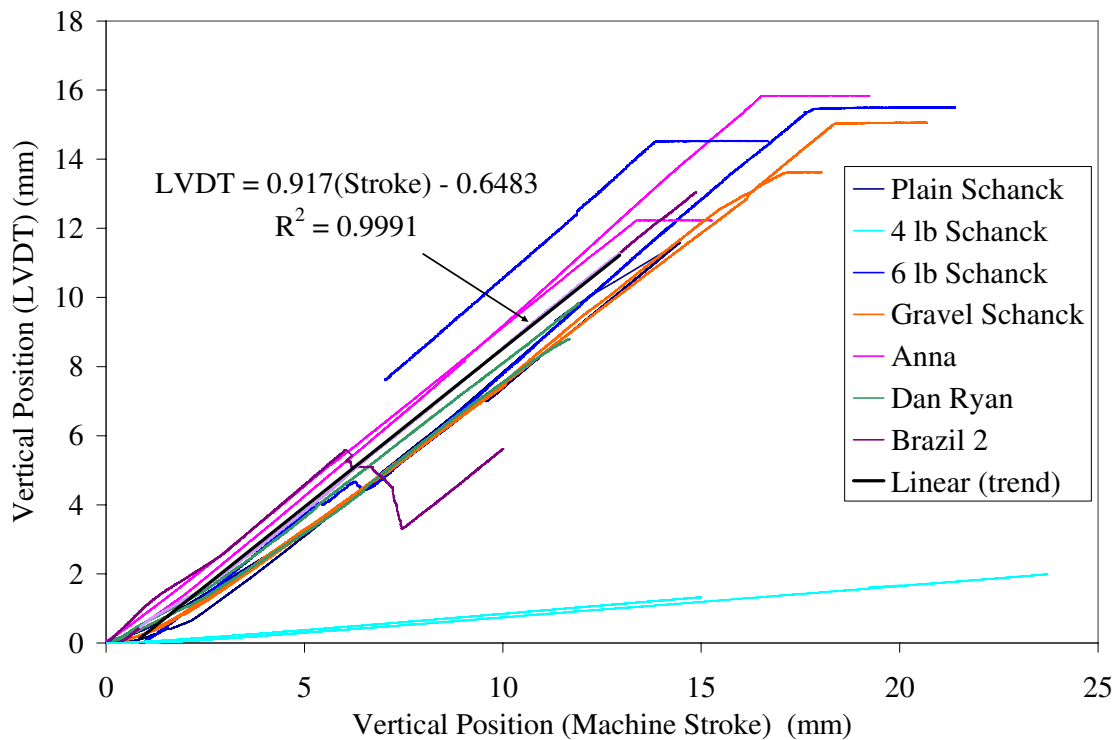


Figure 31 - Vertical deflections (stroke) for 2<sup>nd</sup> composite beam specimen.



**Figure 32 - Vertical position comparison between machine stroke and LVDT values.**

*Load versus COD curves*

The results of the estimated crack opening displacement (COD) were plotted versus load for the Schanck Avenue and all other concrete mixtures in Figures 33 and 34, respectively. The load versus COD curves was similar between the two composite beam specimens tested for each concrete mixture.

The additional LVDT used to measure the midspan deflection with respect to the neutral axis of the concrete and asphalt composite beam has similar results as the clip gauge measuring the crack opening displacement above the notch tip; this comparison plot is shown in Figure 35. The magnitude along the x-axis (the midspan deflection relative to the neutral axis) in the plot was slightly higher than the COD values; however the load

levels are all the same. Only the 4 lb Schanck specimen gauges followed different correlations between the LVDT and the clip gauge.

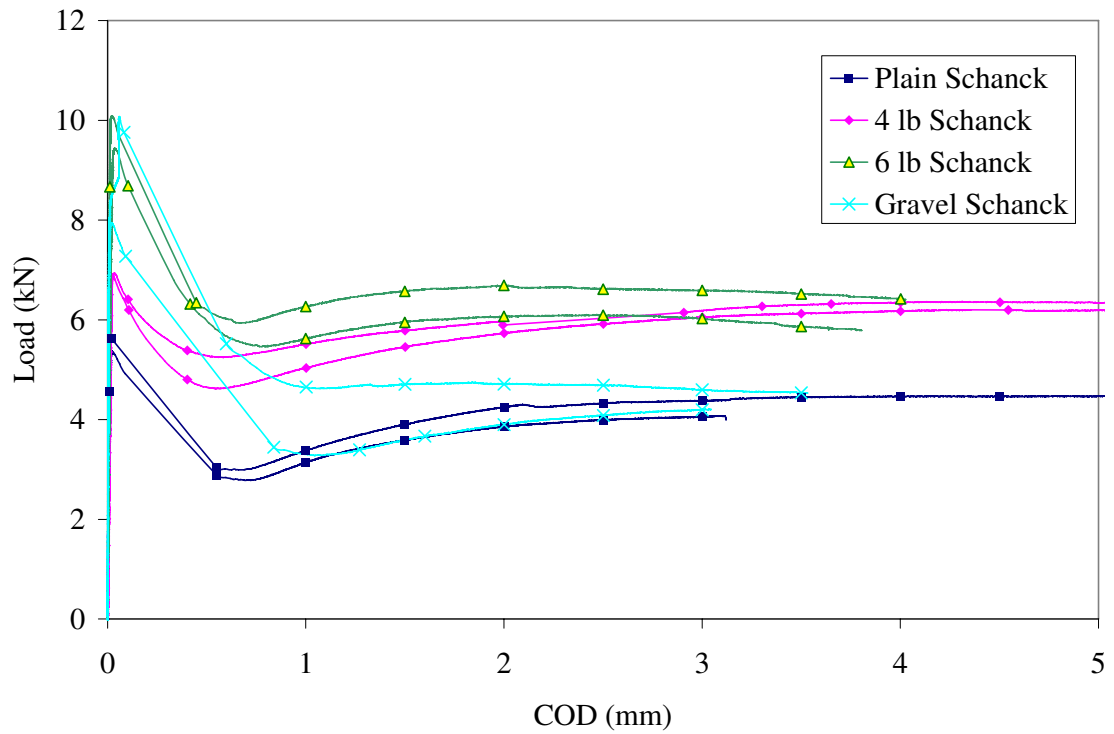


**Figure 33 - Load versus crack opening displacement curves for Schanck Avenue composite beam specimens.**

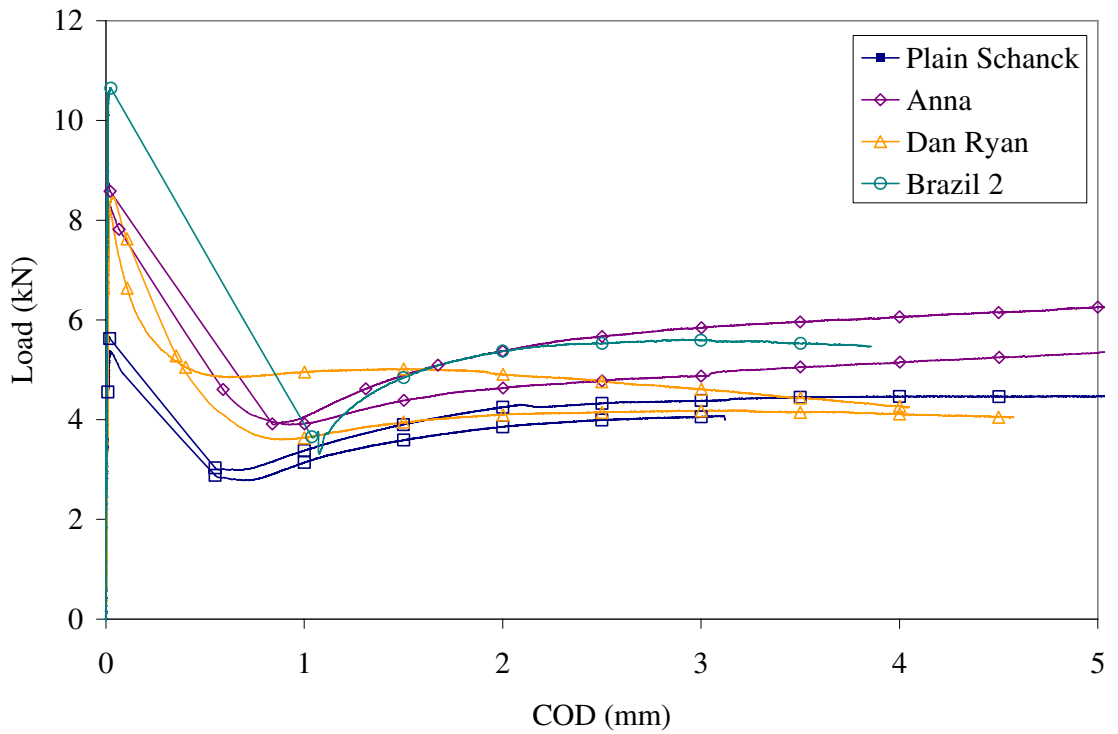


**Figure 34 - Load versus crack opening displacement curves for non-reinforced composite beam specimens.**

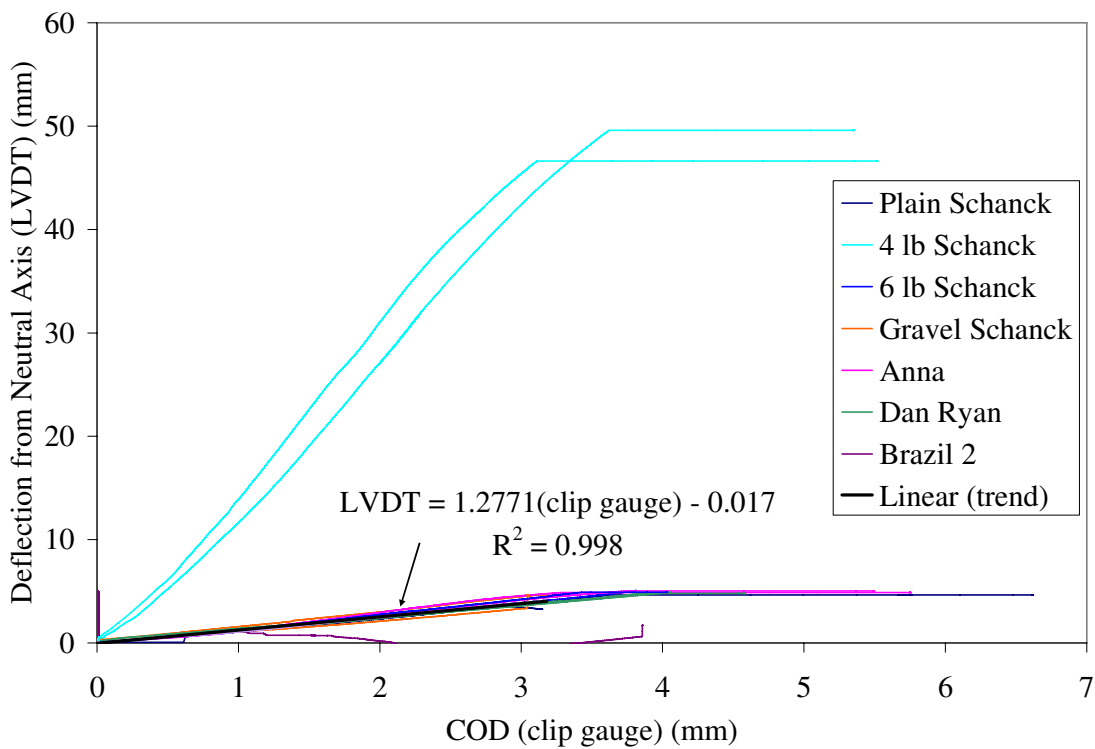


**Figure 35 - COD from clip gauge versus the neutral axis vertical deflection LVDT.**

Recall, the overall objective of the composite beam test was to determine the effect of the concrete mixture on the peak load capacity and residual load capacity after cracking. The first peak load occurred with the sign of a macrocrack through the concrete layer above the asphalt crack. The load dropped off immediately as a plastic hinge was formed. The majority of the post peak load behavior was associated with the soil reaction with very limited beam bending and significant compression of the beam into the soil. For this research, the testing was halted once it was clear that the soil was contributing most of the energy from the test after the concrete had fractured.

#### *Composite Testing Results*

The stroke vertical deflection and COD values at the peak and minimum load (after the drop), and the load drop percentage are shown in Table 14 for all the concrete mixtures. A schematic of the composite beam loading is shown in Figure 36 with key definitions of the load versus deflection curve. The load drop was calculated as follows in equation 11. The Peak/Min Load ratio was found by dividing the peak load by the minimum load immediately after cracking.

$$\% \text{ Load Drop} = \frac{(P_{Peak} - P_{Min})}{P_{Peak}} \quad (11)$$

**Table 14 – Average Composite Beam Specimen Results**

| Mixture        | Age (days) | Peak Load (kN) | Min Load after cracking (kN) | COD (mm) |       | Machine Position (mm) |       | Peak/Min Load Ratio | % Load Drop |
|----------------|------------|----------------|------------------------------|----------|-------|-----------------------|-------|---------------------|-------------|
|                |            |                |                              | @ Peak   | @ Min | @ Peak                | @ Min |                     |             |
| Schanck Plain  | 14         | 5.5            | 2.9                          | 0.020    | 0.68  | 9.1                   | 9.1   | 1.9                 | 48%         |
| Schanck 4 lb   | 14         | 6.9            | 4.9                          | 0.027    | 0.57  | 10.0                  | 10.2  | 1.4                 | 29%         |
| Schanck 6 lb   | 28         | 9.8            | 5.7                          | 0.027    | 0.72  | 14.7                  | 14.8  | 1.7                 | 42%         |
| Schanck Gravel | 28         | 9.0            | 3.9                          | 0.039    | 1.06  | 13.1                  | 13.2  | 2.3                 | 56%         |
| Anna           | 14         | 8.5            | 3.9                          | 0.017    | 0.88  | 7.3                   | 7.4   | 2.2                 | 54%         |
| Dan Ryan       | 28         | 8.4            | 4.2                          | 0.025    | 0.75  | 5.9                   | 6.1   | 2.0                 | 50%         |
| Brazil 2       | 28         | 10.8           | 5.8                          | 0.017    | 0.54  | 5.9                   | 6.1   | 2.3                 | 47%         |

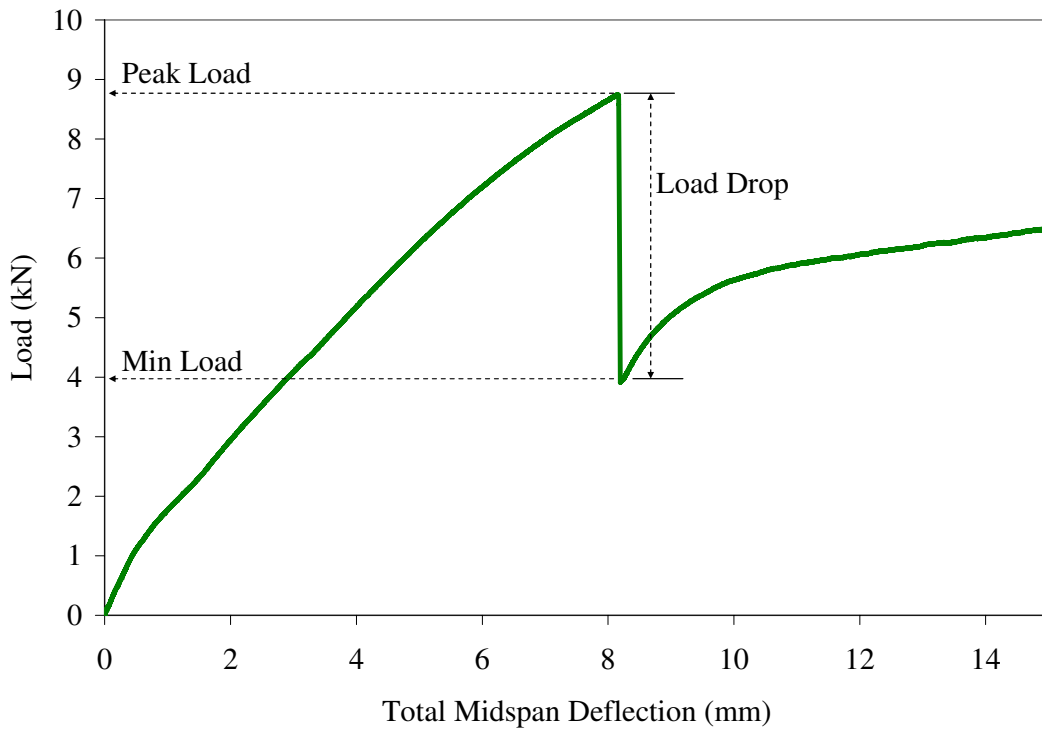


**Figure 36 - Example of composite beam specimen result.**

### *Peak Load*

The peak load for the Brazil 2 mixture was the highest while the smallest peak load, came from the Plain Schanck mixture. These corresponding peak composite loads were reflected in the compressive strength of the concrete. Brazil 2 mixture had the highest compressive strength in contrast the Plain Schanck mixture had the lowest compressive strength due to its high air content. Similarly, the Anna and 6 lb Schanck mixtures showed higher peak loads which match their higher compressive strengths. One thing to note here is the age of testing for these specimens; all of the specimens tested at 28 days showed higher peak loads, while among the 14 day specimens, only the Anna mixture demonstrated a high peak load compared to the other mixtures.

### *Load Drop Percent*

The drop in load was hypothesized as a significant factor to estimate the structural integrity of the UTW once a crack does form. For example, in the field the Anna pavement was one with the most cracking within each slab and with cracking appearing early on in the pavement life [47]. The magnitude of the load drop can be associated with the performance of UTW in the field after some initial cracking has occurred. One research project predicted the load carrying capacity of slabs based on the residual strength of concrete beams [41].

Based on the results here, the Anna mixture does show poor results as far as the having a 54% percentage drop in load capacity after cracking. The Gravel Schanck mixture has the greatest load drop of 56%. This load drop is likely associated to the fact that these

specimens fractured around the aggregates even at 28 days. On the other hand, the FRC mixtures (4 lb Schanck and 6 lb Schanck) have the two lowest load drops at 29% and 42% respectively. Some concrete construction issues with the 6 lb Schanck mixture may have caused the higher load drop than the 4 lb Schanck mixture. Overall the drop in load was not as significant as expected. In addition, the geometry of the test, as previously mentioned, impacted the fracture behavior of the composite beams. This behavior was attributed to the 2-D nature of this test which does not allow the cracking propagation resistance between fibers and plain concrete to be realized.

### ***Composite Beam Testing Issues***

Several issues related to this testing apparatus have occurred. First of all the geometry has been determined to influence the fracture of the beam. Also the soil condition affected the deflection measurements. Overall, the results did show enough information to gain an idea of the fracture performance of the composite section. The actual fracture parameters were determined and shown later in this chapter.

All beams fractured in a curved pattern commonly seen in bending tests of beams subjected to large scale yielding [1]. Figure 37 shows a fractured composite beam after the testing was complete. This large scale yielding was likely the result of such a small fracture area ahead of the notched HMAC specimen and fracture properties would be difficult to determine from these specimens as a result. According to large scale yielding theory, this fracture behavior indicates that the stresses near the crack tip depend on the

geometry [1]. Fracture properties such as the initial fracture energy and  $CTOD_C$  cannot be computed from the test setup without the appropriate geometric correction factors. Future modeling of the results requires the each materials' elastic and visco-elastic properties, the concrete fracture properties, and the global responses from the composite beam test. As discussed early, separate TPB specimens were cast and tested to acquire the fracture properties of the concrete. Soil and HMAC material properties have not been tested at this time.

The concrete appeared to be well bonded to the HMAC beams based on visual observations before, during, and after testing. Failure was defined when the concrete layer was cracked and all LVDTs and the clip gauge were out of range.



**Figure 37 - Picture of fractured composite beam.**

Specific issues which occurred during testing are explained next in order to accurately understand the load-deformation behavior. The 2<sup>nd</sup> beam tested with the Gravel Schanck mixture likely has inaccurate results because the edge of the clip gauge mistakenly was touching the soil box surrounding the beam. The clip gauge likely carried some of the load from the MTS machine to the soil box frame rather than through the composite beam, thus reducing the vertical stroke measurements. In the 2<sup>nd</sup> beam from the Brazil 2 mixture, the concrete crack originated through an alternative crack or weak zone in the HMAC beam (see Figure 38) rather than the original pre-existing crack in the HMAC beam.



**Figure 38 – Failure pattern in the second Brazil 2 composite beam specimen.**

#### *HMAC Surface Condition*

Field studies on the bond preparation for UTW have so far been inconclusive as to what construction technique should be used before placing down concrete on asphalt. The consensus of the UTW literature recommends at least a clean surface; ideally milling and

cleaning would provide the optimal bonding condition. Two surface conditions of the HMAC beam, clean saw-cut surface and weathered existing top surface, were incorporated into the testing. A photo of the HMAC before saw-cutting can be seen in Figure 39. The composite beams with different surface preparations did not separate during the test and no correlation was seen in the load versus vertical deflection curves to distinguish between the different surface types. The difference between surface conditions in the asphalt was not noticeable in the load versus COD results either. Therefore the optimal surface condition of the asphalt could not be determined from this testing configuration.



**Figure 39 - Photo of an upside-down HMAC section prior to saw-cutting into beam sizes.**

### *Soil Consolidation*

After each consecutive test, the soil for the composite beam test became more consolidated and even showed depressions for locations in which the beam had rotated into the soil. Although the sand layer on top of the clay was consistently leveled off, the clay underlying became quite deformed after each consecutive test. This may have

contributed to the variation in load versus displacement curves between specimens and this should be considered for future composite beam testing.

## ***Material Properties of Composite Beam Mixtures***

### *Fracture Results*

The fracture properties (described in Chapter 2) of all the composite beam mixtures were also measured to enable future modeling of the results and to compare their behavior under different geometry and boundary conditions. The load versus CMOD curves for each TPB sample tested is shown in Figures 40 and 41 and their respective fracture properties are shown in Table 15.

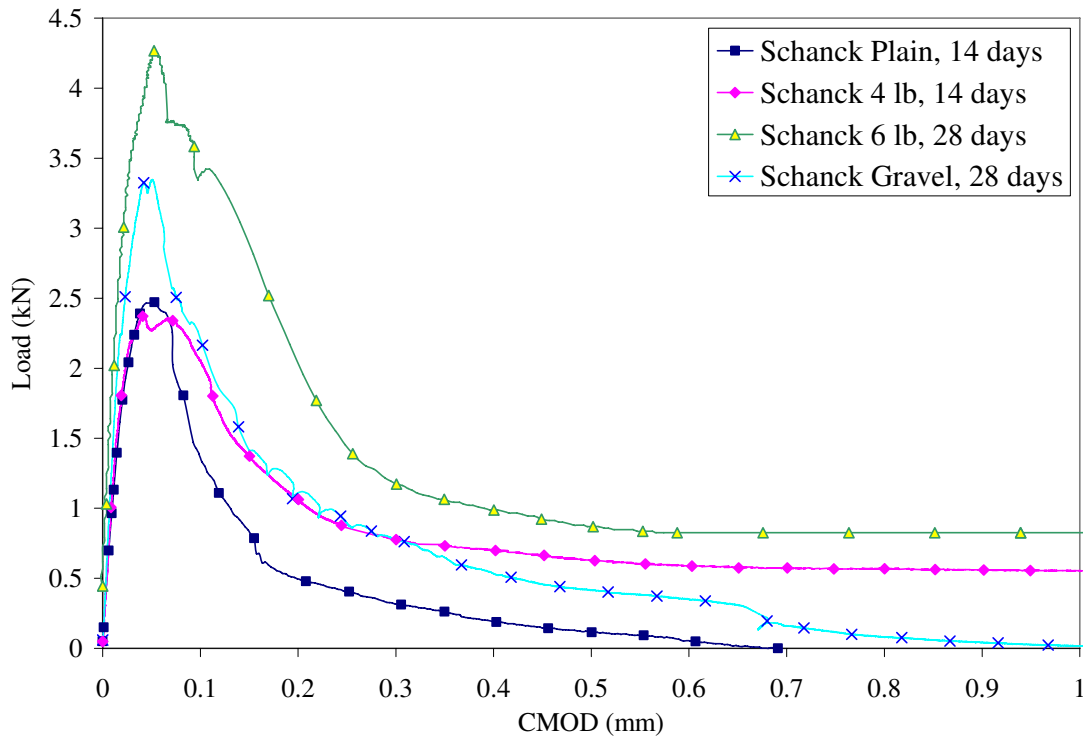


**Figure 40 - TPB Specimen load versus CMOD curves for Schanck concrete mixtures.**

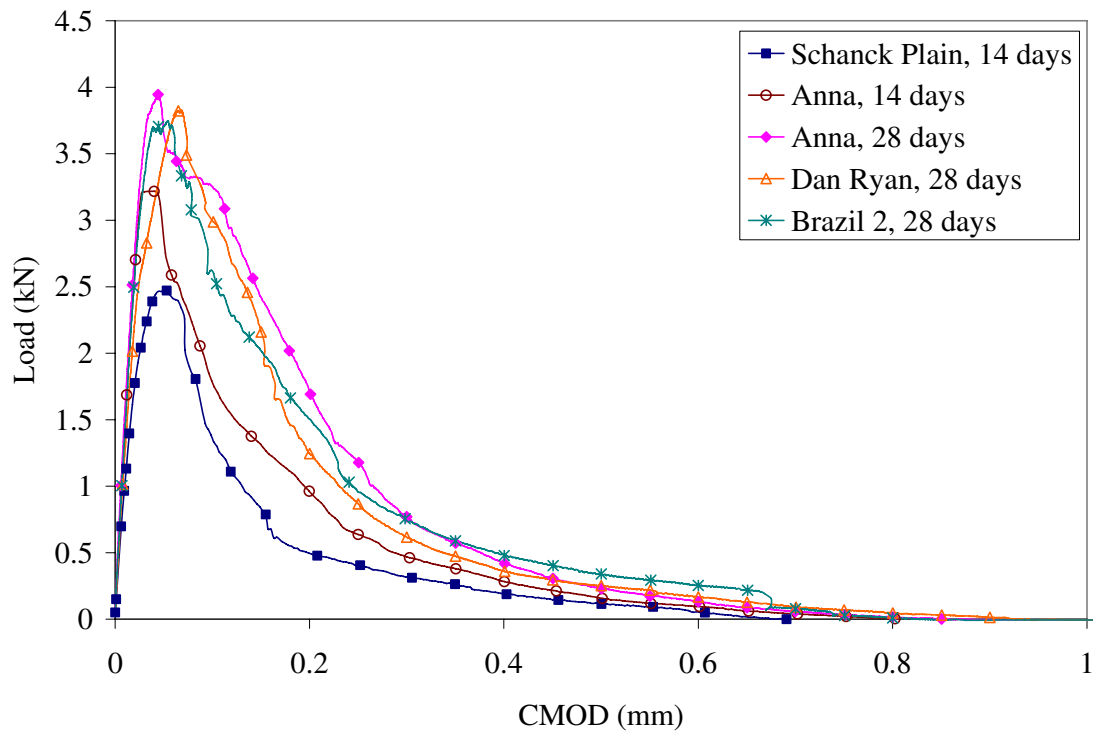


**Figure 41 - TPB Specimen load versus CMOD curves for non-reinforced concrete mixtures.**

**Table 15 - Fracture Results of UTW Mixtures**

| Mixture        | Age (days) | Peak Load (kN) | Calculated Elastic Modulus (GPa) | $K_{IC}$ (Mpa $m^{1/2}$ ) | $CTOD_C$ (mm) | $G_f$ (N/m) | $G_F$ (N/m) |       |
|----------------|------------|----------------|----------------------------------|---------------------------|---------------|-------------|-------------|-------|
| Schanck Avenue | Plain      | 14             | 2.36                             | 17.1                      | 0.86          | 0.031       | 43.7        | 60    |
|                | 4 lb       | 14             | 2.35                             | 20.5                      | 0.82          | 0.025       | 33.8        | 1,720 |
|                | 6 lb       | 28             | 4.34                             | 27.4                      | 1.33          | 0.024       | 65.2        | 3,550 |
|                | Gravel     | 28             | 3.23                             | 30.7                      | 1.10          | 0.018       | 39.2        | 112   |
| Anna           | 14         | 3.74           | 26.3                             | 1.02                      | 0.015         | 41.2        | 99          |       |
|                | 28         | 3.69           | 27.6                             | 1.05                      | 0.016         | 40.0        | 115         |       |
| Dan Ryan       | 28         | 3.67           | 27.8                             | 1.24                      | 0.019         | 55.7        | 133         |       |
| Brazil 2       | 28         | 3.52           | 29.7                             | 1.15                      | 0.018         | 44.3        | 102         |       |

### *Fracture Properties*

The fracture properties were determined for each mixture at their corresponding age as the composite beam test. The higher cement content (Anna and the Brazil 2) mixtures had higher compressive strengths (see Table 13) and higher peak loads as seen in Table 15; this matches the predicted correlation described in Figure 12 from Chapter 3. For the TPB tests performed at 28 days (with the exception of the Gravel Schanck mixture) the peak loads ranged from about 3.5 to 4.3 kN, much higher than the 14-day specimens at 2.4 to 3.7 kN range, and had similar initial fracture properties. The Gravel Schanck mixture has the highest elastic modulus, which reduced its initial fracture energy. The Anna mixture demonstrated the lowest initial fracture energies at 14 and 28 days. The Dan Ryan mixture had one of the highest initial and total fracture energies at 28 days.

### *FRC Results*

The 6 lb Schanck mixture had the greatest peak and post-peak behavior when tested at 28 days as seen in Figures 40 and 42. As seen in Table 15, the initial fracture energy and the stress intensity factor for the 6 lb Schanck mixture are slightly higher than the Plain Schanck due to the later age of testing and the increased compressive and tensile strengths. The 4 lb Schanck mixture had roughly the same peak load as the Schanck Plain mixture at 14 days; however the post-peak load is considerably higher even out to large CMOD values as shown in Figure 42. The total fracture energies for the 4 lb and 6 lb Schanck mixtures were 1,720 N/m and 3,550 N/m, respectively, and both are considerably greater than the Plain Schanck total fracture energy at 60 N/m.

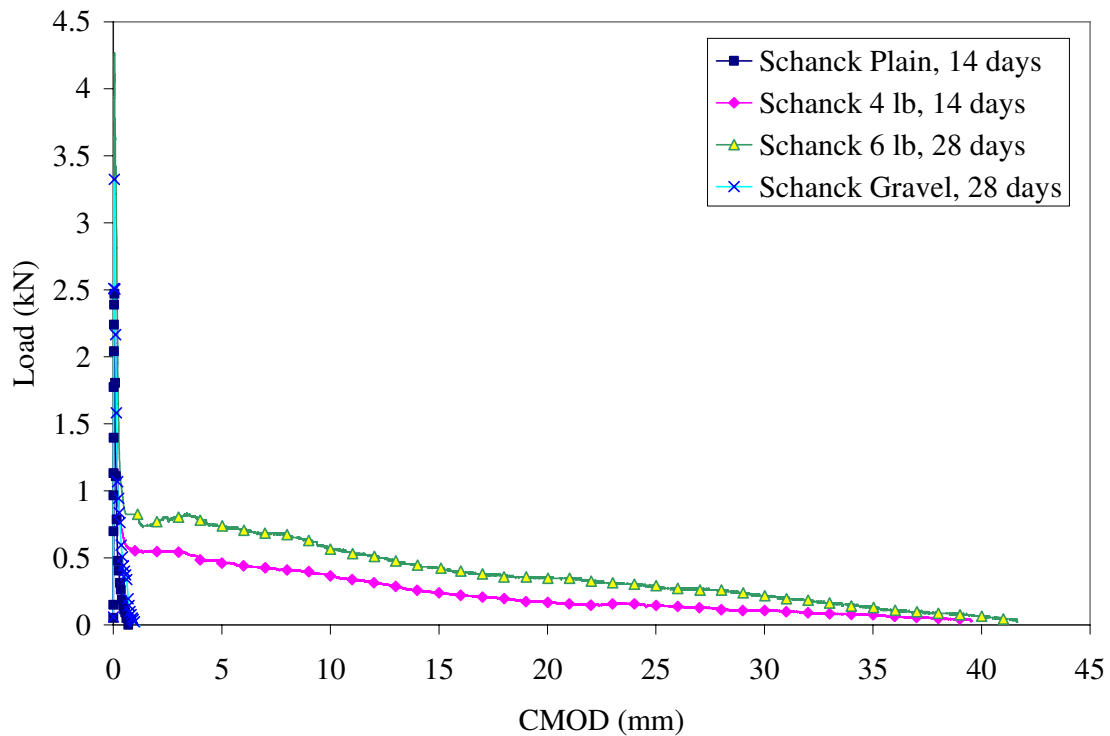


**Figure 42 – TPB Specimen load versus CMOD curves for run-out tests for Schanck mixtures.**

### ***Concrete Free Shrinkage***

In UTW designs, excessive concrete shrinkage could result in de-bonding between the concrete and existing HMAC layer. Higher strength mixtures were typically more susceptible to this behavior due to their higher total cementitious content. In order to assess the potential for excessive shrinkage, specimens were cast with dimensions of 3x3x11.25 inches according to ASTM C157-99 [2]. Shrinkage specimens were demolded 24 hours after casting, and then stored in a controlled climate room at 50% RH and 23 °C. Shrinkage and mass loss was measured at 1, 2, 3, 7, 14, 28 and approximately 56 and 90 days after casting for several composite beam mixtures. Only the Plain Schanck, 4 lb Schanck, and Anna mixtures were studied for their shrinkage with time.

Shrinkage and mass loss results for these same mixtures are shown in Figures 43 and 44. The mass loss of the Plain Schanck specimens was not measured at 24 hours after casting. Since this data point was used to describe the magnitude of shrinkage, the mass loss curve was manually extrapolated so that the entire mass loss curve was similar the 4 lb Schanck mixture. As seen in Figure 43, the addition of fibers in the 4 lb Schanck mixture compared to the Plain Schanck mixture led to a lower free shrinkage in the concrete. Other testing done to measure shrinkage of concrete has determined that the shrinkage was reduced by about 0.02% at 28 days with the addition of 0.5% volume fraction of polypropylene or steel fibers [27]. The use of higher cement content in the Anna mixture showed a greater shrinkage after approximately 14 days and a lower mass loss after 2 days. Since the Anna mixture has a lower water cement ratio of 0.36, some of the shrinkage seen here was likely due to autogenous shrinkage [35]; also a smaller amount of free water was lost to evaporation, therefore making the mass of the specimen roughly the same with time.

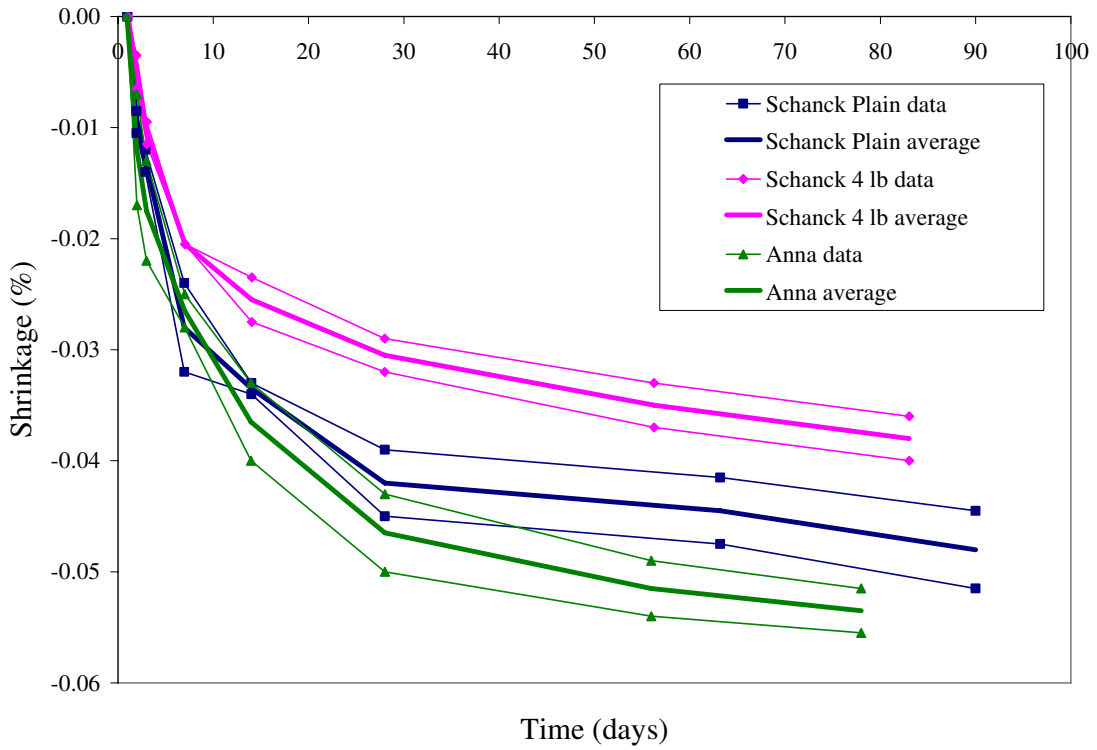


**Figure 43 – Concrete free shrinkage results for the UTW mixtures.**

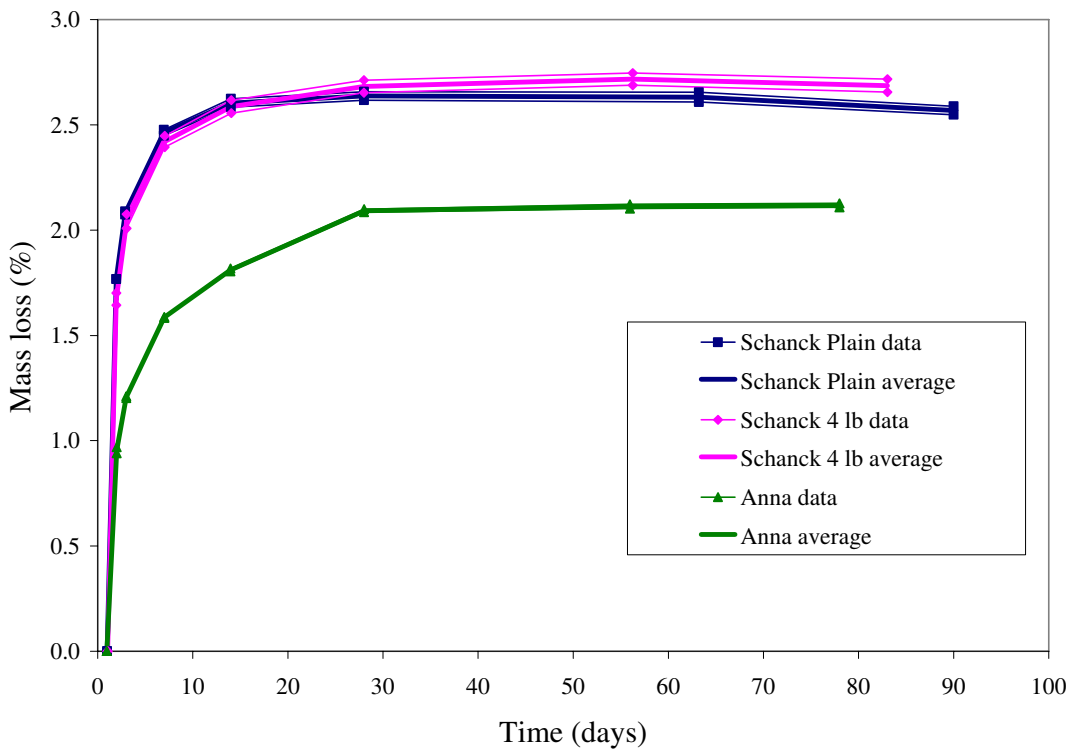


**Figure 44 - Mass loss results for the UTW mixtures.**

## *Summary*

The composite beam test results and TPB fracture properties have similar peak load trends when comparing between mixtures. The greatest peak loads were seen in the Brazil 2, 6 lb Schanck, and Gravel Schanck specimens for the composite test; the greatest peak loads in the fracture test were with the 6 lb Schanck and 14-day Anna test samples. The load drop was lowest with the FRC mixtures which indicated its usefulness in providing residual load capacity especially for UTW systems. There is a rough correlation between the peak/min load ratio and the fracture parameters when comparing plain and fiber-reinforced concrete. No trend was found between the load drop and the total fracture energy between the plain concrete mixtures.

## **CHAPTER 6: FIBER-REINFORCED CONCRETE (FRC) MATERIALS FOR RIGID PAVEMENTS**

A variety of fiber types and geometries exist for use in FRC for rigid pavements. Currently modulus of rupture (MOR) is determined in a laboratory to describe the effectiveness of each fiber type for use in pavement designs. In this thesis chapter, a collection of flexural strength test results for a variety of fiber types and volume fractions was compared. Different standard test methods have been developed over they years to incorporate the post-peak performance of FRC in flexural strength. These methods are also compared for each test result in this chapter.

### *FRC Performance*

Two important issues concerning the use of fiber-reinforcement in concrete pavements are what types of fibers should be used and what volume fraction of a particular fiber type should be add to the plain concrete mixture. The objective of this chapter is to demonstrate the variability in FRC laboratory testing performance for different fiber types and volume fractions. Each fiber type inherently has a different performance that must be considered in designing and specifying FRC.

FRC has been the topic in many research projects and utilized to construct many field concrete pavements across the country. The key features to using a FRC mixture are the increased toughness of the composite and reduced crack widths which can be beneficial for improving pavement performance. The addition of structural fibers in concrete has been shown to improve slab load carrying capacity [41]. A further benefit of the smaller

crack widths seen in FRC pavements could be improved load transfer efficiency at joints or cracks over time.

The influence of each type of fiber on the surrounding concrete would be useful to quantify. Several books and numerous journal papers have been published which analyze and characterize the micromechanical behavior of fibers in plain concrete [3, 11, and 18]. Several of the available theories to predict the composite stress-displacement relationships in a cracked FRC are explained in greater detail in Appendix A.

#### *Flexural Strength Tests*

The standard modulus of rupture (MOR) test configuration (ASTM C78 [2]) for four-point bending flexure is still one of the most common field testing and this testing configuration was primarily be used to assess the toughness performance of various types of fibers and volume fractions of fibers for this chapter. Figure 45 is a photo of the flexure test as it was performed for this study.

A previous standard method, ASTM C 1018, described the MOR and the post-peak performance of a fiber-reinforced concrete beam as deflection ratios and indices; this method involves more complex calculations and the link between the empirically chosen deflection-based indices and field slab performance has been lacking. The Japan Concrete Institute [22] developed JCI-SF4 to calculate the post-peak curve of FRC based on the area under the flexural curve for larger deflections. Following this standard, the ASTM C 1609 method was developed and incorporated the load-deflection curve area up

to similar large vertical deflections. The JCI-SF4 and ASTM C 1609 standards are easier to calculate and to comprehend and some research indicates improved correlation with field performance for different FRC mixtures. The different standard flexural strength methods will be described and compared later in the chapter. One of the important issues for comparing the methods was to determine whether the ASTM C 1609 does an adequate job to characterize FRC behavior for different fiber types and volume fractions.

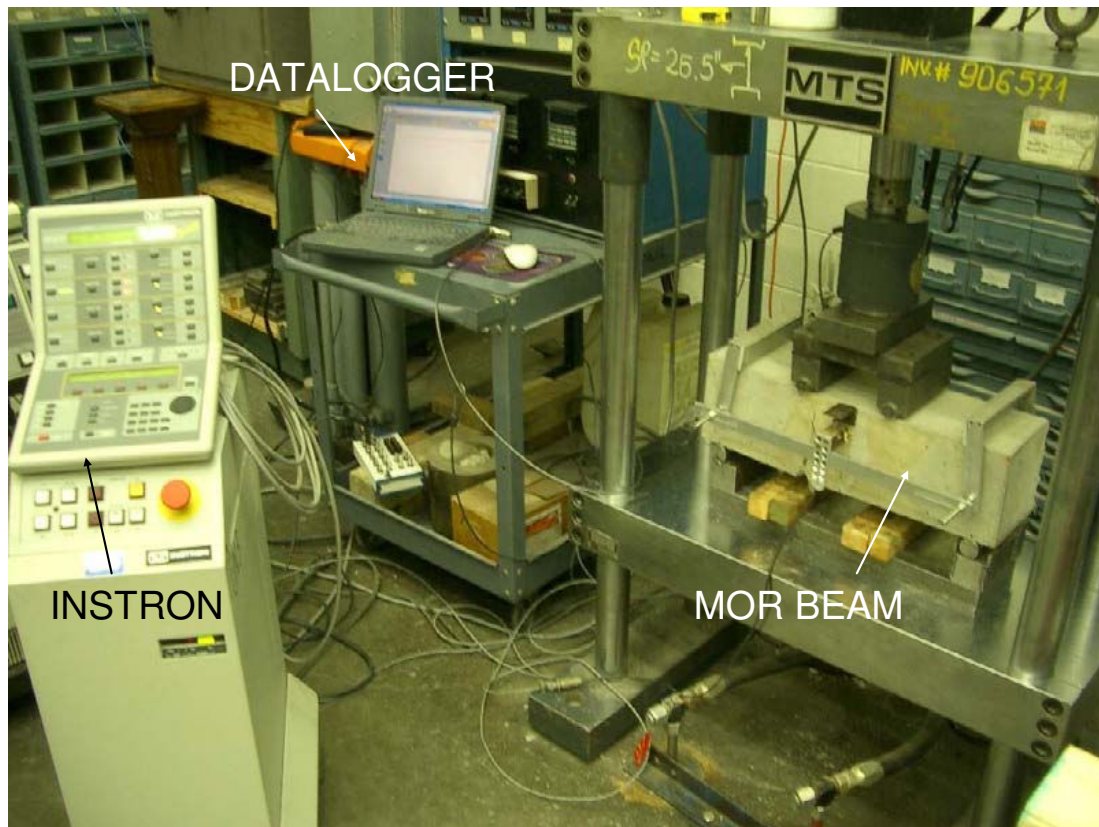


**Figure 45 - Photo of the equipment and set-up for the 4-point bending MOR test.**

The different types of fibers investigated for this study are shown in Table 16. The geometry and material properties are listed according to their manufacturers. The actual manufacturer and brand name for these types of fibers have been omitted.

**Table 16 - Fiber Properties**

| Fiber Type                  | Straight Synthetic             | Crimped Synthetic               | Twisted Synthetic           | Crimped Steel 1 | Crimped Steel 2                    | Hooked Steel 1                     | Hooked Steel 2                     |
|-----------------------------|--------------------------------|---------------------------------|-----------------------------|-----------------|------------------------------------|------------------------------------|------------------------------------|
| Material                    | Polypropylene/<br>Polyethylene | Polypropylene<br>/ Polyethylene | Copolymer/<br>Polypropylene | Steel           | Low Carbon<br>Steel, Cold<br>Drawn | Low Carbon<br>Steel, Cold<br>Drawn | Low Carbon<br>Steel, Cold<br>Drawn |
| Cross Section               | Rectangular                    | Rectangular                     | Rectangular                 | Circular        | Semi-circular                      | Circular                           | Circular                           |
| Length (mm)                 | 40                             | 50                              | 54                          | 50              | 38                                 | 60                                 | 50                                 |
| Thickness (mm)              | 0.105                          | -                               | N/A                         | N/A             | -                                  | -                                  | -                                  |
| Width (mm)                  | 1.4                            | -                               | N/A                         | -               | -                                  | -                                  | -                                  |
| Diameter (mm)               | -                              | 0.83                            | N/A                         | 1.3             | 0.4                                | 0.9                                | 1.05                               |
| Wavelength (mm)             | -                              | N/A                             | -                           | 8               | N/A                                | -                                  | -                                  |
| Amplitude (mm)              | -                              | N/A                             | -                           | 0.65            | N/A                                | -                                  | -                                  |
| Aspect Ratio                | 90                             | N/A                             | N/A                         | 50              | 38                                 | 67                                 | 48                                 |
| Specific Gravity            | 0.92                           | 0.91                            | 0.91                        | 7.83            | 7.83                               | 7.83                               | 7.83                               |
| Tensile Capacity (MPa)      | 620                            | N/A                             | 620-758                     | 900             | 828                                | 1000                               | 1000                               |
| Modulus of Elasticity (GPa) | 9.5                            | N/A                             | N/A                         | N/A             | N/A                                | N/A                                | N/A                                |

N/A = not available

## ***FRC Beam Flexural Strength Results***

A collection of FRC beam data from various sources have been combined for this research. The concrete mixture proportions for each FRC mixture study are shown in Table 17. It should be recognized that only the fiber type and volume fractions were used in this chapter and variations in age tested or mixture proportioning was not investigated. The results of the beam testing for different fiber type are broken up below in sections to describe the background on the source of the data and their respective load-deflection curves for straight synthetic fibers, all synthetic fibers, crimped steel fibers, and hooked end steel fibers.

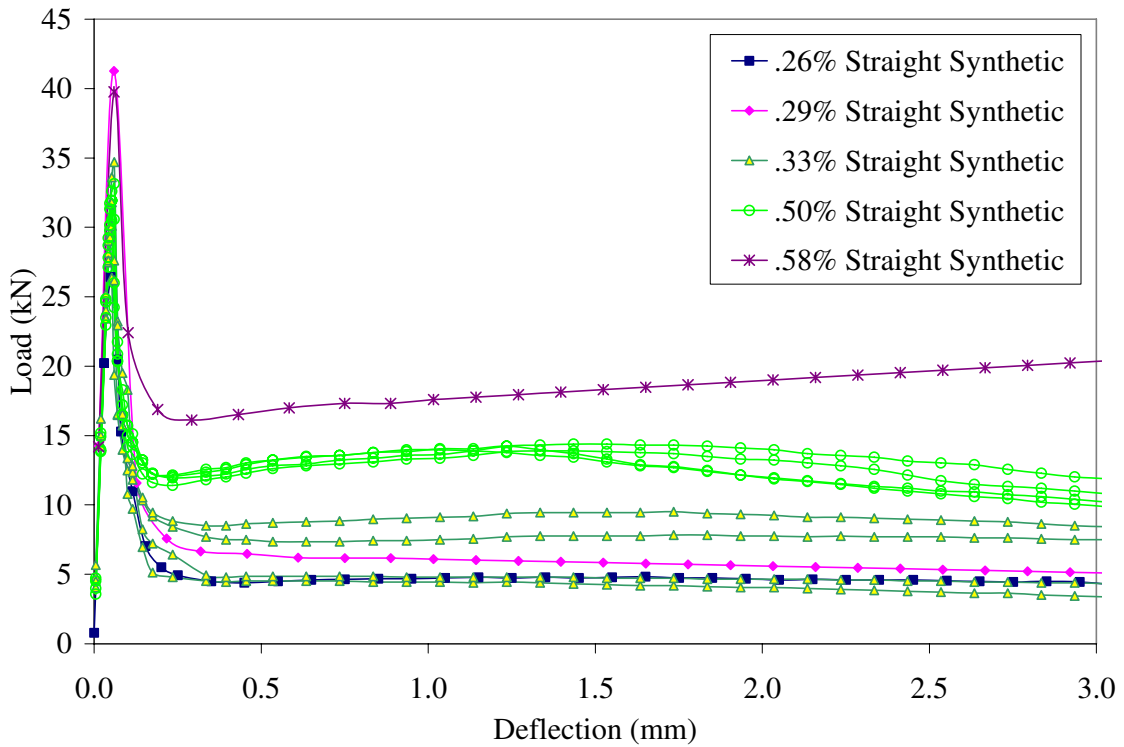
**Table 17 - Concrete Proportions for FRC Study (in lb/yd<sup>3</sup>)**

|                  | Lange and Lee (2005) | Rieder (2002), FGCM (Table 9), Mate (2007) | Donovan and Strickler (2007) | Schanck Ave (Table 1) |
|------------------|----------------------|--|------------------------------|-----------------------|
| Water            | 360                  | 308  | 254                          | 267                   |
| Cement           | 667                  | 607  | 605                          | 515                   |
| Class C Fly Ash  | 0                    | 0  | 0                            | 140                   |
| Coarse Aggregate | 1814                 | 1645                                       | 1834                         | 1972                  |
| Fine Aggregate   | 1008                 | 1360                                       | 1318                         | 1001                  |

### ***Straight Synthetic FRC***

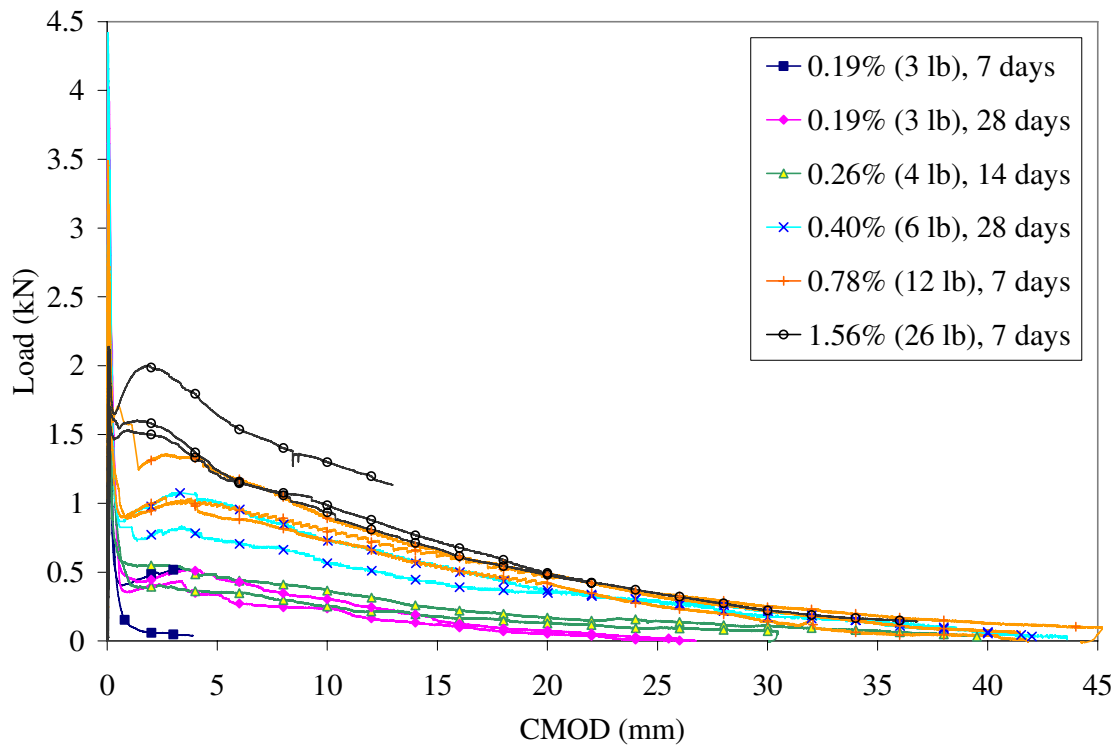
A straight synthetic fiber type has been mixed with concrete in volume fractions from 0.26% to 0.58% for several of the mixtures listed in Table 17. The flexural load versus deflection curves for the straight synthetic FRC specimens can be seen in Figure 46. The 4 lb/yd<sup>3</sup> Schanck Avenue FRC mixture described in Chapters 3 and 5 used 0.26% volume fraction of the straight synthetic fibers. The 0.29% and 0.58% beam specimen results

came from a project completed by Lange and Lee [25] to compare the ASTM C1018 indices of various fiber types and volumes. The 0.33% and 0.50% FRC specimen results (4 beams tested of each volume fraction) were provided by Rieder (2002) based on laboratory testing done to link FRC beam and slab results [41].



**Figure 46 – Straight synthetic FRC 4-point bending flexure curves.**

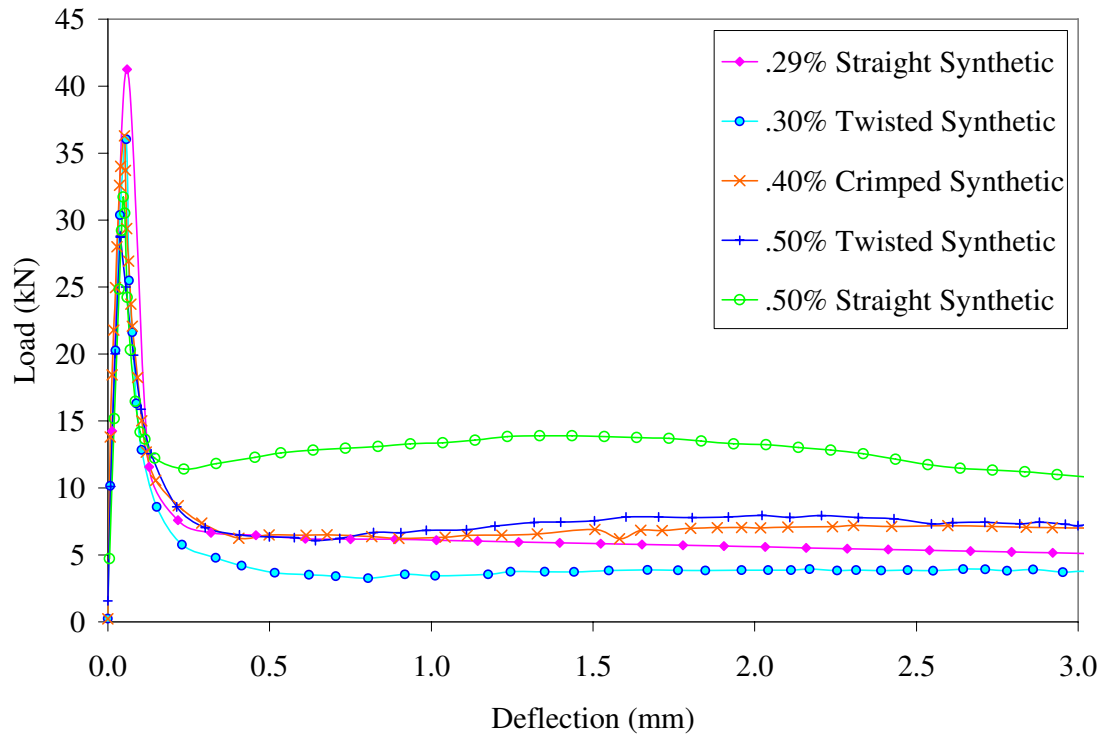
An increase in volume fraction of the straight synthetic fibers in FRC led to an increase in the residual load capacity seen in Figure 46. The TPB specimen load versus CMOD curves for several of these straight synthetic FRC volume fractions are shown in Figure 47. Some of the fracture curves seen here came from the mixtures in Chapters 4 and 5.



**Figure 47 – TPB specimen load versus CMOD curves for straight synthetic FRC mixtures.**

### *Synthetic FRC*

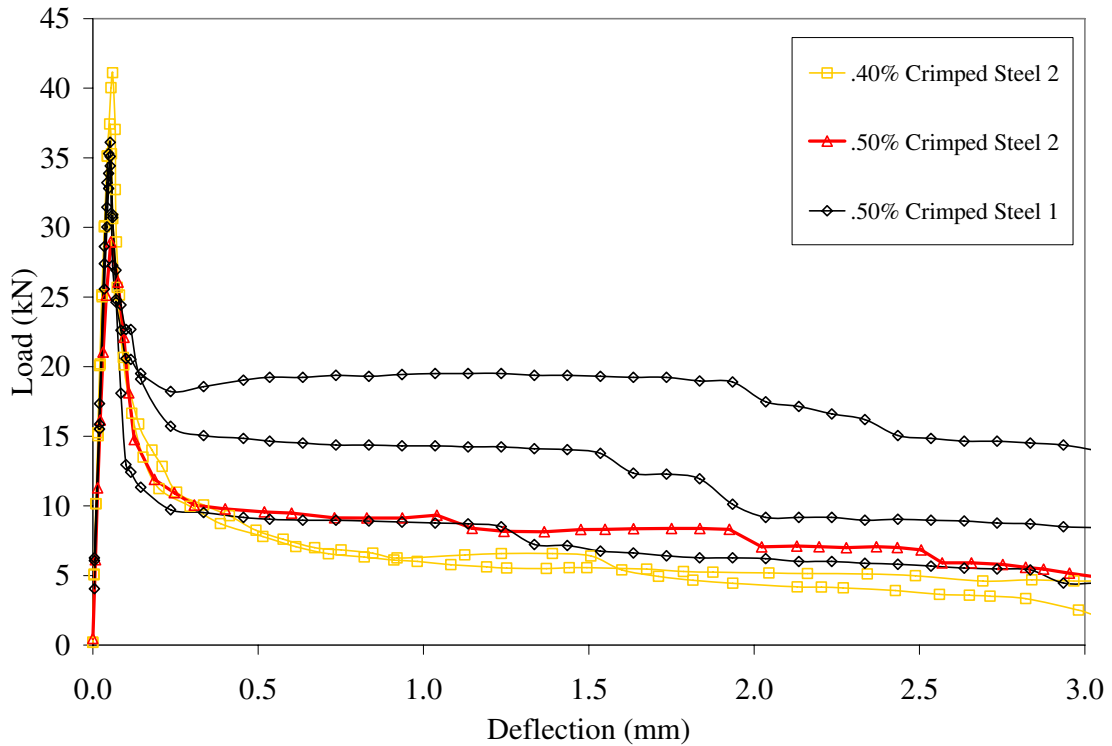
Other forms of synthetic fibers exist, such as the crimped and twisted synthetic fibers. The flexural load versus deflection curves are shown in Figure 48. Donovan and Strickler [15] provided only one beam test data for the crimped synthetic fiber type shown here at 0.40% volume fraction. The data for two twisted synthetic FRC specimens at a different volume fraction (0.3% and 0.5%) were provided by Mate (2007).



**Figure 48 - Synthetic FRC 4-point bending flexure curves.**

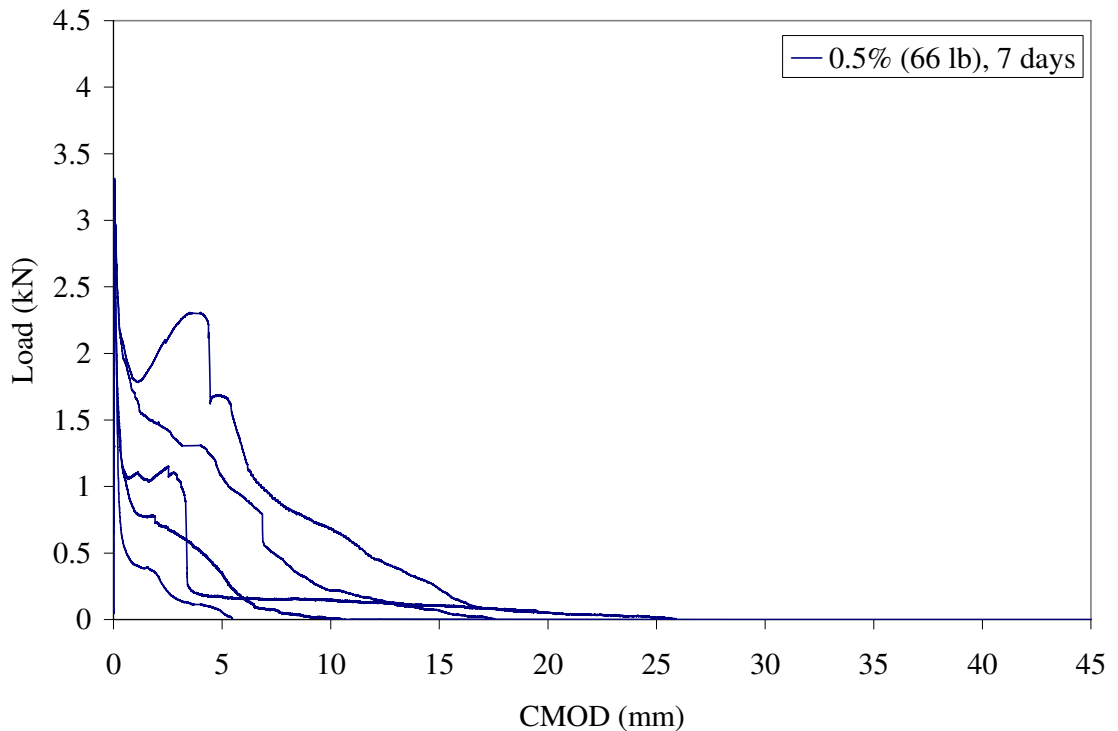
#### *Crimped Steel FRC*

Figure 49 shows the flexural load versus displacement curves for both types of crimped steel fibers in concrete. Three specimens for 0.50% crimped steel 1 fiber volume fraction FRC specimens was provided by Rieder (2002). Two specimens with 0.40% crimped steel 2 fiber (see Table 16 for fiber properties) volume fraction FRC specimens were provided by Donovan and Strickler [15]. One specimen was cast with 0.50% crimped steel 2 fiber for this study using the same mixture design as used in the FGCM study (see Chapter 4).



**Figure 49 - Crimped steel FRC 4-point bending flexure curves.**

TPB fracture testing was also performed using the 0.50% Crimped Steel 2 fibers in concrete. The full load versus CMOD curves for these samples shown in Figure 50 are highly variable. The load levels seemed to drop drastically when a fiber ruptures or pulls out. One sample increased in load capacity after cracking possibly due to the crimped fibers being straightened during testing. At higher volume fractions, the crimped steel fibers in concrete exhibited a more continuous and smooth flexural load versus deformation; for volume fractions less than 0.5% the crimped steel fibers tested here demonstrate high variability due to the small number of fibers bridging the cracked face compared to the total cross-section and due to the early age of testing.



**Figure 50 – SEN(B) load versus CMOD curves for 0.5% volume fraction of crimped steel 2 fibers at 7-days.**

The TPB beams had a smaller fracture area than the MOR beams. With the low volume fraction of steel fibers, this resulted in a lower number of fibers bridging the cracked surface in the FRC and thus a larger variation in the load-displacement curve. The actual number of fibers bridging the cracked face was not recorded, however it was noticed that there was in fact a lower number of steel fibers even on the MOR beam.

#### *Hooked End Steel FRC*

Lange and Lee [25] examined volume fractions of 0.19% and 0.38% of the hooked end 1 steel FRC and volume fractions of 0.30% and 0.55% of the hooked end 2 steel FRC. The average load versus deflection curve for the Lange and Lee specimens are shown in

Figure 51. An additional volume fraction of 0.35% was tested with three hooked end 1 steel FRC samples and provided by Rieder (2002).

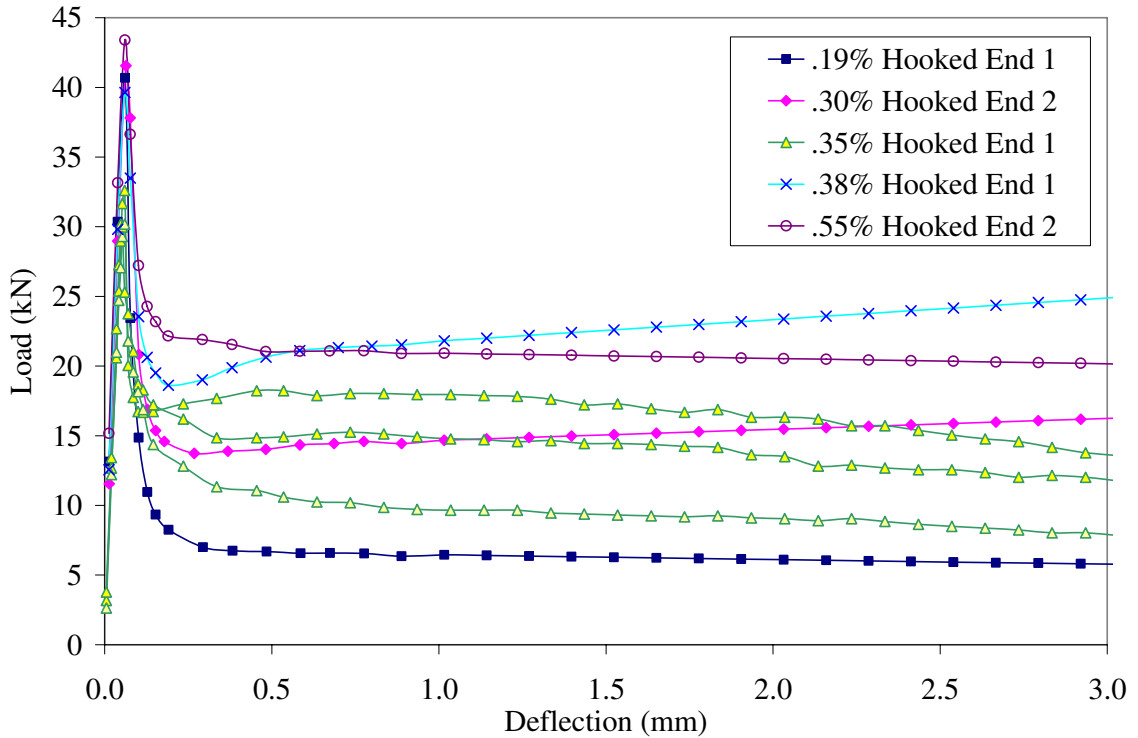


**Figure 51 - Hooked end FRC 4-point bending flexure curves.**

Two similar hooked end fibers were being compared here with the main difference being their aspect ratio. The hooked end 1 fiber had an aspect ratio of 60, while the hooked end 2 fiber had an aspect ratio of 48. The FRC specimens containing the lower aspect ratio hooked end fibers showed greater residual loads after cracking for similar volume fractions. The higher aspect ratio hooked end fibers for the volume fractions shown here up to 0.55% either decreased slightly or maintained a constant load level for at least 3 mm of midspan deflection. In other words, for these small volume fractions the hooked end fibers produced a relatively constant residual strength for deflections up to 3 mm.

## ***Residual Strength Analyses***

For each FRC specimen, the load versus midspan deflection was measured from a four-point bending beam according to ASTM C 78, ASTM C 1018, ASTM C 1609, and JCI standards [2 and 22]. Each standard describes a different analysis technique for analyzing the post-peak load (or residual load) versus deflection data. These techniques are described in detail below and the resulting post-peak properties for each FRC specimen are computed.

### *ASTM C 1018*

A standard for analyzing the residual flexural behavior of fiber-reinforced concrete was originally developed as ASTM C1018 [2] and consisted of computing the first crack flexural strength or MOR, indices, and index ratios at various deflection values. The load at first cracking  $P_A$  is used to compute the modulus of rupture, or flexural strength of the concrete as shown in equation 12,

$$MOR = \frac{P_A S}{bd^2} \quad (12)$$

where  $S$  is the span of the beam,  $b$  is the width of the beam, and  $d$  is the depth of the beam. A schematic of the load versus deflection curve of the flexural beam test is shown in Figure 52.

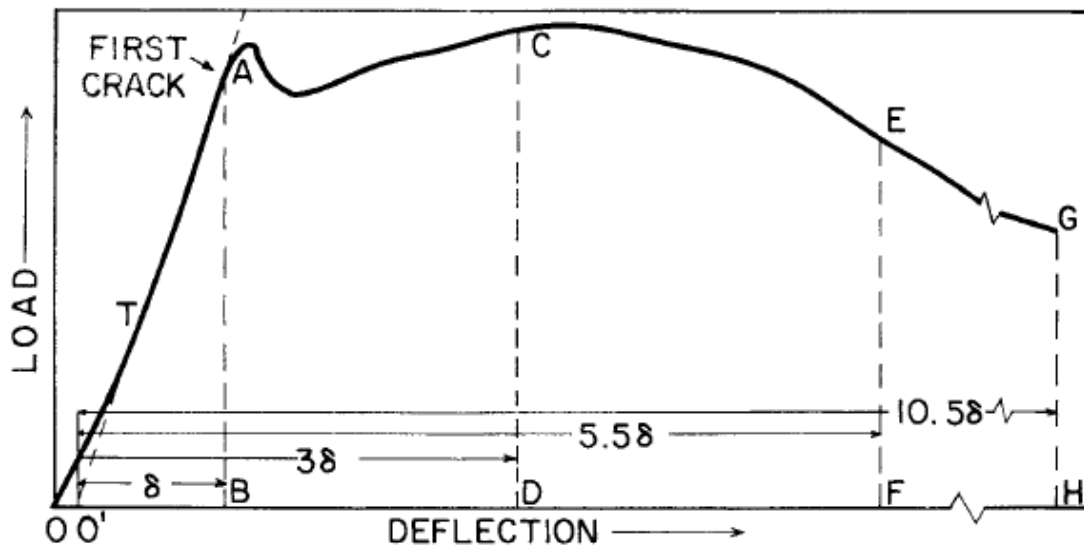


Figure 52 - Schematic of a load versus midspan deflection for the ASTM C 1018 standard [from 2].

All deflection values used to compute the indices are based off of a new zero-point labeled as  $O'$  in Figure 52. This zero-point,  $O'$ , is determined by extending a tangent line from the initial loading curve back to a zero load. The deflection at first cracking in the concrete is recorded as  $\delta$  and the area under the load-deflection curve up to  $\delta$  is recorded as  $I_0$ , see equation 13.

$$I_0 = \text{area}(P \cdot \delta) \Big|_0^\delta \quad (13)$$

Other indices are determined by computing the area under the load versus deflection curve up to some multiple of the first cracking deflection  $\delta$ , such as  $3\delta$ ,  $5.5\delta$  or  $10.5\delta$ , then normalized by  $I_0$  (see equations 14a - 14c).

$$I_5 = \frac{\text{area}(P \cdot \delta)|_0^{3*\delta}}{I_0} \quad (14a)$$

$$I_{10} = \frac{\text{area}(P \cdot \delta)|_0^{5.5*\delta}}{I_0} \quad (14b)$$

$$I_{20} = \frac{\text{area}(P \cdot \delta)|_0^{10.5*\delta}}{I_0} \quad (14c)$$

Ratios  $R_{5,10}$  and  $R_{10,20}$  are computed as in equation 15a and 15b, respectively, to give an estimate of the magnitude and sustainability of the post-peak behavior of the FRC mixture.

$$R_{5,10} = 20(I_5 - I_{10}) \quad (15a)$$

$$R_{10,20} = 10(I_{10} - I_{20}) \quad (15b)$$

#### *JCI-SF4*

The Japan Concrete Institute SF4 standard [22] was developed for computing flexural strength and residual properties of a FRC beam. The standard requires the load to be carried out to a specified deflection based on the span  $S$  of the beam. In the case of a 6x6x21 inch beam, where the span is 18 inches, the maximum required deflection corresponds to  $S/150$  or 0.12 inches (3 mm). The modulus of rupture is computed similar to the previous standard, except the peak load  $P_I$  is used in the calculation, see equation 16.

$$MOR = \frac{P_1 S}{bd^2} \quad (16)$$

Figure 53 shows a schematic of the load versus deflection curve for defining the terms used here. A toughness  $T_{150,3}$  parameter is computed as the area under the curve up to 3mm, seen in equation 17. This toughness parameter is used to compute the equivalent residual strength  $f_{e,3}$  and thus also affects the equivalent residual strength ratio  $R_{e,3}$  (see equations 18 and 19). As a result the equivalent residual strength and residual strength ratio incorporate the entire post-peak performance of the FRC up to a deflection of 3 mm rather than an instantaneous residual strength and residual strength ratio at a 3 mm deflection.

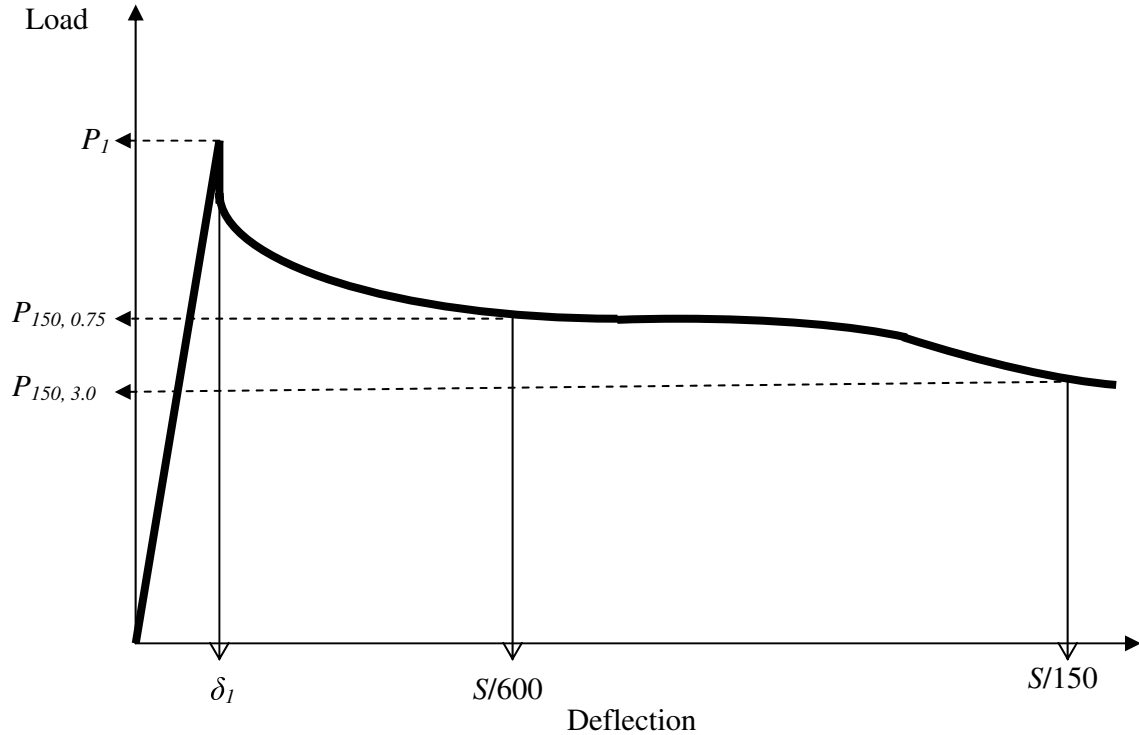


**Figure 53 - Schematic of the load versus midspan deflection for ASTM C1609 and JCI-SF4 standards.**

$$T_{150,3} = \text{area}(P \cdot \delta)|_0^{S/150} \quad (17)$$

$$f_{e,3} = \frac{T_{150,3} S}{bd^2} \quad (18)$$

$$R_{e,3} = \frac{f_{e,3}}{MOR} * 100 \quad (19)$$

### *ASTM C 1609*

A modification to the original ASTM C 1018 standard for beam toughness was created specifically to better describe the post-peak or residual behavior of FRC. The residual post-peak behavior is described primarily with three terms: the residual strength  $f_{150,3}$ , the toughness  $T_{150,3}$  and the residual strength ratio  $R_{150,3}$  (calculated based on the  $f_{150,3}$  and  $MOR$ , but not part of the ASTM standard). Equations 20-21 show the calculations for these residual properties. The major difference compared to the JCI method is that the load at 3mm, see Figure 53 is used for computing the residual strength  $f_{150,3}$  rather than the area up to 3mm.

$$f_{150,3} = \frac{P_{150,3} S}{bd^2} \quad (20)$$

$$R_{150,3} = \frac{f_{150,3}}{MOR} * 100 \quad (21)$$

### ***Beam Flexural Toughness Testing Standards Comparison***

Using the ASTM C 1018 standard, the indices and ratios does provided some empirical insight on how a mixture performs compared to other mixtures. However, it was unclear how to link the ASTM results to FRC slab performance (load capacity and crack width). ASTM C 1609 and JCI standards were similar in that they both record residual strength values and ratios at 3mm deflection. The main difference being the ASTM standard residual strength value was determined solely on the load level resisted by the specimen at 3mm while the JCI method was computed as the average load resisted by the specimen up to 3mm. Note for plain (un-reinforced) concrete, the residual properties based on ASTM C 1609 were zero; ASTM C 1018 and JCI standards do compute some residual values for the un-reinforced concrete samples. In general, for increasing volume fraction of a given fiber, the residual flexural strength, toughness, and residual strength ratio all increase. Averaged flexural properties of the FRC specimens at each volume fraction for each fiber type are shown in Table 18.

**Table 18 – Average Flexural and Residual Properties of FRC**

| Fiber Type         | Volume Fraction | Dosage Used (lb/yc <sup>3</sup> ) | Peak Load (lb) | Flexural Strength (MOR) (psi) | JCI-SF4 Standard |               | ASTM C 1609 Standard |                     |                 | ASTM C1018 Standard |          |                |          |                 |   |   |   |
|--------------------|-----------------|-----------------------------------|----------------|-------------------------------|------------------|---------------|----------------------|---------------------|-----------------|---------------------|----------|----------------|----------|-----------------|---|---|---|
|                    |                 |                                   |                |                               | $f_{e,3}$ (psi)  | $R_{e,3}$ (%) | $f_{150,3}$ (psi)    | $T_{150,3}$ (lb-in) | $R_{150,3}$ (%) | $I_5$               | $I_{10}$ | $R_{5,10}$ (%) | $I_{20}$ | $R_{10,20}$ (%) |   |   |   |
| Straight Synthetic | 0.26            | 4.0                               | 5,472          | 456                           | 92               | 20.2          | 83                   | 130                 | 18.3            | -                   | -        | -              | -        | -               | - | - | - |
|                    | 0.29            | 4.5                               | 9,276          | 773                           | 125              | 16.2          | 95                   | 180                 | 12.3            | -                   | -        | -              | -        | -               | - | - | - |
|                    | 0.33            | 5.0                               | 8,138          | 680                           | 148              | 21.8          | 126                  | 193                 | 18.5            | 2.8                 | 3.9      | 21.3           | 5.7      | 17.8            | - | - | - |
|                    | 0.50            | 7.7                               | 8,088          | 699                           | 276              | 39.5          | 224                  | 348                 | 32.1            | 3.0                 | 4.7      | 34.4           | 8.3      | 35.6            | - | - | - |
|                    | 0.58            | 8.9                               | 8,939          | 745                           | 347              | 46.6          | 382                  | 500                 | 51.3            | -                   | -        | -              | -        | -               | - | - | - |
| Twisted Synthetic  | 0.30            | 4.6                               | 8,101          | 675                           | 84               | 12.5          | 68                   | 120                 | 10.1            | -                   | -        | -              | -        | -               | - | - | - |
|                    | 0.50            | 7.7                               | 6,487          | 541                           | 143              | 26.4          | 135                  | 203                 | 24.9            | -                   | -        | -              | -        | -               | - | - | - |
| Crimped Synthetic  | 0.40            | 6.1                               | 8,160          | 673                           | 131              | 19.8          | 129                  | 190                 | 19.5            | 2.8                 | 3.8      | 19.8           | 5.3      | 14.7            | - | - | - |
| Crimped Steel 1    | 0.50            | 66.0                              | 9,052          | 766                           | 269              | 35.1          | 185                  | 347                 | 24.1            | 3.2                 | 5.1      | 37.0           | 8.6      | 35.1            | - | - | - |
| Crimped Steel 2    | 0.40            | 52.8                              | 8,828          | 710                           | 117              | 16.5          | 64                   | 175                 | 8.9             | 3.0                 | 4.4      | 27.9           | 6.4      | 20.4            | - | - | - |
|                    | 0.50            | 66.0                              | 6,511          | 543                           | 160              | 29.5          | 88                   | 227                 | 16.3            | -                   | -        | -              | -        | -               | - | - | - |
| Hooked End 1       | 0.19            | 25.0                              | 9,145          | 762                           | 132              | 17.3          | 108                  | 190                 | 14.2            | -                   | -        | -              | -        | -               | - | - | - |
|                    | 0.35            | 46.2                              | 8,278          | 678                           | 291              | 42.8          | 234                  | 385                 | 34.5            | 3.5                 | 5.8      | 47.5           | 10.3     | 44.7            | - | - | - |
|                    | 0.38            | 50.2                              | 8,911          | 743                           | 424              | 57.0          | 467                  | 610                 | 63.0            | -                   | -        | -              | -        | -               | - | - | - |
| Hooked End 2       | 0.30            | 39.6                              | 9,795          | 816                           | 292              | 35.7          | 305                  | 420                 | 37.4            | -                   | -        | -              | -        | -               | - | - | - |
|                    | 0.55            | 72.6                              | 9,754          | 813                           | 396              | 48.7          | 377                  | 570                 | 46.4            | -                   | -        | -              | -        | -               | - | - | - |

A plot of the residual strength ratios based on the JCI method and ASTM C 1609 calculations is shown in Figure 54. The JCI standard residual strength ratio was generally greater than with the  $R_{150,3}$  value. For design purposes, if a concrete mixture were to be created to meet a minimum residual strength ratio ( $R_{150,3}$ ), the concrete mixture would result in a high volume fraction of fibers than a specification based on the JCI standard.

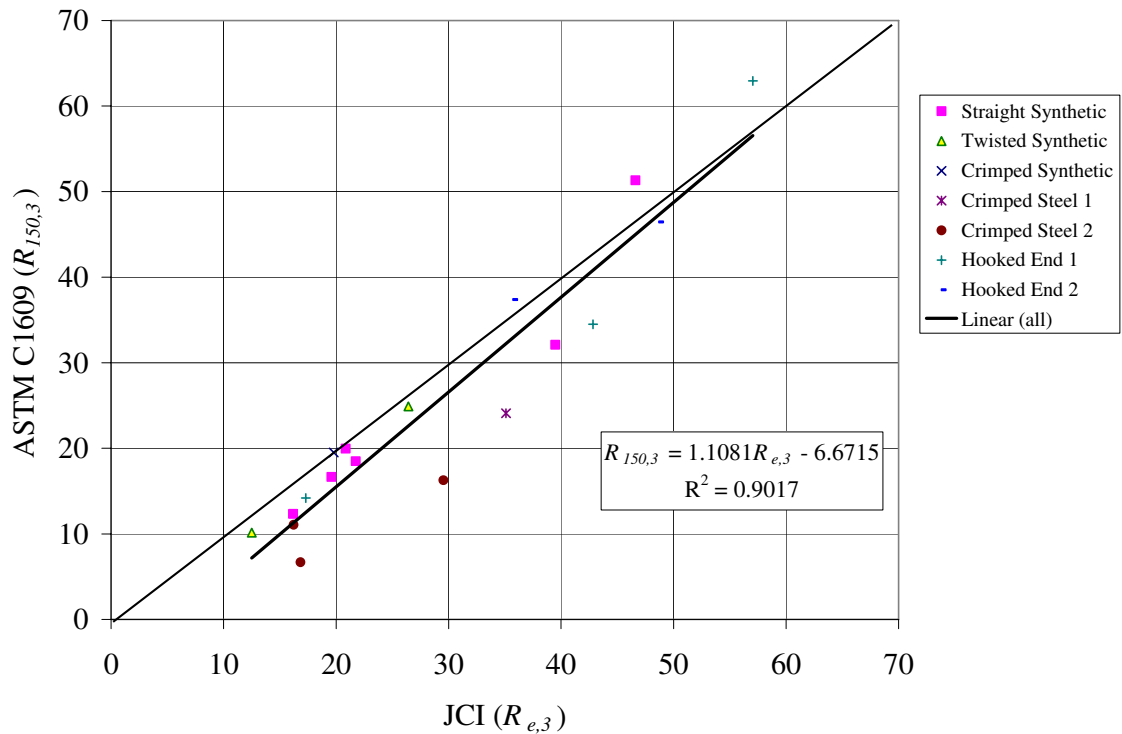


**Figure 54 - Comparison between the residual strength ratios of ASTM C 1609 and JCI-SF4 standards.**

*Fiber Type and Volume Effects*

Every fiber type will generate a different post-peak performance in a given concrete mixture. Using the same amount of fibers either by mass or volume fraction does not produce the same residual strength for different fiber types. In order for a specification to

be created on the amount of fibers to use, the mass or volume fraction should not be used. Instead a performance based criteria such as  $R_{e,3}$  or  $R_{150,3}$  should be used.

Several similar residual strength values can be found from Table 18; a  $R_{e,3}$  value of 20% was obtained for 4 lb/yd<sup>3</sup> or 0.26% of the straight synthetic FRC and was estimated to be for about 55 lb/yd<sup>3</sup> or 0.42% of a crimped steel 2 FRC mixture. In other words a larger volume of steel fibers of a certain type are required compared to a certain type of synthetic fibers to obtain the same toughness level. For the same volume fraction, say 0.50%, the  $R_{150,3}$  for straight synthetic FRC was 32%, twisted synthetic was 25%, crimped steel 1 was 24%, crimped steel 2 was 16%, and hooked end 2 was estimated to be 45%. Synthetic FRC had repeatable fracture and flexure performance characteristics between samples due to the consistency between batches and at different ages. Crimped steel FRC had the greatest variability in fracture and flexural performance at low volume fractions.

The residual strength ratio values are not absolute for each specified fiber type or volume fraction. The concrete mixture design also impacted the MOR and residual strength properties. For example, the 0.29% straight synthetic FRC beams had a high MOR value and thus reduced residual strength ratios compared to 0.26% volume fraction beams in a different concrete mixture.

### *Secondary Peak*

With the volume fractions less than 0.5% (or even lower volume fractions of 0.19% at 28 days seen in Figure 46) a secondary peak in the residual curve was observed. The mechanism to describe this behavior was predicted to correspond to when all fibers were de-bonding from the matrix and beginning to pullout of the matrix. Some micromechanical models described in Appendix A have attempted to incorporate this secondary peak in their localized tension softening descriptions. Further investigation is needed to characterize this secondary peak in terms of fiber content, fiber type, the number of fibers bridging the fractured surface, and bonding strength with the concrete matrix.

### *Summary*

Seven types of fibers were compared at volume fractions between 0.2% to 0.6% volume fractions for their flexural and residual properties. Equivalent residual strength properties were dependent on the fiber type in addition to the volume fraction or mass fraction of the fiber in FRC. The JCI-SF4 or ASTM C 1609 methods were both effective to determine the residual properties of these FRC mixtures. More conservative fiber content would be selected in design of FRC if performance-based residual properties were determined from the ASTM C 1609 calculations compared to the JCI-SF4 method.

## **CHAPTER 7: CONCLUSION**

Fracture mechanics testing of concrete mixtures can enhance the performance prediction of rigid pavements in the field. Although strength can be used to estimate the event of a crack in concrete, the fracture properties can better describe the rate of crack growth and crack widths seen in the pavement. Various studies were performed, such as a two-layer functionally graded concrete beam, a composite hot-mixed asphalt and concrete beam on an elastic foundation, and concrete material constituent and proportioning for ultra-thin whitetopping, to determine fracture properties and correlate them use in rigid pavement designs. A summary of the conclusions found from each study is listed below.

Various fracture properties of paving mixtures were investigated at different ages and with different mixture proportions. The most significant factors on fracture properties were fiber-reinforcement and age effect. Other factors such as coarse aggregate type were also studied in this report. Recycled concrete as a coarse aggregate was found to have the lowest initial and total fracture properties. Specimens of different mixtures were tested at ages between 7 and 90 days and a statistical fit was derived to match their fracture toughness curve. A testing age of 28 days or greater was determined to be the most reasonable to determine the fracture properties of paving concrete mixtures. Current empirical equations presented in the literature (using compressive strength, w/cm ratio, aggregate type and size) were insufficient to characterize the fracture energy performance of the mixtures studied herein.

Four layered configurations of FRC and un-reinforced concrete mixtures in a notched beam were tested for their fracture properties. Full-depth FRC beams demonstrated the greatest fracture energies as expected. Beams containing a synthetic FRC layer were found to be best at mitigating crack propagation when the fibers were implemented nearest to the crack tip. On the other hand, when crimped steel FRC layers were examined the number of fibers bridging the fracture area was too low to produce repeatable results.

Composite beams composed of concrete cast onto hot-mixed asphalt were tested on a clay subgrade to predict the fracture performances of UTW mixtures found in the field. Soil conditions affected the vertical deflection readings of each test. However, the percent load drop after each beam cracked was determined to be effective at differentiating the performance between fiber-reinforced concrete and plain concrete mixtures used for UTW projects. No significant ranking of plain concrete mixtures was seen using the test configuration. Fracture properties derived from SEN(B) specimens alone were misleading as they too did not always correlate to the performance seen in the field. Overall, the behavior and performance of UTW systems depend on the combined effect of loading, concrete material fracture properties, geometry of the slab, and support condition. A 3D fracture model and testing is required to validate the performance of each UTW mixture.

A study of 7 types of fibers types at varying volume fractions from 0.2 to 0.6% in concrete were examined under flexure testing. ASTM and JCI standards on flexural and

residual strengths were compared. A small collection of MOR and residual properties according to different standards was created to aid in estimating the amount of fibers for a particular type of fibers would be needed to reach a certain residual strength ratio value. All fibers are not equal as far as their impact on residual strength or fracture energy. A residual performance-based specification is recommended for future FRC design. ASTM C 1609 provides slightly more conservative FRC design based on residual strength ratio values compared to the JCI method.

#### *Future Research*

Overall, the fracture energy determined using the TPFM or the Hillerborg method can be a useful property to describe the post-cracked concrete performance. A test to describe the post-cracking behavior should be implemented into current design of rigid pavements. Fracture properties can be used in models, such as finite element models, to analyze a variety of materials and structural configurations to predict field slab performance. Through further correlation between testing and modeling, the post-cracking fracture properties can be used to describe the load carrying capacity of slabs and load transfer efficiency across joints or cracks. Design guidelines should incorporate these additional material characteristics in order to improve predictions of future rigid pavement performance.

## REFERENCES

1. Anderson, T.L. *Fracture Mechanics Fundamentals and Applications*. Third Edition. Taylor & Francis Group: Boca Raton, FL, 2005.
2. ASTM, *Annual Book of ASTM Standards, Section 4 Construction*. American Society for Testing and Materials International: Philadelphia, Pennsylvania, 2004.
3. Balaguru, P.N. and S.P. Shah. *Fiber Reinforced Cement Composites*. McGraw-Hill: New York, NY, 1992.
4. Bazant, Zednek, P. and Emilie Becq-Giraudon. "Statistical prediction of fracture parameters of concrete and implications for choice of testing standard." *Cement and Concrete Research*, Vol. 32, 2002, pp. 529-556.
5. Bazant, Zdenek P. and Jaime Planas. *Fracture and Size Effect in Concrete and Other Quasibrittle Materials*. CRCP Press: New York, NY, 1998.
6. Bazant, Zdenek P., Qiang Yu, and Goanqseup Zi. "Choice of standard fracture test for concrete and its statistical evaluation." *International Journal of Fracture*, Vol. 118, No. 4, 2002, pp. 303-337.
7. Braham, Andrew. "The Investigation of Asphalt Interlayers Between Existing Portland Cement Concrete Pavements and Portland Cement Concrete Overlays", CEE 506 Pavement Design and Analysis II Term Project, Spring 2006.
8. Bordelon, Amanda. "SEM Lab" CEE500E Experimental Characterization of Materials Laboratory Report, Spring 2007.
9. Bentur, A, S. Diamond and S. Mindess. "Cracking Process in Steel Fiber Reinforced Cement Paste". *Cement and Concrete Research*, Vol. 15, 1985, p331-342.
10. Bentur, A, S. Diamond and S. Mindess. "The Microstructure of the Steel Fiber Cement Interface", *Journal of Material Science*, Vol. 20, 1985, p3610-3620.
11. Bentur, A. and S. Mindess. *Fibre Reinforced Cementitious Composites*. Elsevier Applied Science: New York, NY, 1990.
12. Cable, J. K. and D.P. Frentress. "Two-Lift Portland Cement Concrete Pavements to Meet Public Needs." Federal Highway Administration Technical Report, 2004.
13. Cervantes, Victor, Jeffery Roesler, and Amanda Bordelon. "Fracture and Drying Shrinkage Properties of Concrete Containing Recycled Concrete Aggregate", *CEAT Technical Note*, No. 29, 2007.

14. Chupanit, Punya and Jeffery R. Roesler. "Fracture Energy Approach to Characterize Concrete Crack Surface Roughness and Shear Stiffness", approved for 2005 publication in the *ASCE Journal of Materials in Civil Engineering*, 2005.
15. Donovan, Phillip and Matthew Strickler. "Comparison of Fiber Reinforced Concretes Using ASTM C1018 and C1609", CEE 506 Pavement Design and Analysis II Term Project, Spring 2007.
16. Fu, Shao-Yun, and Bernd Lauke. "Effects of Fiber Length and Fiber Orientation Distributions on the Tensile Strength of Short-Fiber-Reinforced Polymers", *Composites Science and Technology*, Vol. 56, 1996, p. 1179-1190.
17. Gopalaratnam, and Shah. "Tensile Failure of Steel Fiber-Reinforced Mortar", *ASCE Journal of Engineering Mechanics*, Vol. 113, No. 5, 1987 p. 635-652.
18. Hannant, D. J. *Fibre Cements and Fibre Concretes*. John Wiley & Sons: New York, NY, 1978.
19. Hillerborg, A. The Theoretical Basis of a Method to Determine the Fracture Energy  $G_f$  of Concrete. *Material and Structures, RILEM*, Vol. 16, 1985, pp. 291-296.
20. Ioannides, Anastasios M. "Evaluation of UTW and Whitetopping Design Procedure", Interim Report for the Illinois Center for Transportation, March 2007.
21. Jansen, D.C., W.J. Weiss, and S.H.F. Schleuchart. "Simplification of the Testing and Analysis Procedure for the Two Parameter Fracture Model." *14<sup>th</sup> Engineering Mechanics Conference Proceedings*, 2000.
22. Japan Concrete Institute. "Standard test method for flexural strength and flexural toughness of fiber reinforced concrete" Japan Concrete Institute, Standard SF4, 1983, pp. 45-51.
23. Jenq, Y. and S.P. Shah. Two Parameter Model for Concrete. *Journal of Engineering Mechanics*, Vol. 111, No. 10, 1985, pp. 1227-1241.
24. Karihaloo, B.L., and P. Nallathambi. "Notched Beam Test: Mode I Fracture Toughness", from *RILEM Report 5 Fracture Mechanics Test Methods for Concrete*, edited by S.P. Shah and A. Carpinteri. Chapman and Hall: New York, 1991, pp. 1-86.
25. Lange, David A. and Chang Joon Lee. "Evaluation of Six Fiber Reinforced Concrete Materials." Internal Report, Department of Civil and Environmental Engineering, University of Illinois Urbana-Champaign, June 24, 2004.
26. Leung, Christopher K.Y, and Y.Philip Geng. "Micromechanical Modeling of Softening Behavior in Steel Fiber Reinforced Cementitious Composites." *International Journal of Solid Structures*, Vol. 35, No. 31-32, 1997, pp. 4205-4222.

27. Leung, Christopher K.Y., Raymond Lai, and Augustus Y.F. Lee. "Properties of wet-mixed fiber reinforced shotcrete and fiber reinforced concrete with similar composition", *Cement and Concrete Research*, Vol. 35, No. 4, 2005, pp.788-795.
28. Li, V.C. "Performance Driven Design of Fiber-Reinforced Cementitious Composites." *Fibre Reinforced Cement and Concrete*. Edited by R.N. Swamy. E&FN Spon: London, 1992.
29. Li, V.C. "Postcrack Scaling Relations for Fiber Reinforced Cementitious Composites." *ASCE Journal of Materials in Civil Engineering*, Vol. 4, No. 1, 1992, pp. 41-57.
30. Li, V.C. and C.K.Y. Leung. "Steady-State and Multiple Cracking of Short Random Fiber Composites." *ASCE Journal of Engineering Mechanics*, Vol. 118, No. 11, 1992, pp. 2246-2264.
31. Li, V.C., H. Stang, H. Krenchel. "Micromechanics of crack bridging in fibre-reinforced concrete." *Materials and Structures*, Vol. 26, 1993, pp. 486-494.
32. Li, V.C., Y. Wang and S. Backer. "Effect of inclining angle, bundeling and surface treatment on synthetic fibre pull-out from a cement matrix." *Composites*, Vol. 21, No. 2, 1990, pp. 132-140.
33. Lin, Deng-Fong, and Her-Yuan Wang. "Forensic Investigation of Ultra-Thin Whitetopping Failures in Taiwan", *Journal of Performance of Constructed Facilities*, Vol. 19, No. 2, 2005, pp. 165-171.
34. Lok, Tat-Seng, and Jin-Song Pei. "Flexural Behavior of Steel Fiber Reinforced Concrete", *Journal of Materials in Civil Engineering*, Vol. 10, No. 2, 1998, p. 86-97.
35. Mindess, Sidney, J. Francis Young, and David Darwin. *Concrete* 2<sup>nd</sup> edition. Prentice Hall: Upper Saddle River, NJ, 2003.
36. National Concrete Pavement Technology Center. "Guide to Concrete Overlay Solutions", Iowa State University CP Tech Center, January 2007.
37. Park, Kyoungsoo. "Concrete fracture mechanics and size effect using a specialized cohesive zone model", *MS Thesis*, University of Illinois at Urbana-Champaign, 2005.
38. Park, K., G.H. Paulino, A. Bordelon, and J.R. Roesler. "Experimental based softening model for fiber reinforced concrete". (To be submitted for journal publication), 2007.

39. Pereira, Deividi Da S., Jose T. Balbo and Lev Khazanovich. "Theoretical and field evaluation of interaction between ultra-thin whitetopping and existing asphalt pavement". *International Journal of Pavement Engineering*. Vol. 7, No. 4, 2006, pp. 251-260.
40. Ravindrarajah, R. S. and C.T. Tam. Flexural Strength of Steel Fibre Reinforced Concrete Beams. *International Journal of Cement Composites and Lightweight Concrete*, Vol. 6, No. 4, 1984, pp. 273-278.
41. Roesler, Jeffery R., Salah A. Altoubat, David A. Lange, Klaus-Alexander Rieder, and Gregory R. Ulreich. "Effect of Synthetic Fibers on Structural Behavior of Concrete Slabs-on-Ground." *ACI Materials Journal*, Vol. 103, No. 1, 2006, pp. 3-10.
42. Roesler, Jeffery, Glaucio Paulino, Cristian Gaedicke, Amanda Bordelon, and Kyoungsoo Park. "Fracture Behavior of Functionally Graded Concrete Materials (FGCM) for Rigid Pavements", accepted for publication *Transportation Research Record*, 2007.
43. Shah, Surendra P., Stuart E. Swartz and Chengsheng Ouyang. *Fracture Mechanics of Concrete: Applications of Fracture Mechanics of Concrete, Rock and Other Quasi-Brittle Materials*. Wiley-Interscience: New York, NY, 1995.
44. Transtec Group, The. 2005. Whitetopping system analysis tool: Design. Austin, TX: The Transtec Group. <http://www.whitetopping.com/design.asp>.
45. Tursun, Deniz. "Ultra Thin White Topping Testing Effort", CEE 506 Pavement Design and Analysis II Term Project, Spring 2006.
46. Visalvanich, Kitisak, and Antoine E. Naaman. "Fracture Model for Fiber Reinforced Concrete." *ACI Materials Journal*, Vol. 80, No. 2, 1983, pp. 128-138.
47. Winkelman, Tom. "Illinois' Whitetopping Experience, A Practical Approach". *International Conference on Best Practices for Ultrathin and Thin Whitetoppings Conference Proceedings*, April 2005.
48. Zhang, J. and V.C. Li. Monotonic and fatigue performance in bending of fiber-reinforced engineered cementitious composite in overlay system. *Cement and Concrete Research*, Vol. 32, 2002, pp. 415-423.
49. Zollinger, Dan G., Tianxi Tang and Rae H. Yoo. "Fracture Toughness of Concrete at Early Ages". *ACI Materials Journal*, Vol. 90, No. 5, 1993, pp. 463-471.

## **APPENDIX A: MICROMECHANICAL VIEW OF FIBER-REINFORCED CONCRETE BEHAVIOR**

Fiber-reinforced concrete (FRC) is a composite material composed of discrete fiber materials acting as local reinforcement in a concrete matrix. As a composite, the overall material properties change based on the interaction and volume ratio of the fiber relative to the matrix. The major material properties of FRC which are modified from plain concrete are: increased tensile strength (particularly for high volume fractions), increased toughness, reduced crack widths and crack propagation rates, reduced shrinkage, increased fatigue resistance, and impact resistance, increased post-cracking ductility, and lower rheological properties [3, 11, and 18].

Fibers may be added for plastic shrinkage cracking, crack width control, toughness, and increased slab capacity. In this research for the structural design of concrete pavements, the toughness, crack width and increased slab flexural capacity are key design objectives for fibers. Only fibers which can impart significant structural benefit are of interest in this research and therefore low modulus fibers used for plastic shrinkage control are not of interest. Beam flexural testing of the various structural fiber types can be made to give a quantitative measure of the fiber effectiveness by means of the FRC toughness.

## ***FRC Design and Construction***

A large variety of fiber materials and geometric properties exist. By optimizing the characteristics of the fiber (material and geometry), an improved performance in the FRC material can be obtained as long as the primary properties desired are known (workability, compaction, bonding, and toughness).

### *Material*

The fiber material is chosen to be one with a greater composite flexural strength or increased ductility relative to concrete. The elastic modulus of fibers can be lower than the concrete matrix (in the case of cellulose, nylon, organic, and polypropylene fibers) or can be higher than the concrete matrix (in the case of glass, steel, and carbon fibers) [18]. As related to the stiffness of the fiber material, some softer fibers tend to bend or twist when mixed with concrete while the stiffer fibers remain in their original shape and structure. This alteration can impact bonding issues, clumping occurrences, and stress reduction within the fiber.

### *Geometry*

The fibers studied here are discrete short fibers; their length and diameter must be considered in design. An aspect ratio is often used which is the length divided by the diameter of the fiber. Fibers can also come in various cross-sectional shapes such as circular, square or rectangular. The effective cross-sectional area of the fiber is sometimes required in analyzing the theoretical performance of the composite material. Fibers can also come as straight, crimped, twisted, hooked or even hoop shapes. These

geometrical variations highly complicate the theoretical behavior of the composite material. In general most analyses assume the fiber to be a straight rigid member for simplification.

### *Construction*

FRC mixtures have been reported to have reduced workability or slump and can cause more difficulty to finish the concrete surface especially for volume fractions at 1 percent or greater [3, 11, and 18]. The fibers with larger aspect ratios and higher volume fractions may clump and bind up together in the mixture rather than uniformly dispersing. Weak zones in the mixture are formed because the clumps have little cement within to provide the strength of the bulk paste and outside of the clumps there are more regions of concrete unreinforced. The best technique to minimize fiber clumping and enhance fiber dispersion is to use a water reducer or super-plasticizer or to increase the effectiveness of the cementitious matrix. This technique is very effective at increasing workability and improving the ability to finish the concrete.

### *Details on Fibers from this Report*

Descriptions on all fiber types investigated in this report can be found in Table 16. One of the primary fiber types studied in this research is a straight synthetic fiber made of a polypropylene/ polyethylene blend. These fibers are initially straight but tend to bend or twist after mixing. The fibers are composed of long extruded fibrillated fiber strands in a rectangular cross-section. The fibers are considered to be a structural fiber because they are larger in size, strength, and modulus than those used for plastic shrinkage. These

fibers were specifically designed to improve the flexural and ultimate load capacity of concrete slabs.

### *Matrix-Fiber Interaction*

The bond that occurs between the fiber and concrete becomes important when determining how the material fails. The bonding strength between the fiber and matrix depends on the strength of the concrete matrix, the age of the concrete, the density of the concrete, the geometry of the fiber and the fiber surface characteristics.

Similar to aggregates in concrete, there is an interfacial transition zone along the fiber surface that separates the fiber from the bulk concrete material. This concept has been described by Bentur and others [9 - 11] as seen in Figure 55. According to the images, as one looks closer into the microstructure of the fiber interfacial zone, large crystals of calcium hydroxide can be seen in the SEM image (Figures 55b, 55c, and 55e) along with porous regions between the crystals along the interface. The problems with the interfacial transition zone are a reduced strength region and inconsistent bond strength. With a lack of calcium silicate hydrate gel often seen in the bulk cement paste, the strength of this region is reduced so cracking is likely to initiate as seen in the Figures 55a, 55c, 55d, and 55f. Areas of higher porosity are generally where cracks will propagate along or around.

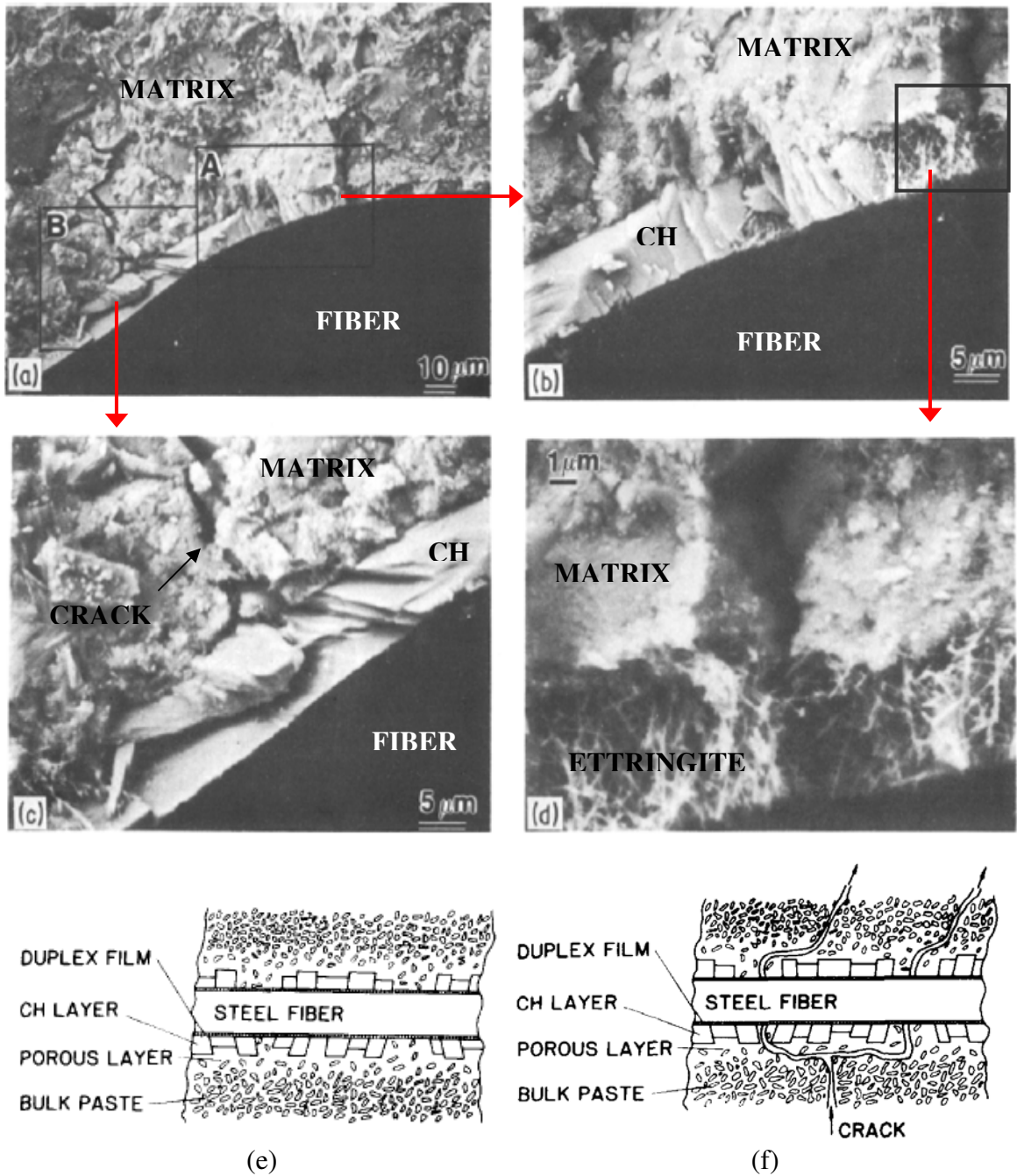


**Figure 55 – (a-d) SEM images of the fiber-cement interface [from 10] and (e-f) a microstructure schematic of FRC [from 9].**

This interfacial area around the fibers is difficult to quantify even for a micromechanical model due to the highly variable material which actually bonds the bulk matrix to the fiber surface. When fibers pull-out of a matrix, it is generally assumed that the porous

interfacial area is what breaks and the fibers slip out. Some theoretical models therefore include: static shear strength  $\tau_s$  to quantify the bonded interface and dynamic shear strength  $\tau_d$  to quantify the friction that occurs between the fiber and the bulk matrix.

A brief study to understand the microstructure of the interface between the fiber and concrete matrix was performed [8]. A scanning electron microscope (SEM) was used with a secondary electron image of the fracture surface of a fiber-reinforced concrete mixture at roughly 1 year old to gain an idea of what these fibers look like after testing. These images can be seen in Figures 56 and 57.



**Figure 56 - Secondary electron image of a straight synthetic fiber in concrete matrix.**

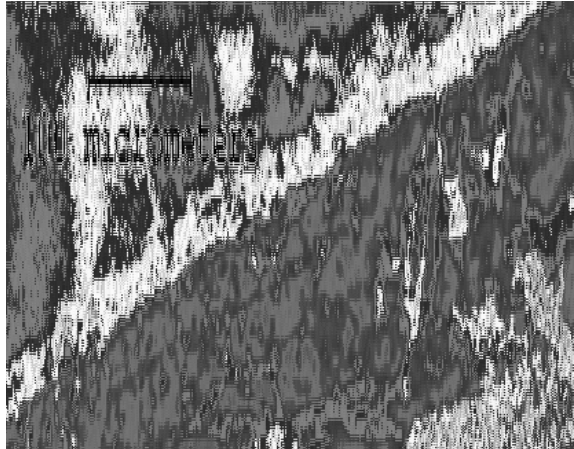


**Figure 57 – A straight polypropylene/polyethylene fiber pulled out from the concrete matrix.**

A crack can be seen in Figure 56 extending along the fiber surface most likely due to the presents of the interfacial transition zone. However, with SEM imaging, specimens are often subjected to high vacuums which can cause cracking after the specimen is taken from the concrete. The straight synthetic fibers do bond well with the concrete and the fibers typically pull-out of the matrix rather than rupturing. However, some of the straight synthetic fibers seem to shear within the fiber and fray as it pulls out of the concrete matrix as seen in Figure 57. The additional fact that some of the fibers bend within the concrete matrix, leads to an increase in pull-out load, and may also lead to the fiber shearing. These factors can alter the fracture properties of a FRC mixture. Every fiber type used in a concrete will demonstrate different fracture and residual strength properties that must be understood in order to determine the amount of fibers to use. Chapter 6 investigates the differences between fiber type and volume fraction in residual properties.

## *Stress Distribution Theory in FRC Composites*

Some of the earliest studies on the effect of fibers on cement and concrete have been performed by Laws, Aveston, Allen, Cox and Krenchel from the 1950s to 1970s [3, 11, and 18]. The majority of the early studies looked at steel straight fibers for simplicity in analysis. Direct tension tests were often performed on single fibers across a cracked concrete to understand the influence of orientation and length. Equation A1 for pre-cracked composite stress  $\sigma_c$  has been developed [3, 11, and 18] and shown below

$$\sigma_c = \eta_\theta \eta_l \sigma_f V_f + \sigma_m (1 - V_f) \quad (\text{A1})$$

where  $\sigma_f$  and  $\sigma_m$  are the fiber and matrix stresses respectively,  $\eta_\theta$  and  $\eta_l$  are orientation and length efficiency factors, respectively, and  $V_f$  is the fiber volume fraction. The equation assumes there is zero Poisson's ratio in the fiber and matrix, fibers and the matrix exhibit equal amounts of strain ( $\varepsilon_c = \varepsilon_f = \varepsilon_m$ ), and all fibers are aligned in the direction of the loading.

Various efficiency factors for the pre-cracked concrete condition are shown in Table 19. The 3D orientation factor depends on whether the specimen is constrained in other dimensions; because various wall effect issues impact the effective number of fibers across the testing plane. The length of fibers across a plane depends on the original fiber length  $L_f$  and the critical fiber length  $L_c$ . The modified version of the length orientation factors, shown in Table 19, account for any variation in strain between the fiber and matrix ( $\varepsilon_c / \varepsilon_f$ ). The critical fiber length can be determined by the fiber strength  $\sigma_f$ , the

cross-sectional area  $A_f$ , the density  $\rho$ , and the shear strength  $\tau_f$  between the fiber and matrix. Fibers longer than the critical length often have a greater tendency to clump or ball and bind. Fibers longer than the critical length often rupture instead of pull-out of the matrix.

The statistical distribution of fibers in terms of their orientation and location within a specimen can be determined using x-rays for steel fibers. This technique may be used to confirm the number of fibers located in a fracture plane and would be useful to predicting the fracture performance especially with low volume fractions of steel FRC. No testing method is known for examining the statistical distribution of synthetic fibers in concrete.

**Table 19 – Orientation and Length Efficiency Factors for FRC [after 11]**

| orientation | $n_\theta$    |             |
|-------------|---------------|-------------|
|             | unconstrained | constrained |
| 1D aligned  | 1             | 1           |
| 2D random   | 1/3           | 3/8         |
| 3D random   | 1/6           | 1/5         |

| length           | $n_l$  |   |
|------------------|--|---|
|                  | original ( $\varepsilon_m = \varepsilon_f$ ) | modified  |
| $L_f \leq L_c$ * | $L_f / (2 L_c)$                              | $L_f / (2 L_c) * \varepsilon_c / \varepsilon_f$       |
| $L_f \geq L_c$   | $1 - L_c / (2 L_f)$                          | $1 - (L_c / (2 L_f)) * \varepsilon_c / \varepsilon_f$ |

$$* L_c = 2 \sigma_f A_f / (\rho \tau_f)$$

Once cracking occurs in the matrix, the crack widens with increasing load and the randomly orientated fibers pull out in the direction of the tensile load. Sometimes the pullout also elastically stretches the fibers. In addition, for sharp angles of fiber

orientation, the concrete near the crack face may crush or spall under the fiber re-alignment [26], see Figure 58. The bending that induces in the fibers from the re-alignment under tension generates a greater stress within the fiber; the fiber will undergo greater strain or stretching. However once the fiber is re-aligned, the overall composite is capable of holding more loads (aligned fibers carry more efficiency for load transfer across the matrix).

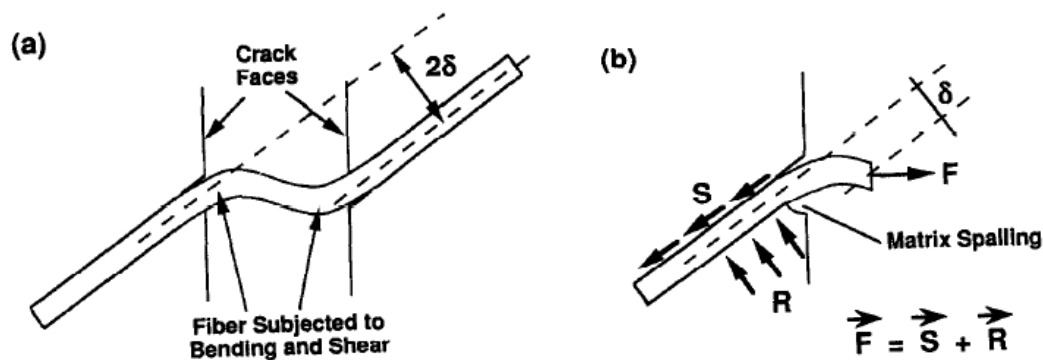


**Figure 58 – a) Diagram of a fiber bridging a crack and b) the components of the force as the fiber pulls out of the matrix [from 26].**

### *Fiber Embedment Length*

The embedment length  $l$  is the original distance of fiber surrounded by the matrix. In the case where the fiber pulls out of the matrix, usually the shorter embedded fiber is what pulls out of the matrix first, therefore the shorter embedment length is a concern for design. The value of  $l$  can range from 0 to  $L_f/2$  where  $L_f$  is the original length of the fiber. The average or mean pullout length is  $L_f/4$  for a perfectly aligned fiber [16, 17, and 34].

### *Fiber Rupture*

As the fiber is pulled out of the matrix in tension, the fiber either ruptures or the interface between the fiber and matrix fractures (fiber-matrix bond strength reached) and the fiber slides out. Ruptured fibers can occur when fibers are either too long in length or if there is a very high volume fraction. The load carrying capacity analysis can be quite difficult for fibers which rupture, especially if they also exhibit some de-bonding.

### *FRC models*

Over the course of time, researchers have developed mathematical or finite element based models to describe and predict the behavior of FRC structures. Models range from the microscale (attempting to characterize each individual fiber and statistically extrapolate to a global behavior) to the macro scale of a structural response (simplified models which generalize the composite behavior) from the FRC. Only a few of the more commonly used and recognized FRC models are described herein. These models can be used to predict the material behavior for finite element analyses as either bulk material performance of specific cohesive zone elements.

### *Visalvanich and Naaman model*

An empirical based equation relating stress to opening displacement for steel FRC subjected to direct tension was made by Visalvanich and Naaman in 1983 [46]. This model is a polynomial curve that was determined after testing several volume fractions and aspect ratios of a straight steel fiber in mortar. The shear strength and efficiency

factor must be known or estimated to carry out the calculation. The Visalvanich and Naaman stress-displacement relation (equation A2) for FRC is presented below and shown in Figure 59,

$$\sigma_c = (\eta_{VN} \tau V_f L_f / d_f) \left[ 0.1 \left( \frac{2\delta}{L_f} \right) + 1 \right] \left[ \left( \frac{2\delta}{L_f} \right) - 1 \right]^2 \quad (A2)$$

where  $\eta_{VN}$  is an efficiency factor for the fiber orientation and embedment length,  $\tau$  is the shear strength along the fiber surface,  $V_f$  is the volume fraction of the fiber,  $L_f$  is the length of the fiber,  $d_f$  is the fiber diameter, and  $\delta$  is the opening displacement of the crack. This model is an empirically fit curve to the data and only steel fibers were considered.

As seen in Figure 59, the Visalvanich and Naaman model did reasonable well to fit their data presented for a range of volume fractions and aspect ratios. Only a few discrepancies can easily be noticed from the comparison between the data and the model fit. Results show that the combination of a higher aspect ratios ( $L_f/d_f = 83$ ), a 1% volume fraction, and a longer fiber length ( $L_f = 0.5$  inches) produced consistently lower stresses than computed with the model. Also, with a 1% volume fraction of fibers, a short aspect ratio of 42 and a shorter fiber length of 0.25 inches, the model underpredicts the actual measured stresses in the composite material.

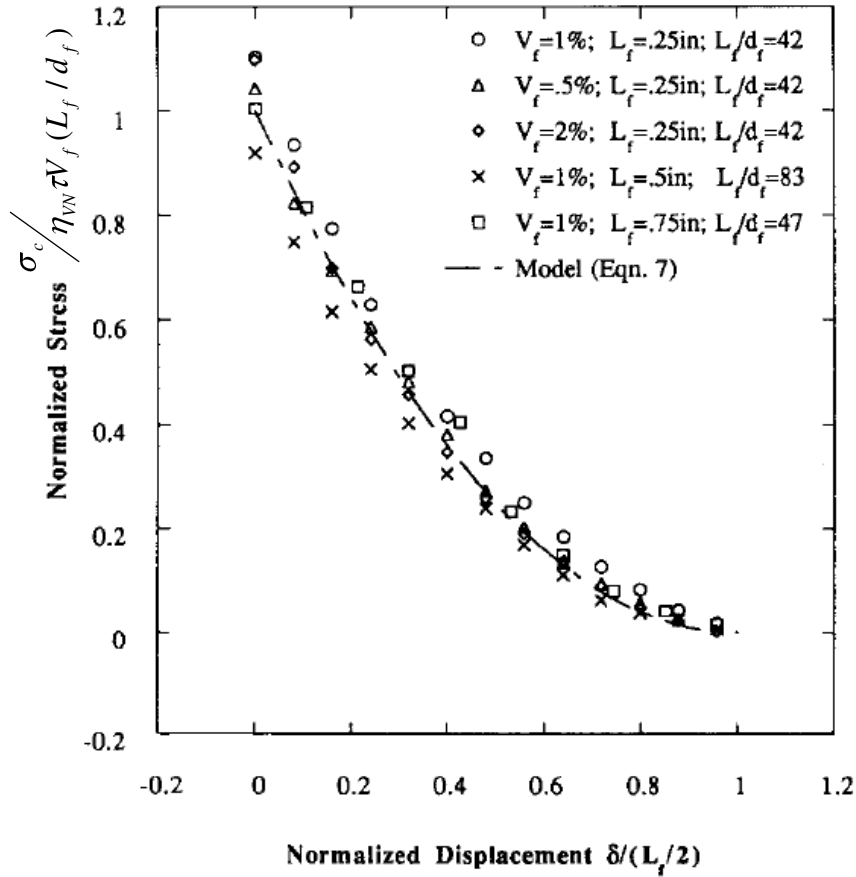


**Figure 59 – Normalized stress versus displacement curve for Viscalvanich & Naaman model and corresponding experimental results [after 29].**

*Li model*

Several studies by Li and others have attempted to capture the micromechanical behavior of single and multiple fibers pulling out of a cement paste matrix [29- 31]. The models incorporate various factors which influence the efficiency of a fiber after cracking. A schematic of stress versus crack opening of a tension specimen is shown in Figure 60.

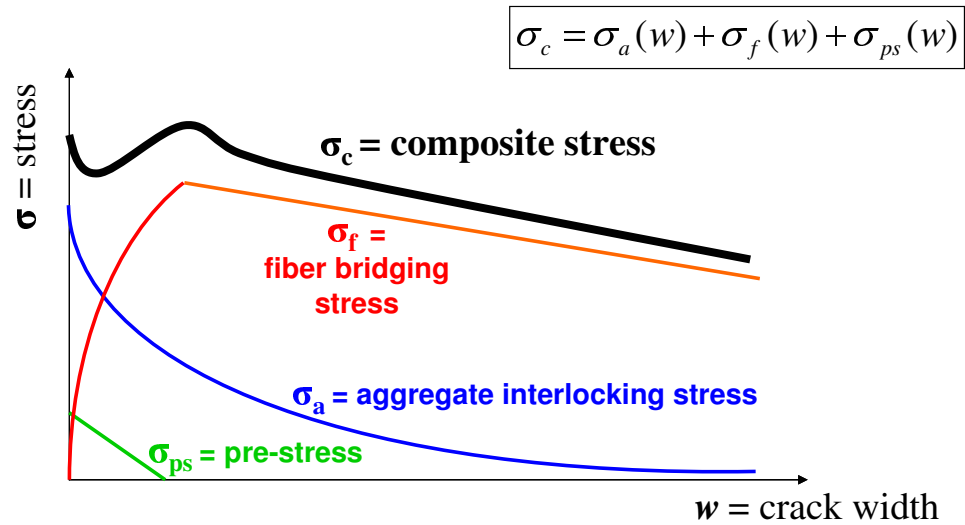


**Figure 60 – Schematic of Li’s micromechanical model for FRC.**

Li’s model [29-31] assumes that before a crack starts the matrix and fiber act elastically together. However due to strain mismatch between the fiber and matrix, a build-up of stress preexists in the fiber at the point when the matrix cracks called the pre-stress  $\sigma_{ps}$ . As the crack widens, this pre-stressing in the fiber is relieved as the fiber de-bonds from the matrix. At the point of complete de-bonding, the fiber is no longer experiencing any stress from the matrix. The initial magnitude for the pre-stressing is the pre-cracked composite strength can be determined using the efficiency factors in Table 19 and equation A1.

If no fiber were to exist, as in the case with plain concrete subjected to direct tension, there is still some stress distributed across a crack. This is due to aggregate interlock because cracks that form early on in concrete often form a tortuous path around the larger aggregates. Protruding aggregates can still interact with other surrounding aggregates until the crack is too wide for these to interact. According to Li’s theory [31], the

equation for aggregate interlocking was chosen to be an experimentally fit power function where cracking initiates at the tensile strength of the concrete matrix. Figure 61 shows the experimental data and power-curve fit to data for both high and normal strength unreinforced concrete.

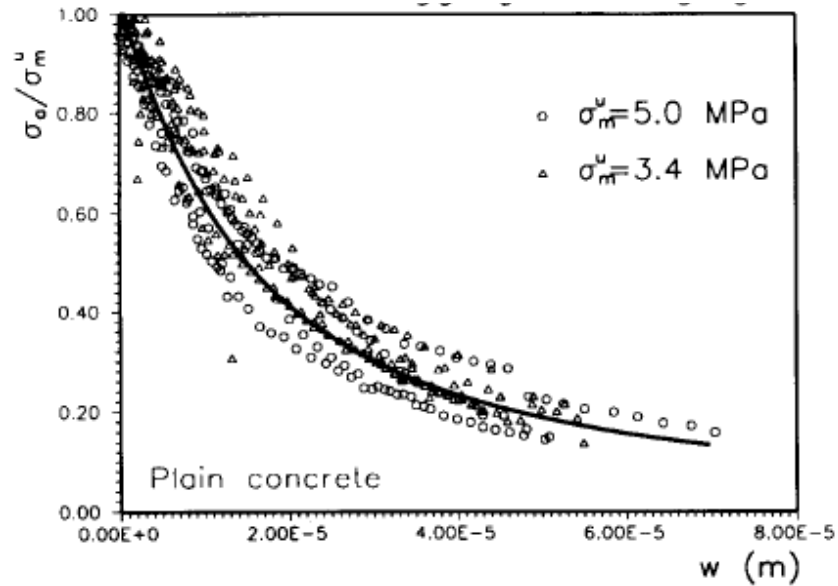


**Figure 61 - Aggregate interlock determination for high and normal strength plain concrete [from 31].**

The calculation of fiber bridging stress can be broken up into two equations: before and after complete de-bonding has occurred. The deflection at complete de-bonding  $\delta^*$  of all fibers in a FRC specimen has been described as the following in equation A3,

$$\delta^* = \frac{\tau L_f^2}{(1 + \mu) E_f d_f} \quad (A3)$$

where  $\tau$  is the shear strength of the bond,  $L_f$  is the fiber length,  $\mu$  is the composite ratio  $\frac{V_f E_f}{(1-V_f)E_m}$ ,  $V_f$  is the fiber volume fraction,  $E_f$  and  $E_m$  are the elastic moduli for the fiber and matrix, respectively, and  $d_f$  is the diameter of the fiber [31]. The equations for single fiber bridging load across a crack are written to account for various fiber properties such as the bond strength, modulus and diameter of the fiber, plus they incorporate the length of the single fiber embedment  $l$  and the orientation angle  $\phi$  of the fiber. The load  $P$  versus crack opening  $\delta$  can be seen in equation A4 for a single fiber,

$$P = \begin{cases} \frac{\pi}{2} \left[ \sqrt{(1+\eta)E_f d_f^3 \tau \delta} \right] e^{f\phi} & \text{where } \delta \leq \delta_0 \\ \pi d_f \left( 1 - \frac{\delta - \delta_0}{l} \right) e^{f\phi} & \delta \geq \delta_0 \end{cases} \quad (\text{A4})$$

where  $\delta_0 = \frac{2\tau l^2}{E_f d_f}$  is the crack opening displacement for a single fiber to have complete

de-bonding (recall for all fibers to de-bond the displacement is  $\delta^*$ ). The snubbing factor  $f$  has been defined by Li [31] to take into account any bending that the fiber undergoes as it pulls out of the cracked face. This snubbing factor can range anywhere from 0 (for complete bending) to 1 (stiff fiber with no bending). From the load equations for a single fiber in equation A4, the fiber bridging stresses for multiple fibers can be computed through integration as follows (equation A5),

$$\sigma_f = \frac{4V_f}{\pi d^2} \int_{\phi=0}^{\pi/2} \int_{z=0}^{(L_f/2)\cos\phi} P(\delta) p(\phi) p(z) dz d\phi \quad (\text{A5})$$

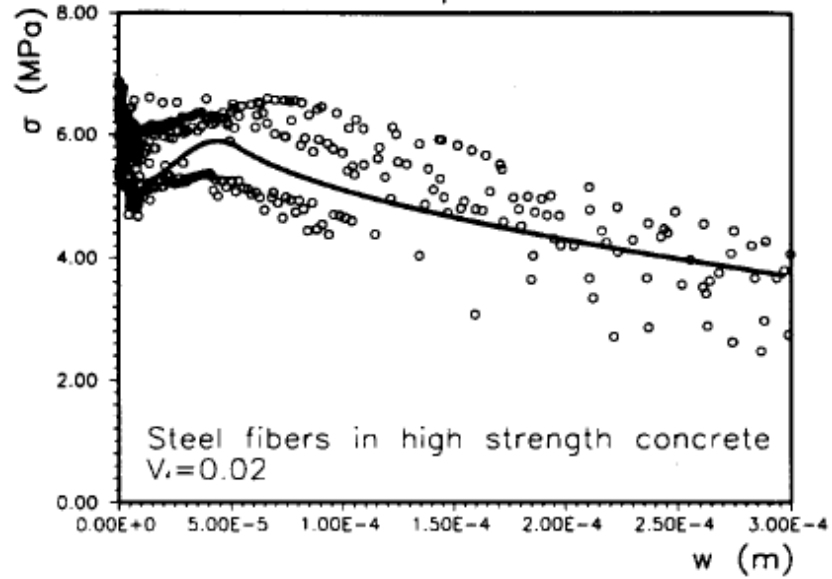
where  $p(\phi)$  and  $p(z)$  represent the probability densities for fiber orientation and fiber length, respectively. The probability density for orientation has been assumed to be for

3D random distribution to be  $\sin \phi$  and for length is assumed to have a uniformly random distribution at  $2/L_f$ . The resulting fiber bridging stress function,  $\sigma_f$ , is shown in equation A6a with the peak bridging stress ( $\sigma_0$ ) occurs when all fibers have completely de-bonded ( $\delta^*$ ) shown in equation A6b.

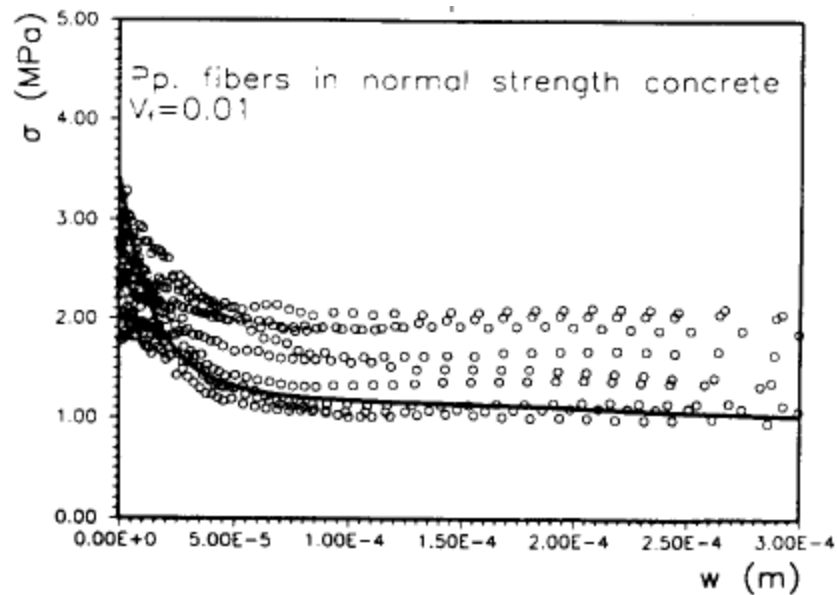
$$\sigma_f = \left\{ \begin{array}{l} \sigma_0 \left[ 2\sqrt{\left(\frac{\delta}{\delta^*}\right)} - \left(\frac{\delta}{\delta^*}\right) \right] \text{ where } \delta \leq \delta^* \\ \sigma_0 \left[ 1 - \frac{2}{L_f}(\delta - \delta^*) \right] \quad \delta \geq \delta^* \end{array} \right\} \quad (\text{A6a})$$

$$\sigma_0 = \frac{2}{4 + f^2} (1 + e^{\pi f/2}) \frac{\tau V_f L_f}{2d} \quad (\text{A6b})$$

Using the three component models for fiber prestressing, aggregate interlock, and fiber bridging stresses, Li summed all these stress components to create a net composite stress curve as seen in Figure 60. These equations have been plotted against test data for straight steel fibers (at 2% volume fraction and an aspect ratio of 100) and for straight polypropylene fibers (at 1% volume fraction and an aspect ratio of 250) as shown in Figure 62a and 62b, respectively.



(a)



(b)

**Figure 62 - Data and Li's model stress versus crack opening curve for (a) steel FRC and (b) synthetic FRC [from 31].**

The model shows potential for matching laboratory data at least up to 0.3 mm crack widths (limit to the tests performed [31]). The data shown for Li's tests seem to be quite scattered and variable for any type of fiber or concrete strength. In particular, the Li model seems to predict the lowest possible data results for the polypropylene FRC as

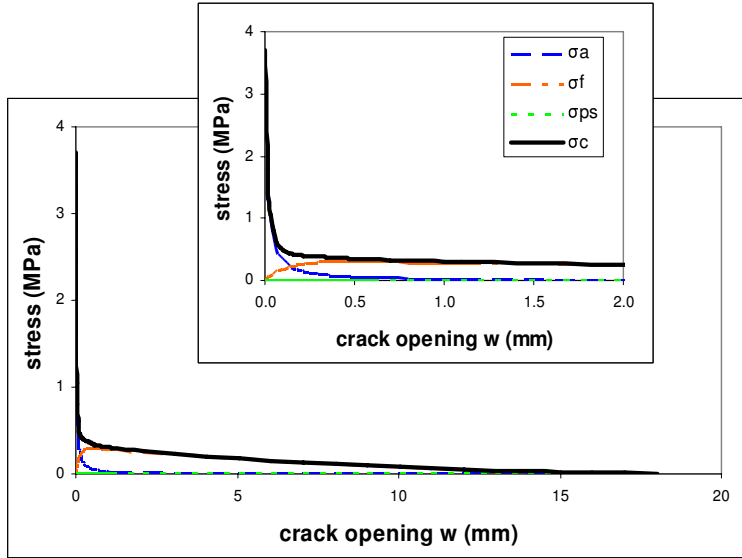
shown in Figure 62b. The Li model may be acceptable for design as a worst-case scenario stress prediction.

The Li model was used in combination with the fiber geometry of the straight synthetic fibers in this report and the results are shown in Figure 63. The diameter of the fiber determined using the aspect ratio ( $L_f/d_f$ ) was found to be 0.444 mm. Li suggested an effective diameter for rectangular cross-sections to be computed using equation A7,

$$d_f = \frac{2wt_f}{(w+t_f)} \quad (A7)$$

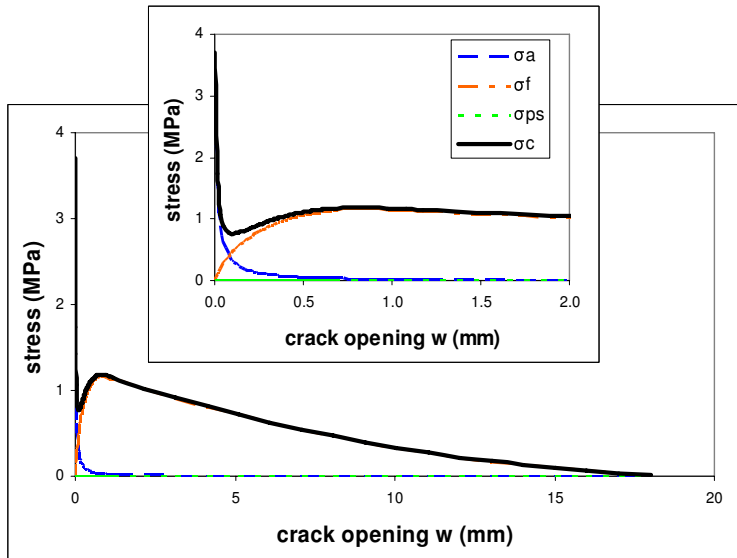
where  $w$  is the fiber width and  $t_f$  is the fiber thickness. For the straight synthetic fibers, the effective diameter is computed to be 0.195 mm. The volume fraction of fibers used was roughly 0.8%, the same as the fiber content for the FGCM study in Chapter 4. The snubbing coefficient  $f$  used by Li was 0.05 in his 1993 study [31], however in a previous study in 1990 [32] Li used 0.702 to describe a polypropylene fiber. All other parameters used as inputs in the Li model were chosen to be the same as the polypropylene inputs used in the study by Li [31]

By changing parameters in the Li model, the total fracture area prediction (calculated as the area under the stress-crack opening curve) ranged from 190 to 720 N/m for the same straight synthetic fiber type. The higher snubbing factor produced a more pronounced secondary peak in the micromechanical model; for smaller fiber diameter size used in the model, the stress magnitude on the secondary peak increased. In order for the Li model to become more accurate, further research and testing for the properties of each fiber type would be needed.



|                   |                            |
|-------------------|----------------------------|
| Fiber type        | polypropylene/polyethylene |
| Ef                | 9.5 GPA                    |
| Lf                | 40 mm                      |
| df                | 0.444 mm                   |
| tau0              | 0.8 MPA                    |
| a1                | 0 MPA mm-1                 |
| a2                | 0 MPA mm-2                 |
| alpha             | 6.67 mm                    |
| shape func p      | 1.2 -                      |
| w0                | 0.015 mm                   |
| sigma_mu (normal) | 3.7 MPA                    |
| Vf                | 0.00794                    |
| Snub coef F       | 0.05                       |
| epsilon_mu        | 0.00013                    |
| Em                | 30 GPA                     |
| GF                | 190 N/m                    |

(a)



|                   |                            |
|-------------------|----------------------------|
| Fiber type        | polypropylene/polyethylene |
| Ef                | 9.5 GPA                    |
| Lf                | 40 mm                      |
| df                | 0.195 mm                   |
| tau0              | 0.8 MPA                    |
| a1                | 0 MPA mm-1                 |
| a2                | 0 MPA mm-2                 |
| alpha             | 2.93 mm                    |
| shape func p      | 1.2 -                      |
| w0                | 0.015 mm                   |
| sigma_mu (normal) | 3.7 MPA                    |
| Vf                | 0.00794                    |
| Snub coef F       | 0.702                      |
| epsilon_mu        | 0.00013                    |
| Em                | 30 GPA                     |
| GF                | 720 N/m                    |

(b)

Figure 63 - Li's model applied to straight synthetic FRC at (a)  $d_f = 0.44\text{mm}$ ,  $f = 0.05$  and (b)  $d_f = 0.195\text{mm}$ ,  $f = 0.702$ .

### Trilinear Softening Model

A finite element cohesive zone model developed and presented in Park et al. [38] was implemented to fit the data of the functionally layered and full-depth TPB specimens. The finite element analysis results are presented in the paper by Roesler et al. [42]. Separate UEL were used to define the local tension softening model of the plain concrete and straight synthetic FRC materials. A bilinear softening model was used for the plain

concrete and a trilinear softening model was used for the FRC material. The parameters to determine the shape of these softening curves were based on the average tensile strength (average of the plain concrete and straight synthetic FRC mixtures combined), the initial fracture energy and total fracture energy of each material respectively according to Park [37 and 38]. An addition parameter, the final crack width  $w_f$  was necessary to define the FRC softening behavior. This value was assumed to be  $L_f/4$  [35 and 42] where  $L_f$  is the length of the fiber.

### *Discussion*

For concrete pavement design such detailed micromechanical models, such as the Li's model may be too complex for practitioners. Several of the micromechanical models such as the aggregate interlock or the pre-stressing of the fibers have negligible effect on the post-peak behavior. Contrary to some of the micromechanical models which attempt to match any volume fraction of fibers in FRC, the model proposed by Park et al. provides a simplified model that accounts for the lower volume fraction straight synthetic FRC mixtures utilized in rigid pavements. Further models using a bilinear or trilinear simplification may be developed to match other fiber types.

## **APPENDIX B: CONCRETE LABORATORY PROCEDURES FOR CASTING FRACTURE SPECIMENS**

### *Mixing Procedure*

The mixing was done with a 2.5 cubic foot pan mixer. The mixing procedure consistently followed this strategy: all aggregates, liquid air entrainment agents (if used), and half of the water was mixed for 1 minute; cementitious materials, remaining water and water reducers were added followed by 3 minutes of mixing; all material was set to rest for 3 minutes; any fibers (if used) were added gradually and 1 more minute of mixing took place. Fresh concrete properties such as slump, unit weight and air content were all recorded.

### *Equipment*

All mixtures of concrete were created using the same mixing and compacting equipment to reduce variability. Steel molds were used to create the TPB, MOR, and shrinkage concrete specimens. A total of 4 TPB size steel molds of inner dimensions described in Chapter 2 were available. The external geometry of the beams was always consistent between each sample. Note the TPB specimens had an 80 mm width and thus exhibit more material and testing variability, especially when utilizing a 25 mm maximum size coarse aggregate or 40 mm long fibers.

Wooden molds were used to cast the concrete for the composite beams onto the asphalt sections. The asphalt sections that were saw-cut to the desired beam dimensions had some variability in size from human error in cutting the asphalt beams.

### *Batching*

The number of replicate specimens was important to consider when reporting the properties of a material. In the majority of the properties reported in this thesis, the number of replicates was anywhere from 2 to 3 specimens. Existing testing standards recommend 4 specimens to be tested to compute fracture properties. The small number of specimens was chosen due to mixing equipment limitations and to limit the between batch variability that would be required for large number of specimen replicates.

In the age effect study in Chapter 3, small volumes (batches) for each mixture were created at a time due to the limited capacity of the equipment in the laboratory. Multiple batches were often made of the same mixture design in order to obtain all the samples needed for the study. One problem seen with this process is that each batch could be slightly different (moisture contents of the aggregates were not measured for each batch prepared; values of moisture levels were assumed to be the same as previous batches measured) and even sample preparation such as compaction effort may have varied with each batch created.

### *Saw-cutting*

Notches (for the TPB and composite beam specimens) were cut using a diamond blade on a mortar saw. A technical limitation with the saw used to cut the specimens was that the blade often bounced in height while samples were pushed past it and notches were noted to vary as  $\pm 5$  mm based on the speed of the cutting. In order to reduce variation, samples were pushed through the machine by the same person and at roughly the same rate. This

variability in notch depth can impact the effective fracture area ahead of the crack and thus impact the calculated fracture properties. To aid in reducing the variability, sample notches were measured after sawing operations to determine the actual notch depth  $a_0$  and this measured value was actually used in the equations for computing the fracture area (see Chapter 2 for TPFM testing calculations).

### *Laboratory Tests*

There are material properties that can be tested for prediction of performance other than strength, slump and air content. Many test methods have been developed – most of these have become standardized – to describe different aspects of the concrete performance in the field. Some of the standardized testing methods [2, 22, and 23] are:

- ASTM C 39 (compressive strength)
- ASTM C 78 (4-point bending flexural strength)
- ASTM C 138 (unit weight)
- ASTM C 143 (slump)
- ASTM C 157 (shrinkage)
- ASTM C 231 (air content by the pressure method)
- ASTM C 496 (split-tensile strength)
- ASTM C 1018, ASTM C 1609 and JCI-SF4 (flexural and residual strengths for FRC)
- TPFM – RILEM method (3-point bending notched concrete fracture) – See Chapter 2

For each concrete mixture created, the compressive strength and split tensile strength were measured of the hardened concrete. The elastic modulus was measured for the age-effect study. All strength and elastic modulus testing was done on 4 inch diameter, 8 inch long cylinders. Flexure and residual strengths were determined using 6 inch x 6 inch x 21 inch beams. ASTM standards were used for all of these properties [2].